Designs of Next Generation c-Si Solar Cells by Numerical Simulation

January 2021

Sugiura Takaya

A Thesis for the Degree of Ph.D. in Engineering

Designs of Next Generation c-Si Solar Cells by Numerical Simulation

January 2021

Graduate School of Science and Technology
Keio University

Sugiura Takaya

A Doctoral Thesis
submitted to Graduate School of Integrated Design Engineering, Keio University
in partial fulfillment of the requirements for the degree of
Doctoral of Integrated Design Engineering

Takaya Sugiura

Thesis Committee:

Associate Professor Nobuhiko Nakano	(Supervisor)
Professor Satoru Matsumoto	(Co-Supervisor)
Professor Hiroki Ishikuro	
Associate Professor Kei Noda	
Professor Kohei Itoh	

Abstract of Doctoral Thesis of Academic Year 2020

Designs of Next Generation c-Si Solar Cells by Numerical Simulation

Category: Science / Engineering

Summary

Crystalline-Si (c-Si) solar cells are the most common solar cells in the photovoltaics (PV) market, which occupy approximately 90% of the total market. Several advanced structures have been proposed to improve c-Si solar cell performances, such as passivated emitter and rear cell (PERC), interdigitated back contact (IBC), tunnel oxide passivated contact (TOPCon), and heterojunction with intrinsic thin-layer (HIT) solar cells.

The c-Si solar cell performance can be evaluated by numerical simulations in semiconductor devices. Numerical simulations help improve cell performance by varying the cell parameters or testing new schemes with reduced durations and costs, which are unavoidable problems in experiments. Furthermore, numerical simulations provide insights into the physical properties of the device, which are difficult to evaluate while performing experiments. These merits render numerical simulations effective for evaluating c-Si solar cell structures.

In this study, the evaluations of advanced c-Si solar cell structures are discussed with new schemes for improving cell performance or for optimization of cell designs. The cell structures of PERC, IBC, and TOPCon are focused upon in this study, which are potential candidates for use in the PV market. These cell structures are evaluated, and the cell designs that improve the cell performances are understood using numerical simulations.

Keywords:

c-Si, IBC, Numerical simulation, PERC, Photovoltaics, TCAD, TOPCon

Graduate School of Integrated Design Engineering, Keio University

Takaya Sugiura

Table of Contents

List of Figures

List of Tables

Chapter 1

Introduction

1.1 Overview of crystalline-Si solar cells

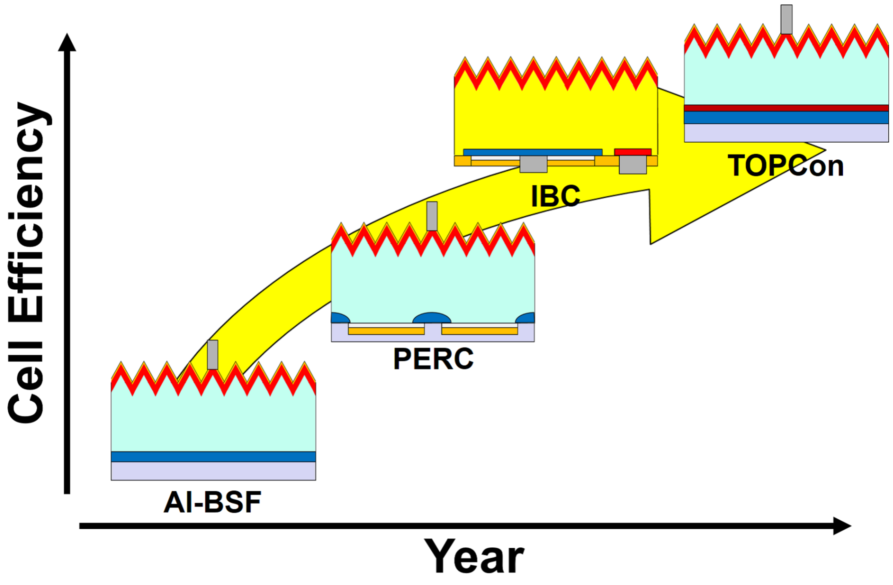

Figure 1.1: Roadmap of c-Si solar cells [1]

Crystalline-Si (c-Si) solar cells are the most common solar cells in the photovoltaic (PV) market, which occupy approximately 90% of the total market share [2]. In the PV field, the most important factor is the improvement of cell efficiency, which is the ratio of output power to the input light energy. In the c-Si PV field, the cell efficiencies are improved mainly by refining the cell structures, as shown in Fig. 1.1.

The most common cell structure is called "Al-BSF" [1]. However, this Al-BSF structure reached its performance limit, and further improvements to increase the output power have been the goal for the PV market.

Table 1.1 summarizes the latest records of the single-junction solar cell efficiencies [3]. From this data, it can be seen that Si (crystalline cell) has the second-highest cell efficiency following GaAs (thin-film cell). Accordingly, Si-based solar cell is considered to be the first candidate of the PV industry.

Table 1.1: Cell efficiencies of single-junction solar cells under the global AM1.5G spectrum at 25 °C [3]

Classification	**Cell efficiency** [%]
Silicon	
Si (crystalline cell)	**26.7±0.5**
III-V cells	
GaAs (thin-film cell)	29.1±0.6
InP (crystalline cell)	24.2±0.5
Thin-film chalcogenide	
CIGS (Cd-free)	23.35±0.5
CdTe	21.0±0.4
Amorphous / microcrystalline	
Si (amorphous)	10.2±0.3
Si (microcrystalline)	11.9±0.3
Perovskite	
Perovskite	20.9±0.7

1.2 c-Si solar cell structures

Currently, there are some new cell structures in the c-Si PV field. The conventional structure is called " Al-BSF " (see Fig. 1.2 for the structure), which has a simple structure that forms the pn junction at the front side and p^+-diffusion at the rear side by Al paste melting during the annealing process. This Al-BSF structure has been widely popular for decades because of its simple process and satisfactory performance [1].

However, the Al-BSF cell reached its limit and cannot yield higher performance. Furthermore, improved cell structures have been researched and developed. The most prevailed one is the passivated emitter and rear cell (PERC) [4], which formed passivation layers at the rear end of the cell. The passivation layer has a suppressed surface recombination velocity and a higher light reflectance, which improves the comprehensive cell performance. Another such structure is the interdigitated back contact (IBC) [5]. In this structure, all the electrodes are concentrated at the rear side to avoid light shading at the front side, which enables absorbing of all the light. There is a c-Si solar cell structure that forms a heterojunction with a-Si (amorphous-Si), which is called heterojunction with intrinsic thin layer (HIT) [6]. In this structure, the heterojunction with the a-Si layer suppresses the recombination loss. The relatively new cell structure is the tunnel oxide passivated contact (TOPCon) [7], which forms a thin tunnel layer to passivate the electrode.

The advantages and disadvantages of these cell structures are summarized

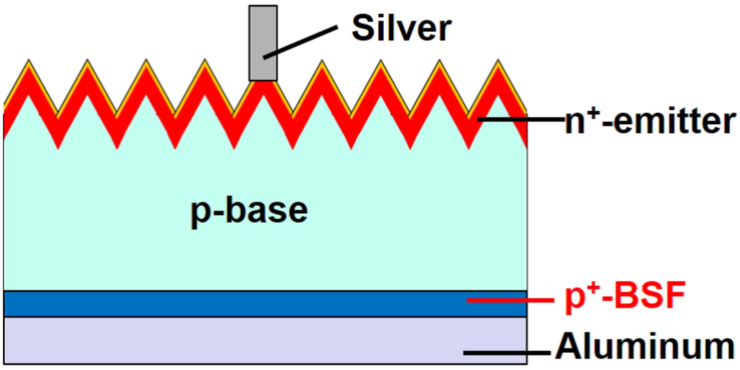

Figure 1.2: Structure of Al-BSF cell

Table 1.2: Features of advanced c-Si solar cells

PERC: Passivated Emitter and Rear Cell [4]	
Advantages	· Improved rear-side internal light reflectance · Suppressed rear-surface recombination · Relatively easier manufacturing process
Disadvantages	· High internal resistance by the restricted contact
IBC: Interdigitated Back Contact [5]	
Advantages	· No front-side shading by electrodes
Disadvantages	· Large recombination loss at the pn-junction interface · Restricted carrier collection · Complex manufacturing process
HIT: Heterojunction with Intrinsic Thin-layer [6]	
Advantages	· Excellent passivation by amorphous-Si · High robustness against the ambient temperature
Disadvantages	· Low carrier mobility of amorphous-Si · Transparent conductive oxide is necessary
TOPCon: Tunnel Oxide Passivated Contact [7]	
Advantages	·Suppressed contact recombination · 1D-carrier transport
Disadvantages	· No additional to light issues

in Table 1.2. Each cell structure has its own features, and characterization can improve the cell performance; however, it can also result in degradation of some parts. The details of each cell are discussed in the following sections.

These structures have their own advantages and disadvantages, and studies on these structures have been conducted for decades. The main focus of these studies has been to improve cell efficiency; however, studies on process developments, installations, and operations have also been conducted. Most types of cells are already in the mass-product phase, and new developments for these cells are expected.

Currently, the highest c-Si solar cell efficiency is over 26%, obtained with the combination of IBC and HIT structures called heterojunction back contact (HBC) [8]. Figure 1.3 shows the HBC structure, wherein the front-side passivation and the rear-side emitter and BSF are designed by amorphous-Si. The full-area light absorption by removing the front-side electrode (feature of IBC) and strong passivation by amorphous-Si (feature of HIT) produced the highest performance in the single-junction c-Si field. Consequently, this HBC structure has led to improvements in c-Si solar cells, which resulted in cell efficiency first exceeding 25% [9, 10], then over 26% [11], and now reaching 26.63% [8].

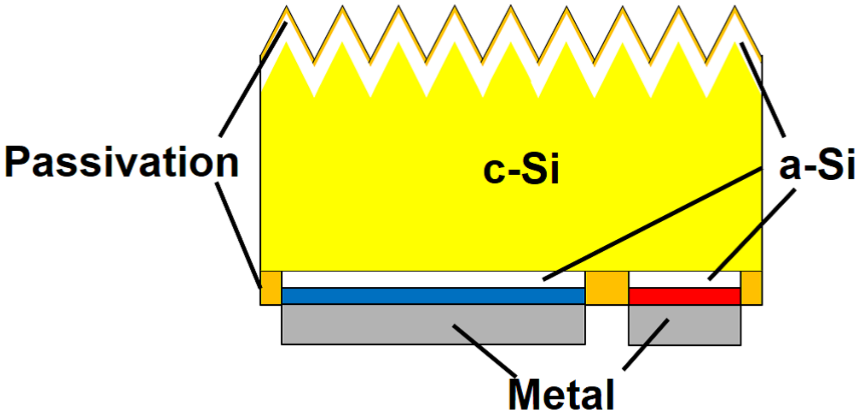

Figure 1.3: Structure of the HBC cell

1.3 Other solar cells

In addition to c-Si solar cells, various other types of solar cells have been widely researched.

Currently, the most focused type of solar cell is “perovskite” solar cell. The first perovskite solar cell was reported in 2009 [12], which had a cell efficiency of 3.81% at that time. However, its cell efficiency has been rapidly increasing in this decade, reaching over 20% in 2019 [3]. The main advantage of perovskite solar cells is the extremely simple manufacturing process that includes spin-coating, dripping, and annealing [13]. The advantage of such a simple process is expected to significantly enhance the application of solar cells.

In the thin film technology, the $Cu(In,Ga)(Se,S)_2$ (CIGS) solar cell has been researched [14] extensively. The main advantage of this technology is the high cell conversion efficiency (current efficiency of 23.35% [15]) that is close to that of the Si-based technology.

There are several combined cell structures, which are called “tandem” solar cells. By stacking multiple different types of solar cells, cell performance can be improved to an extent that cannot be reached with a single solar cell. One of these structures is “smart stack,” which has a cell efficiency of over 30% [16].

1.4 Solar cell simulation

Solar cell simulation is one of the solutions to evaluate, design, or propose cell structures. Simulations have several advantages over experimental methods, such as reducing time and costs incurred to evaluate cell performance, visualization of the internal regions of the device that are difficult to observe in experiments, testing new materials or structures, and precise control of the condition. Table 1.2 summarizes the advantages and disadvantages of performing simulations. A solar cell device usually has a multi-dimensional structure; thus, the simulation that is performed to understand such a structure should also correspond to it.

The free 1D solar cell simulator "PC1D" has been used as the de facto standard to evaluate the fundamental properties of solar cells [17], which is useful for understanding cell physics. However, as advanced solar cell structures have appeared, multi-dimensional solar cell simulation modeling has become important for developing, evaluating, and optimizing solar cells. Several studies have been

Table 1.3: Advantages and disadvantages of semiconductor device simulation

Advantages	· Reducing time and costs · Visualization of device internal physics · Testing new materials or structures · It excludes the uncertain errors of the conditions
Disadvantages	· Precise modeling is necessary · Physics that cannot be modeled cannot be considered

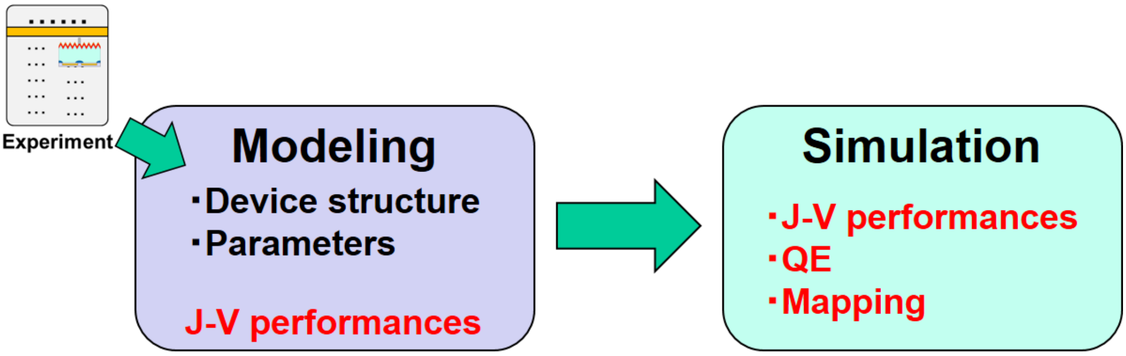

Figure 1.4: Flow of modeling and simulation

conducted to model and evaluate solar cells [18–20], mainly targeting advanced solar cell structures of PERC, IBC, and SOI solar cells. However, there are more prospective solar cells including TOPCon and HBC that are being developed and studied; thus, further development of solar cells by numerical simulation is necessary.

Figure 1.4 illustrates the flow of modeling and simulation. The simulations that are able to closely represent the experiment are necessary to render the results reliable; therefore, the fitting of the J-V performances to the experimental values is performed. The modeling precision will determine the reliabilities of following the simulation results. Further, simulations in which the cell structures or parameters are varied were performed to obtain the J-V performances, QE, mapping, and so on.

Currently, the renewable energy source occupies approximately 20% of the total energy source, and PV is the main source of renewable energy. The demand for renewable energy has been increasing; thus, the development of PV will be very important in the future. From the viewpoint of applications, simulations including modules are also performed [21]. Module-based simulations are desired because solar module is the actual operation form of solar cell, which is composed of numerous solar cells. The solar cell device is the most important part of PV operations; however, simulation of the solar cell device is necessary to improve the total PV performance.

In this study, reports on the development of c-Si solar cells by numerical simulations are reviewed. The contents include PERC designs with bifacial scheme, IBC front designs with bifacial scheme, and TOPCon designs for tunnel dielectric material selection.

1.5 Thesis structure

In this study, the improvements in c-Si solar cell performance with these new structures have been discussed. In Chapter 2, the fundamental physics of c-Si solar cells is introduced. In Chapter 3, the simulation and modeling methods are summarized. The PERC, IBC, and TOPCon cell structures are discussed in Chapters 4, 5, and 6, respectively. In Chapter 7, the conclusion of this thesis is summarized.

Chapter 2

Physics

2.1 Fundamentals of crystalline-Si solar cells

Solar cells are composed of p-n junction diodes. When light is illuminated at diodes, the electron-hole pairs are generated if the illuminated light energy is larger than the band-gap energy of the material (1.1 eV for Si). The generated minority carrier will be separated when the carrier reaches the depletion-region by the electric field and generates the voltage inside the cell. This is called “photovoltaic

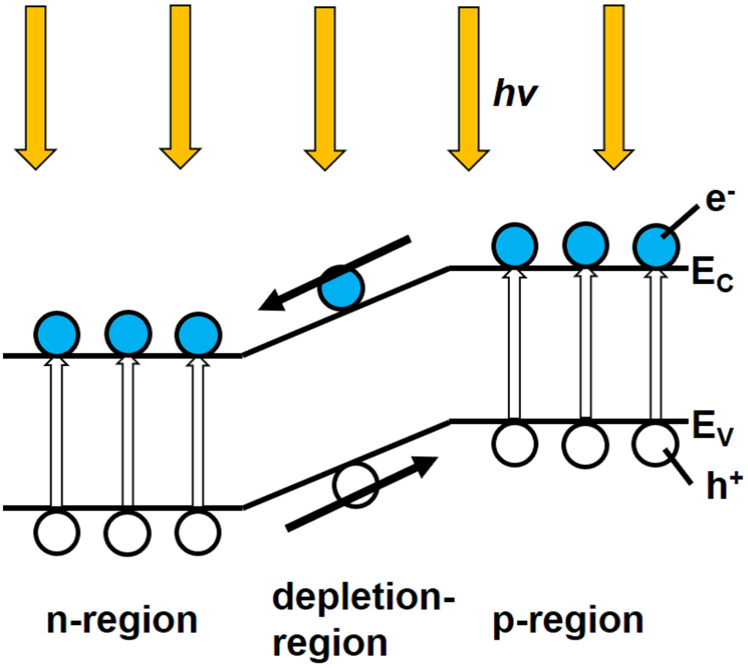

Figure 2.1: Photovoltaic effect diagram

effect," and the mechanism is shown in Fig. 2.1.

To obtain the power as much as possible it is important that incident light is absorbed as much as possible, the optically generated carrier recombination is suppressed as much as possible, and the internal resistance is low. The important cell performances are obtained from the I-V characteristic: short-circuit current, open-circuit, and maximum power. The short-circuit current corresponds to light absorption and carrier generation; absorption of more light improves it. The open-circuit voltage corresponds to the carrier recombination and diode quality; the

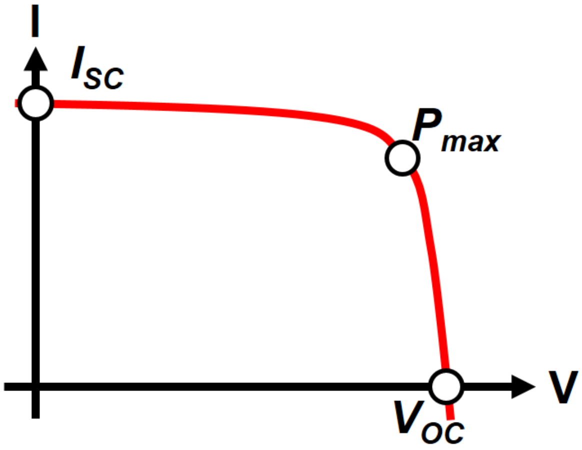

Figure 2.2: I-V characteristic of solar cells

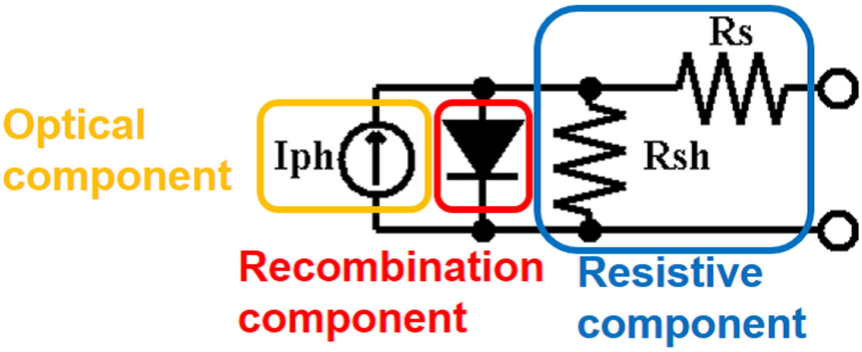

Figure 2.3: Equivalent circuit of solar cells

suppressed recombination and superior diode quality improves it. The maximum power is affected by carrier generation, carrier recombination, and internal resistance. The internal resistance should be suppressed for larger maximum power. Figure 2.3 shows the equivalent circuit of a solar cell. The higher values of short-circuit current, open-circuit voltage, and shunt resistance, the smaller is the value of series resistance.

The main cell performance parameters of a solar cell are J_{SC} (short-circuit current density), V_{OC} (open-circuit voltage), FF (fill factor), and η (cell efficiency). Each parameter corresponds to the optical, recombination, resistive, and total cell performance, respectively. Here, the FF and η are determined by

$$FF = \frac{P_{max}}{I_{SC}V_{OC}}, \tag{2.1}$$

$$\eta = \frac{P_{max}}{P_{in}}. \tag{2.2}$$

where P_{max} is the maximum power obtained from the solar cell and P_{in} is the input light energy of the solar cell.

2.2 Diode equation

The diode equation is expressed as follows:

$$I = I_0 \cdot (e^{\frac{qV}{nkT}} - 1). \tag{2.3}$$

This equation is the sum of the electron current at the depletion-region/neutral p-region and the hole current in the depletion-region/neutral n-region. The equation contains the ideality factor n and saturation current I_0, which determine the diode properties. The ideality factor expresses the extent to which the diode is similar to the ideal diode; $n = 1$ is ideal, and n is between 1 and 2. For silicon, it is known that n is almost 1, which is generally used to derive the saturation current density J_0. The saturation current expresses recombination in diode. A larger I_0 means that the recombination loss is also larger; thus, smaller I_0 is favorable.

When light is illuminated and carriers are generated, the photocurrent appears in this equation.

$$I = I_0 \cdot (e^{\frac{qV}{nkT}} - 1) - I_{ph}. \tag{2.4}$$

The recombination parameter J_0 can be separated in each recombination mechanism [22]. To determine J_0, J_{SC} and V_{OC} are used with some assumptions of $I_{ph} = I_{SC}$ and $n = 1$. At the open-circuit condition, the diode equation is expressed as

$$J_{SC} = J_0 \cdot (e^{\frac{qV_{OC}}{kT}} - 1). \tag{2.5}$$

Here, $e^{\frac{qV_{OC}}{kT}} - 1$ can be approximated as $e^{\frac{qV_{OC}}{kT}}$. Therefore, the J_0 is determined as

$$J_0 = \frac{J_{SC}}{e^{\frac{qV_{OC}}{kT}}}. \tag{2.6}$$

2.3 Light absorption

Light absorption affects how much light current the solar cell receives. To improve this, the surface reflectance should be lower, light shading should be avoided, and internal light reflectance should be higher.

Front-surface light reflectance is the most important problem for light absorption, and anti-reflection coating and texturing are its solutions. The textured surface scatters the incident light at the interface and increases the optical path

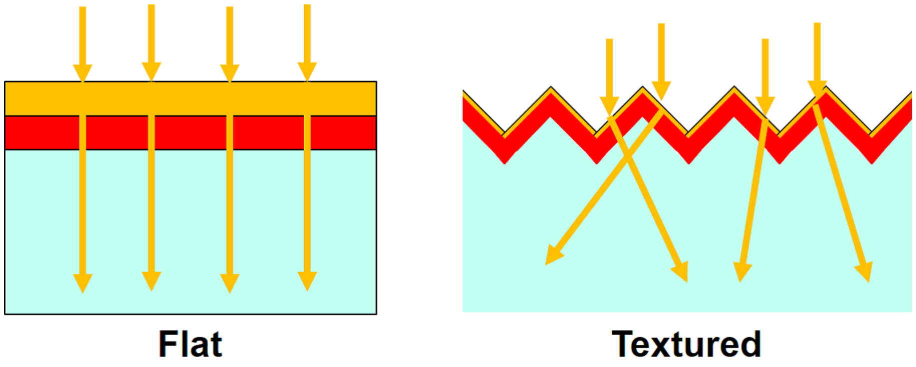

Figure 2.4: Optical path of the textured and flat surface situations

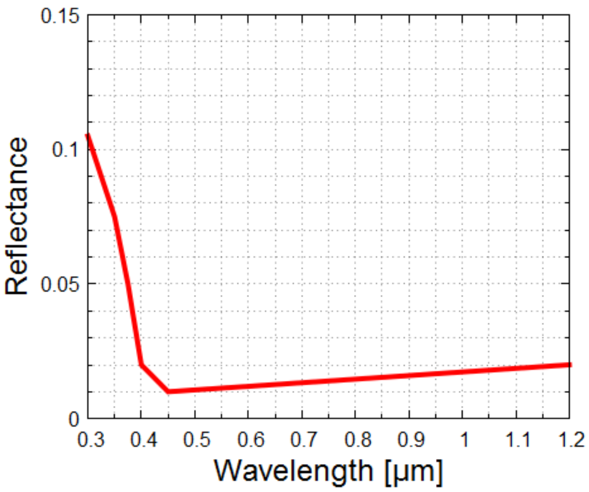

Figure 2.5: Reflectance with anti-reflection coating and texturing [23]

length; thus, more light absorption is expected inside the bulk region (see Fig. 2.4). The anti-reflection coating adopts a Si_3N_4 thin film to suppress light reflectance, and the texturing increases the light path length inside the cell [23].

Another light loss is the shading effect caused by the front contacts (see Fig. 2.6). The front-side contacts shade the regions below; thus, light absorption will be small and proportional to the front-side contact area. Furthermore, shrinking the front-side contact area is effective in increasing light absorption; however, too small contact area will increase internal resistance, which is the trade-off between light absorption and internal resistance, and should be considered. Some advanced solar cell structures consider these problems. The point-contact solar cells of PERC and IBC adopt the rear passivation layer, which has a higher light reflectance, and the IBC removed all front-side contacts to obtain all the illuminated light as its characteristic.

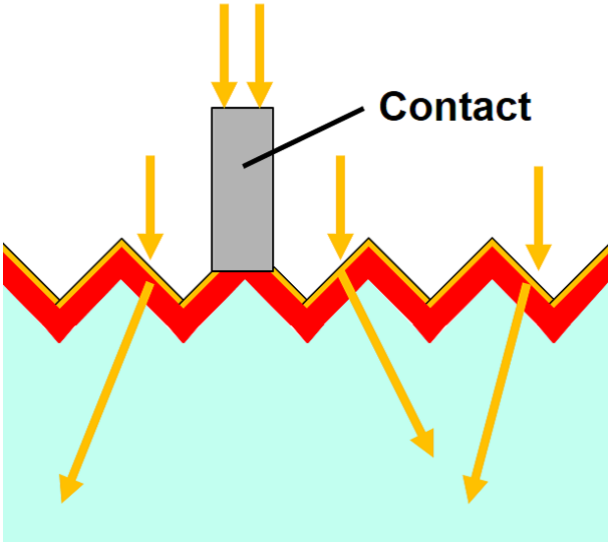

Figure 2.6: Light shading by the front contact

2.4 Carrier recombination

Carrier recombination is the most important problem in solar cells. There are two types of recombination: direct and indirect (see Table 2.1 and Fig. 2.7 for details). Direct recombination occurs when the electron and hole recombine directly, and the auger and radiative recombination are classified. The indirect recombination occurs through the defect level between the conduction and valence band, that is, when both the electron and hole are captured at the defect level they recombine. This indirect recombination is known as Shockley-Read-Hall (SRH) recombination, and it occurs at the bulk region and cell surfaces. The indirect recombination that occurs at cell surfaces is separately classified as “ Surface recombination. ” Most advanced solar cell structures aim at reducing carrier recombination-related losses by passivating the cell surfaces.

Table 2.1: Types of carrier recombination in c-Si solar cell

Name	**Type**	**Location and situation**
Bulk SRH	Indirect recombination	Bulk region
Auger	Direct recombination	Heavily-doped region (emitter)
Radiative	Direct recombination	High-injection situation
Surface SRH	Indirect recombination	Cell surface region

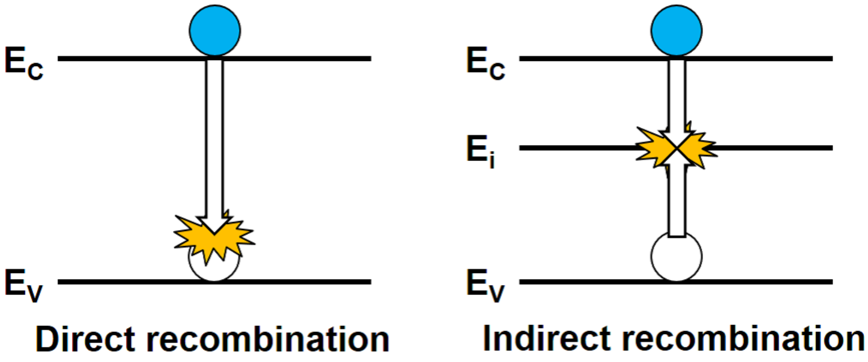

Figure 2.7: Mechanism of direct and indirect recombination

2.4.1 Passivation

Passivation is a major solution to reduce the recombination loss. The surface recombination velocity (SRV) becomes high because the cell surfaces have many unbonded atoms called “ dangling bonds. ” Passivating by dielectric thin films is effective in reducing SRV drastically in the order of tens of centimeter/lower [24]. There are several materials of passivation layers, for example, SiO_2, Si_3N_4, Al_2O_3, and so on; however, the choice of the material should consider the fixed charge in the dielectric films. Figure 2.8 shows the fixed charge effect for the passivation. To suppress the minority-carrier surface recombination, the fixed charge in the passivation layer must have the same charge sign because this fixed charge pushes free carriers back from the surface. Moreover, the opposite charge sign of the fixed

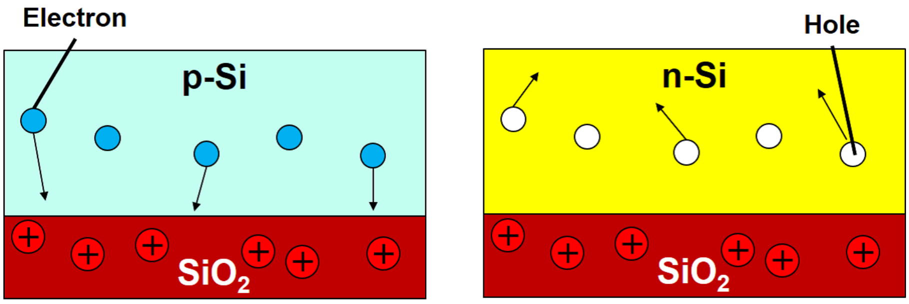

Figure 2.8: Fixed charge effect for the passivation

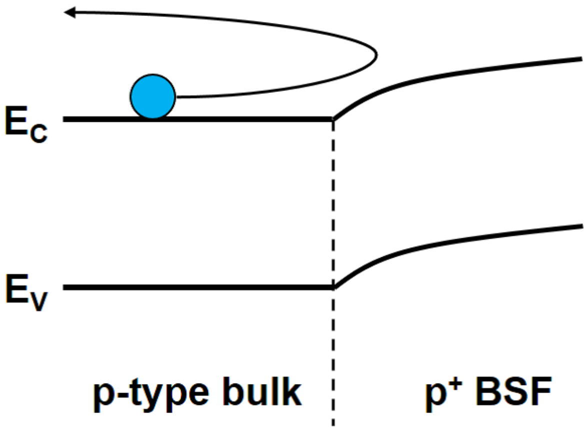

Figure 2.9: Mechanism of BSF by the band diagram

attracts free carriers; thus, the surface recombination increases. It is known that SiO_2 and Si_3N_4 exhibit positive, and Al_2O_3 is the negative charge; thus, they are suitable for n-base and p-base passivation, respectively [25].

The effective SRV strongly depends on the surface doping concentration, and the heavier doping concentration increases the effective SRV for both the p- and n-type bulks [26, 27].

Another passivation method is field-effect passivation, wherein the BSF region is representative [28, 29]. As shown in Fig. 2.9, the BSF forms the slope of the band structure, which pushes the minority-carrier back to the bulk region and suppresses recombination. The Al-BSF solar cell forms the BSF region with rear Al-contact firing processes [30, 31], and high-temperature firing prompts Al-paste to melt to the bulk region as the Al^+ acceptors. The higher temperature makes the Al diffusion deeper and heavier, which leads to stronger field-effect passivation.

2.4.2 Bulk lifetime

The bulk lifetime determines the rough cell performances. Increasing the bulk lifetime as much as possible is important to achieve higher performance, which is strongly dependent on the wafer processes. For the crystalline Si bulks, there are two ways of Czochralski (Cz) and Float Zone (FZ) as the silicon crystal growth for the high-efficiency solar cells [32]. It is known that using FZ-grown Si bulk shows a higher lifetime and better performance than Cz-grown Si bulk; however, the Cz-grown Si bulk is mainly used for high-efficiency silicon solar cells [33].

The choice of the bulk type determines the lifetime, and the n-type bulk is much higher than the p-type bulk, which is a major advantage of this method [34, 35]. For Cz-grown Si bulks, the bulk lifetime of n-type bulk is about 10 times higher than that of the p-type bulk material [36, 37]. The lower lifetime of Cz-grown p-type bulk comes from the formation of boron–oxygen (B–O clusters during the Cz-grown process in which O atoms enter the bulk [34]. Today, the p-type bulk that deactivated B-O clusters are being researched [38], which provides a high bulk lifetime close to the n-type bulk on the p-type bulk [39].

The SRH lifetime in the bulk region has a doping dependency, which is expressed as

$$\tau_{p'}(N) = \frac{\tau_0}{1 + (N/N_0)}, \tag{2.7}$$

where $\tau_{p'}$ is the SRH lifetime, N is the doping level, and τ_0 and N_0 are the parameters [40]. The heavier doping decreases the SRH lifetime as it is well known.

2.4.3 Direct recombination

The auger recombination and the radiative recombination are classified in direct recombination. The mechanism of the direct recombination is shown in Fig. 2.10. The auger recombination is caused by the three carriers: one electron-hole pair and another electron, where the electron-hole recombination gives energy to another electron and excites it. The radiative recombination emits the recombination energy as the light, which is the key mechanism in LED light emitting diodes [41]. The radiative recombination depends on the excess carrier density; therefore, the high injection level increases the radiative recombination rate; however, it is also known that a high injection level can affect it to decrease because of the Coulomb attraction effect between electrons and holes [42]. The radiative recombination rate R_{rad} is expressed as follows:

$$R_{rad} = B(np - n_{i,eff}^2), \tag{2.8}$$

where B is the proportionality factor of the radiative recombination coefficient and $n_{i,eff}$ is the effective intrinsic carrier density.

The possibility of direct recombination depends on whether a semiconductor material is a direct or indirect bandgap material. Si is an indirect bandgap semiconductor [43]; thus, direct recombination, especially radiative recombination, is not likely to occur. The auger recombination can be the recombination loss part

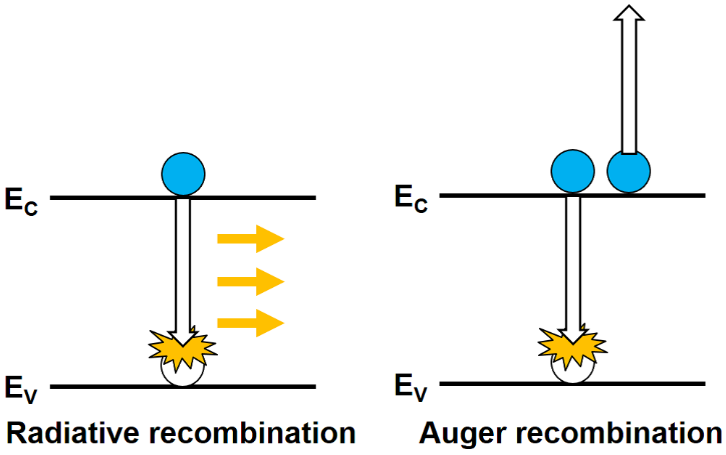

Figure 2.10: Mechanism of the radiative and the auger recombination

for Si solar cells, at the high-injection level or the heavier doped condition [44]. This is because the auger recombination requires one electron–hole pair and another electron to occur, and the high-injection level and the heavier doping provide more carriers. The auger recombination rate R_{auger} is expressed by an equation that includes the rate of electron pair and another electron process (eeh process) R_{eeh}; the rate of electron pair and another hole process (ehh process) R_{ehh}; and auger recombination coefficients of C_n and C_p for both the electron and the hole,

$$R_{auger} = R_{eeh} + R_{ehh} = C_n n^2 p + C_p n p^2. \tag{2.9}$$

The auger lifetime is determined for both the high-injection level and the low-injection level, as

$$\tau_{auger,hi} = \frac{1}{(C_n + C_p)\Delta n^2}(\mathrm{High-injection}), \tag{2.10}$$

$$\tau_{auger,li} = \frac{1}{C_n N_{dop}^2}(\mathrm{Low-injection, n-typesilicon}), \tag{2.11}$$

$$\tau_{auger,li} = \frac{1}{C_p N_{dop}^2}(\mathrm{Low-injection, p-typesilicon}), \tag{2.12}$$

respectively. where $\Delta n = n - n_0 = p - p_0$, and n_0 and p_0 are the thermal equilibrium concentrations of electrons and holes, respectively, [44].

2.5 Solar cell resistance

The resistive component in solar cell affects mainly FF. This resistive component is strongly affected by the cell structures; the point-contact scheme of PERC and IBC shows some degradation. There are some solutions, such as enlarging the point-contact area to avoid resistive components; however, this may weaken the characteristics of the point-contact scheme; therefore, the advantages of it can be smaller. TOPCon; Tunnel oxide passivated contact avoided this problem by adopting the full-rear contact at the rear side with the carrier selective by the tunnel oxide [7].

The resistive component in a solar cell can be derived from the I-V characteristic, the series resistance R_S, and the shunt resistance R_{sh}, as shown in Fig. 2.11. Each R_S and R_{sh} are calculated by the tangent line trend of the I–V curve at the open-circuit or the short-circuit point, respectively.

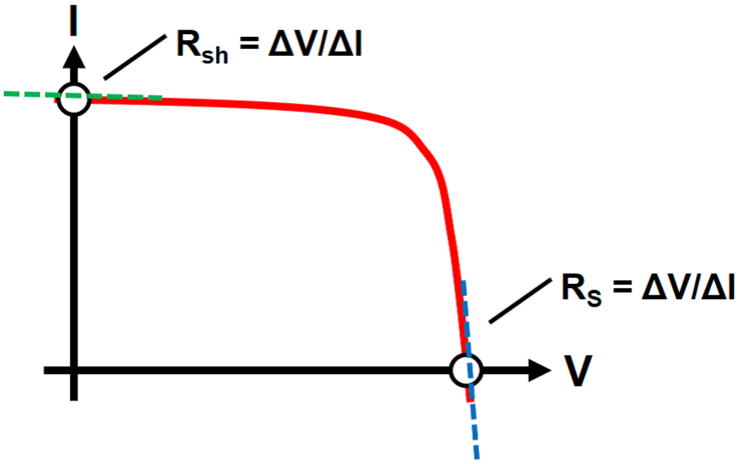

Figure 2.11: Series resistance R_S and shunt resistance R_{sh} in I-V characteristic

2.6 Quantum efficiency

The quantum efficiency is the solar cell device analysis method against the light wavelength. This quantum efficiency aims to reveal the cell response against the wavelength of the contribution of light to the cell performance for each wavelength. There are two quantum efficiencies, EQE and IQE. The EQE includes both the optical and the recombination effects, while the IQE includes only the recombination effect and excludes the optical effect. The EQE and the IQE are expressed as follows:

$$EQE = \frac{Ihc}{q\lambda I_0 S}, \tag{2.13}$$

$$IQE = \frac{EQE}{1 - R_\lambda}. \tag{2.14}$$

where I is the current, q is the elementary charge, h is the Planck's constant, c is the speed of light, λ is the wavelength of the light, I_0 is the intensity of the illuminated light, S is the light illuminated area, and R_λ is the light reflectance at the wavelength. As the definitions express, the IQE always shows a higher value than the EQE because the IQE only expresses the recombination loss. The

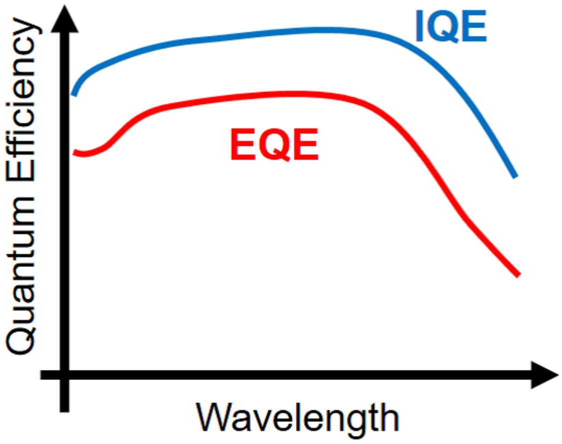

Figure 2.12: External Quantum Efficiency (EQE) and Internal Quantum Efficiency (IQE) graphs

maximum values of both EQE and IQE are less than 1, the minimum values are beyond 0, and the higher values are preferred, which means smaller losses.

The shorter wavelength light is absorbed at the solar cell front-side region, and the longer wavelength light is absorbed at the deeper region of the solar cell; thus, the quantum efficiency at the shorter wavelength expresses the front-side property and the longer wavelength expresses the entire device property. Viewing the quantum efficiency enables us to understand where in the device is the dominant factor in cell losses.

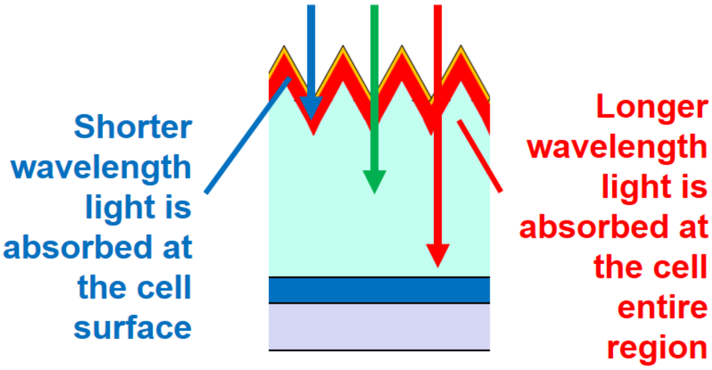

Figure 2.13: Relationship between light absorption and wavelength

2.7 Temperature

Higher temperatures degrade the cell performances. The V_{OC} and FF performances degrade as the temperature rises [45], where the diode saturation current density J_0 and the ideality factor n are the causes.

The adoption of a heterojunction like HIT [6] is one of the solutions against high temperature that suppresses degradations. It has been reported that heterojunction prevents FF degradation at high temperatures [46]. In other words, heterojunction stabilizes the diode ideality factor n, which is related to the resistance performance.

In general, the solar cell performances were evaluated at the room temperature of 25 °C.

Chapter 3

Simulation

3.1 Technology computer-aided design

The technology computer-aided design (TCAD), is a CAD software that aims to evaluate the semiconductor device performance and semiconductor process properties. Utilizing TCAD software for evaluating semiconductor device properties has several advantages: 1). reducing time of avoiding semiconductor processes, which take a long time, 2). reducing the cost of avoiding semiconductor processes, which cost drastically, and 3). visibility of device internal physics that is difficult in the experiment. In this thesis, Sentaurus TCAD software provided by Synopsys, Inc. [47] was used for the solar cell simulations.

For semiconductor device simulation, several equations are solved, including the Poisson's equation, the electron and hole current equations of continuity with the self-consistency. Poisson's equation and the electron and hole current equations of continuity are as follows [50].

$$\varepsilon_S \nabla^2 \phi = q(n - p + N_D^+ - N_A^-), \tag{3.1}$$

$$\mathbf{J_n} = q\mu_n n\mathbf{E} + qD_n \nabla n, \tag{3.2}$$

$$\mathbf{J_p} = q\mu_p p\mathbf{E} - qD_p \nabla p. \tag{3.3}$$

Here, q is the elementary charge, ε_S is the semiconductor permittivity, ϕ is the electrostatic potential, n and p are the electron and hole carrier densities, respectively; N_d^+ and N_A^- are the ionized donor and acceptor densities, respectively; mu_n and mu_p are the electron's and hole's mobilities, and D_n and D_p are the diffusion coefficients. These equations are derived from Maxwell's equations, and are the fundamental equations for the device simulations.

The actual device simulations are modeled by setting each component of the equation, such as the mobility model, carrier generation, and recombination model. For Si solar cell simulations, the carrier generation comes from the light generation of electron-hole pairs, and the recombination model includes the SRH, auger, and radiative recombination.

The solar cell simulation is composed of an optical simulation that calculates the carrier generation by light illumination and an electrical simulation that calculates the carrier transport and carrier recombination, and the outputs are the I-V curve, the quantum efficiency, or the mapping data of the cell physics. The light illumination is solved by the optical solver, and there are several solvers that have their advantages and disadvantages. The general solver is ray tracing [48], which enables solving the multi-dimensional optical problem. Another solver is transfer matrix method (TMM) [49]. It can solve only the 1D-optical problem; however, it enables the consideration of the thin film effect, which is useful for calculating the interface light reflectance that is composed of multiple thin film layers.

Figure 3.1 shows the simple flow of the solar cell simulation.

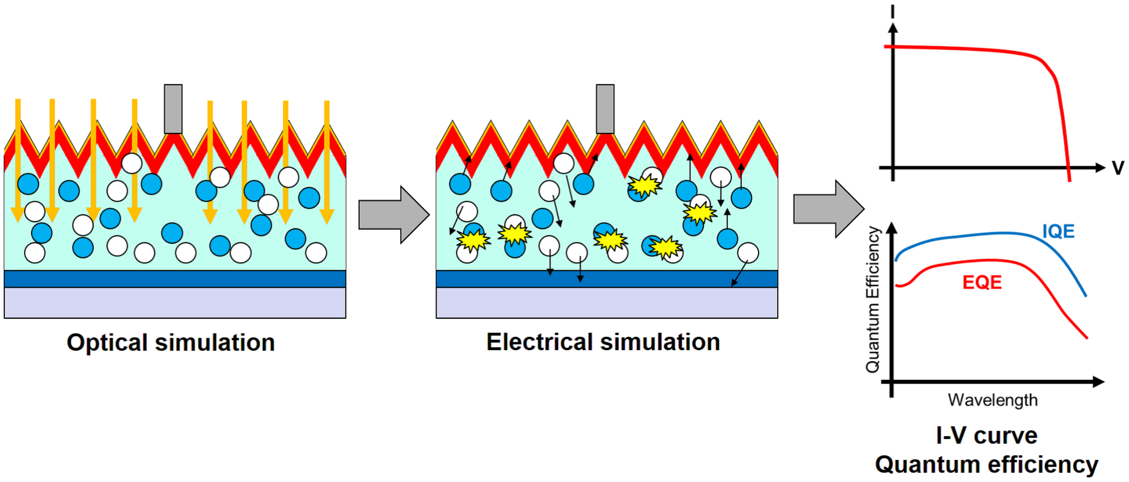

Figure 3.1: Flow example of solar cell simulation

3.2 Solar cell modeling

The solar cell simulations are modeled by activating several physical models, including the carrier mobility model, carrier recombination model, optical model, and contact model. The fundamental modeling of c-Si solar cells is reviewed [51], in which the simulations in this thesis are based on this.

3.2.1 Carrier mobility

The carrier mobility modeling is referred the literature [52]. This mobility model considers the difference of the dopant, and in this thesis, the phosphorus dopant as n-type doping is applied for the modeling. The carrier mobilities of both the electron and the hole against the impurity concentration at room temperature (300 K) is expressed as

$$\mu = \mu_{min} + \frac{\mu_{max} - \mu_{min}}{1 + (N/N_{ref,1})^{\alpha_1}} - \frac{\mu_1}{1 + (N/N_{ref,2})^{\alpha_2}}. \tag{3.4}$$

The parameters of the expression are listed in Table 3.1. The model included four effects: lattice, donor, acceptor, and electron-hole scattering.

Table 3.1: Parameters of the Klaassen's mobility modeling for each dopant of Arsenic, Phosphorus, and Boron [52]

Parameter	**As**	**P**	**B**
μ_{max} [cm^2/Vs]	1417.0	1414.0	470.5
μ_{min} [cm^2/Vs]	52.2	68.5	44.9
μ_1 [cm^2/Vs]	43.4	56.1	29.0
$N_{ref,1}$ [cm^{-3}]	9.68×10^{16}	9.20×10^{16}	2.23×10^{17}
$N_{ref,2}$ [cm^{-3}]	3.43×10^{20}	3.41×10^{20}	6.160×10^{20}
α_1	0.68	0.711	0.719
α_2	2.0	1.98	2.0

3.2.2 Carrier recombination

The carrier recombination modeling is introduced in Chapter 2, in which the SRH, auger, and radiative recombination are included in the simulations.

The auger recombination coefficients, which include the temperature dependence, are modeled as [47]

$$C_n(T) = (A_{A,n} + B_{A,n}(T/300) + C_{A,n}(T/300)^2)[1 + H_n\text{exp}(-n/N_{0,n})], \quad (3.5)$$

$$C_p(T) = (A_{A,p} + B_{A,p}(T/300) + C_{A,p}(T/300)^2)[1 + H_p\text{exp}(-p/N_{0,p})]. \quad (3.6)$$

Where, the coefficients of the equations are listed in Table 3.2.

The radiative recombination coefficient of $B_{rad} = 4.73 \times 10^{-15}$ cm^3/s was used for the simulation [51].

For the SRH recombination, the bulk lifetime or surface recombination velocity is determined for each simulation condition. The information will be listed in each section.

Table 3.2: Coefficients of the auger recombination coefficients both for electron and hole [47]

Carrier	A_A **[cm^6/s]**	B_A **[cm^6/s]**	C_A **[cm^6/s]**	H	N_0 **[cm^{-3}]**
Electrons	6.7×10^{-32}	2.45×10^{-31}	-2.2×10^{-32}	3.46667	1×10^{18}
Holes	7.2×10^{-32}	4.5×10^{-33}	2.63×10^{-32}	8.25688	1×10^{18}

3.2.3 Bandgap narrowing

The bandgap narrowing represents the bandgap deformation by the impurity doping. The bandgap narrowing model of Schenk's proposed model is well used [53], and in this study, the table data of this model from the literature are used for the modeling [19]. Figure 3.2 shows the bandgap deformation as a function of the impurity doping concentration. The donor exhibits a larger bandgap deformation at a higher doping concentration.

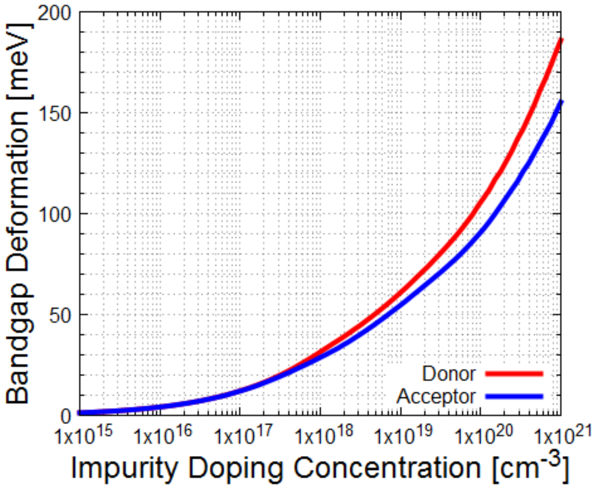

Figure 3.2: Bandgap deformation as a function of the impurity doping concentration [19]

3.2.4 Complex refractive index

The complex refractive index includes the real part of n and the imaginary part of k. This n-k data as a function of wavelength represents the light response of the material. For silicon, the n-k data of Green's report [54] are commonly used. The n-k data of the Green's report is shown in Fig. 3.3. The higher value of k at the shorter wavelength and the small value at the longer wavelength represents the absorption of short wavelength light at the surface region, and longer wavelengths require longer optical path lengths to absorb well. The relationship between the absorption coefficient α and the k value is expressed as [47]

$$\alpha = \frac{4\pi}{\lambda}k. \tag{3.7}$$

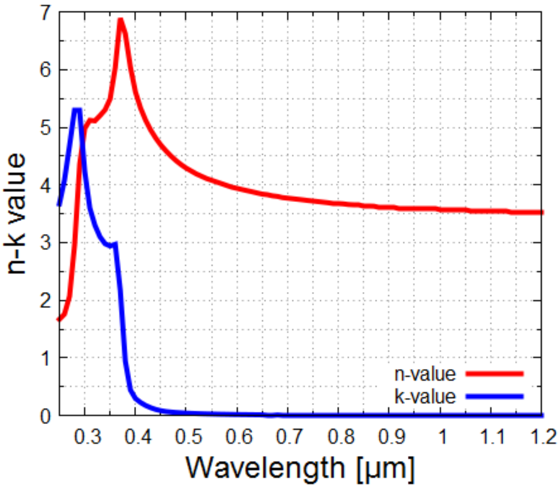

Figure 3.3: N-k data of the Silicon [54]

3.2.5 Free carrier absorption

Free carrier absorption is a phenomenon in which the free carriers in the bulk region absorb light, which inhibits carrier generation [55]. This phenomenon worsens the carrier generation, and the effect increases at the carrier-rich condition, which corresponds to the heavier doping. The free carrier absorption is modeled as the coefficient α_{FCA} which is expressed as

$$\alpha_{FCA} = 2.6 \times 10^{-18} n\lambda^3 + 2.7 \times 10^{-18} p\lambda^2. \tag{3.8}$$

This expression is widely used [56], where α_{FCA} affects the quantum yield and the ratio of the number of absorbed photons to the number of generated carriers. The quantum yield η_G is determined by the total absorption α_{tot}, the original quantum yield value $\eta_{G\Theta}$, and α_{FCA}, as in [47]

$$\eta_G = \eta_{G\Theta}(1 - \frac{\alpha_{FCA}}{\alpha_{tot}}). \tag{3.9}$$

The smaller α_{FCA} improves the quantum yield, and more electron-hole pairs will be generated.

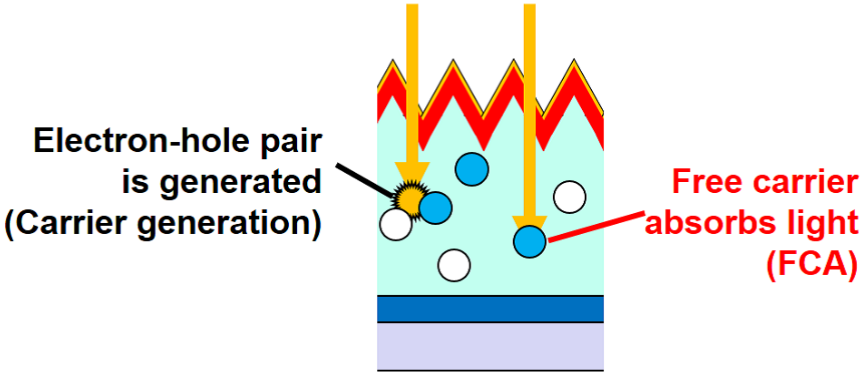

Figure 3.4: Mechanism of the free carrier absorption

3.2.6 Contact modeling

The contact modeling includes the contact type of Ohmic or Schottky, the carrier recombination velocity at the semiconductor/contact interface, and the contact resistivity. Generally, Ohmic contact is necessary for semiconductor device operations, and the charge neutrality and equilibrium are assumed, as follows [47].

$$n_0 - p_0 = N_D - N_A, \tag{3.10}$$

$$n_0 p_0 = n_{i,eff}^2. \tag{3.11}$$

The recombination velocity at the contact interface affects the carrier currents,

$$\tilde{\mathbf{J}_\mathbf{n}} \cdot \hat{n} = q v_n (n - n_0), \tag{3.12}$$

$$\tilde{\mathbf{J}_\mathbf{p}} \cdot \hat{n} = -q v_p (p - p_0). \tag{3.13}$$

where v_n and v_p are the electron's and the hole's recombination velocities. A high recombination velocity of 10^6 - 10^7 cm/s is defined for the contact interface, which is important for the contact functions and increases the carrier recombination at the contact regions.

For the contact resistance modeling, the distributed resistance is often used. The distributed contact resistance value is in the milli-order with the Ωcm^2 unit.

3.2.7 Summary

In summary, the fundamental solar cell modeling is summarized in the Table 3.3.

Table 3.3: Fundamental device simulation modeling for c-Si solar cell

Type	**Physics**
Electrical	Carrier mobility Carrier recombination Bandgap narrowing Ohmic contact
Optical	Carrier generation Complex refractive index Free carrier absorption Quantum yield

3.3 Illumination spectrum

The light spectrum that is generally used for solar cell performance evaluations is “ AM1.5G. ” AM1.5G means “ Air Mass 1.5G, ” the definition is the light illumination by the solar with the 48.2 angle from the vertical direction (defined as AM1.0) [57]. The AM1.5G spectrum (see Fig. 3.6) considers the scattered light, and only the direct light is referred to as AM1.5D.

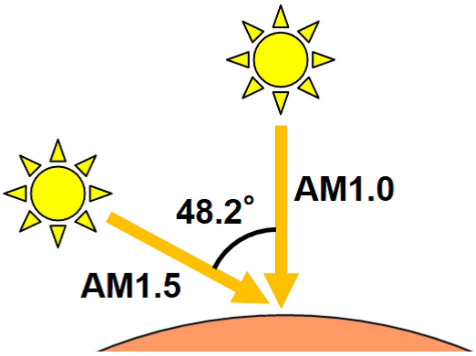

Figure 3.5: Definition of air mass [57]

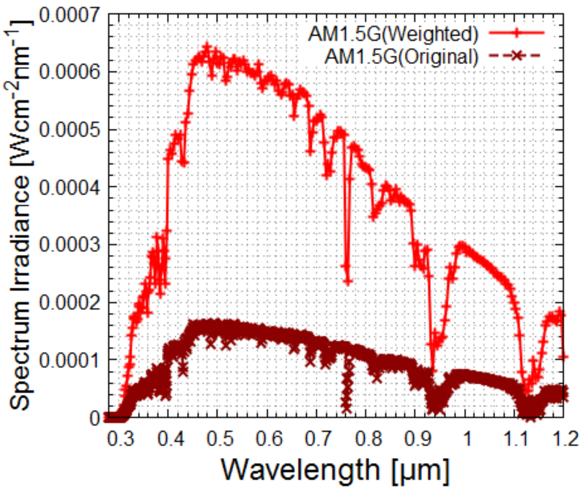

Figure 3.6: AM1.5G spectrum (the weighted spectrum reduces the number of data)

The ground-surface reflected light should be considered for bifacial solar cells [58]. A bifacial solar cell absorbs both illuminated light and ground-surface reflected light. The reflectance of the illuminated light at the ground surface is mentioned as "albedo". The albedo differs by region or season (for example, the snow cover provides a high albedo of near 1), and the albedo of 0.2 is observed for most regions and seasons [59]. The utilization of the ground-surface reflected light will increase the photocurrent of the photovoltaic cells, which is one of the methods to improve cell performance.

Chapter 4

PERC Solar Cells

4.1 Characterization of PERC solar cells

Passivated emitter and rear cell (PERC) is one of the most advanced and common c-Si solar cell structures [1]. PERC is characterized by the formation of a passivation layer on the rear side, as shown in Fig. 4.1. This passivation layer has several effects on the cell performance, which are as follows: 1) The suppression of SRV at the rear contact area will improve the open-circuit voltage. 2) A higher light reflectance will result in a higher short-circuit current. 3) The restricted contact area increases the internal resistance and degrades the fill factor (the details are illustrated in Fig. 4.2) [60–62].

These advantages and disadvantages are in the trade-off relationship, which means that there is an optimized open contact area. There have been some studies on this [63–66]; however, this trade-off is affected by several parameters, such

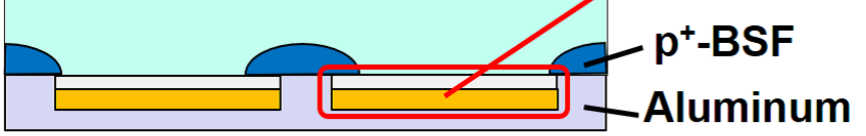

Figure 4.1: p-PERC solar cell structure [4]

as the bulk resistivity, bulk lifetime, contact resistivity, and SRV at passivation layers. The resistive problem of the PERC issue increases at high resistivity bulk, which shows a higher bulk lifetime and is important for increasing the cell output power. Furthermore, the choice of bulk type of p- or n-type determines the minority-carrier at the bulk region, and the mobility of the minority-carrier also affects the resistive components.

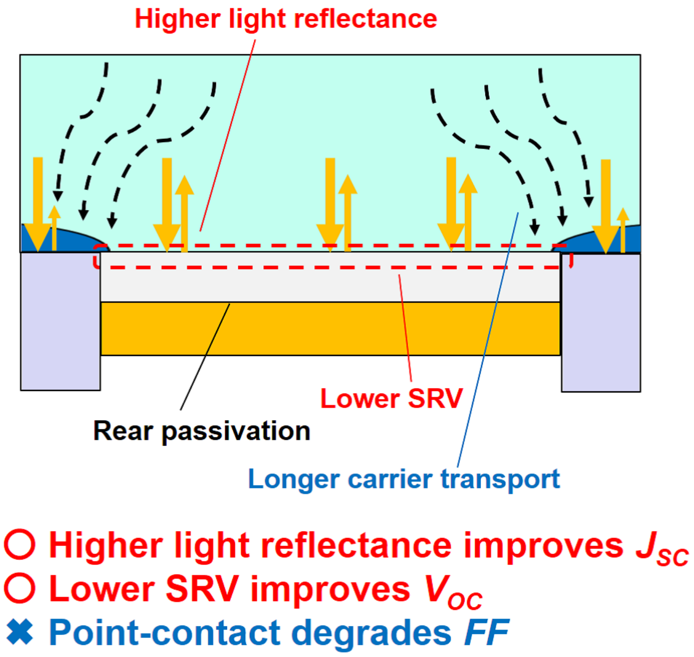

Figure 4.2: Effect of passivation layer in PERC

4.2 Bifacial PERC (PERC+)

Bifacial PERC, also called as 'PERC+' [67], is an advanced PERC structure that absorbs the rear-side illuminated light. The annual output yield is expected to increase by approximately 25% from the conventional PERC by combining the bifacial module [67]. The concept of the bifacial PERC is illustrated in Fig. 4.3.

The advantages of the bifacial PERC are as follows: both-side light absorption increases the photocurrent; lower usage of the rear Al (or Ag) paste, and improved V_{OC} performance for deeper diffusion of Al-BSF (for p-type) [67]. For bifacial PERC designs, rear-side light absorption can affect the optimized design because rear-side light illumination generates carriers mainly at the rear-surface, which is on the opposite side of the emitter, and a longer carrier transport is necessary. Therefore, the effect of the bulk lifetime or bulk resistivity will increase, and the rear surface recombination becomes more dominant in the cell performance.

There is a simulation report for the bifacial PERC solar cell obtained by varying the rear contact area [68]; however, the bulk resistivity or bulk doping type also affects the cell performance significantly. In this study, we report on bifacial PERC solar cell designs [69]. The optimum cell designs are evaluated for different illumination conditions, bulk properties, and rear passivation qualities.

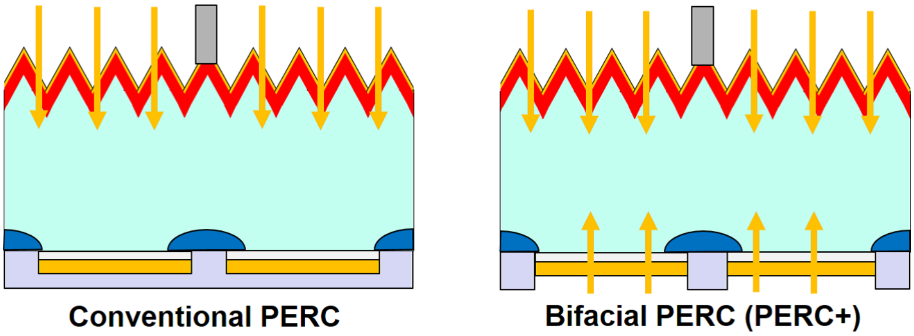

Figure 4.3: Concept of the bifacial PERC solar cell

4.3 Bifacial PERC solar cell designs

In this section, the results from our study on bifacial PERC solar cell designs are presented in [69]. The section is composed of the simulation modeling, its results, and discussion.

4.3.1 Simulation modeling

In this study, bifacial PERC solar cell designs were designed and evaluated under four illumination conditions: the monofacial/front-side, bifacial/front-side, bifacial/rear-side, and bifacial/double-side, as illustrated in Fig. 4.4. The monofacial/front condition corresponds to the usage in the conventional standard module, and the bifacial/double condition corresponds to the bifacial module. To evaluate the front- and rear-side cell properties, the bifacial/front and bifacial/rear conditions were simulated.

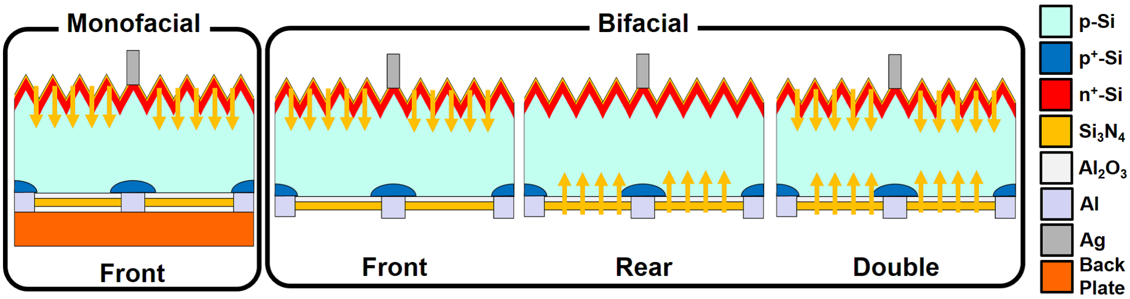

Figure 4.4: Bifacial PERC solar cell simulations for four illumination conditions

The parameters and variables used in the simulations are listed in Table 4.1.

Table 4.1: Parameters and variables of modeling

Parameter	**Value**
Bulk thickness	180 μm
Emitter profile	100 Ω/sq [67]
BSF profile	65 Ω/sq
Rear passivation stack	Al_2O_3 / Si_3N_4 = 10 nm /80 nm (p-type) SiO_2 / Si_3N_4 = 10 nm / 80 nm(n-type)
Front electrode coverage	5%
Internal light reflectance	80% (Front) 65% (Si/Metal) 87.1% (Si/Al_2O_3 (SO_2) (w/o brass)) [67] 92.5% (Si/Al_2O_3 (SO_2) (w/v))
SRV value	1,000 cm/s (Front) 10^6 cm/s (Si/Metal)
Contact finger resistivity	4.5 $\mu\Omega$cm (Front) [51] 20 $\mu\Omega$cm (Rear) [67]
Contact finger distributed resistance	22.5 mΩcm^2
Variable	**Value**
Bulk resistivity ρ_{bulk}	2, 1, 0.5 Ω-cm
Rear pitch distance W_{rear}	100, 200, 350, 700, 1,400, 2,800 μm
Rear passivation SRV S_{rear}	1 - 100 cm/s

The simulation results and the front (or rear-surface) light reflectances are shown in Figs. 4.5 and 4.6, respectively.

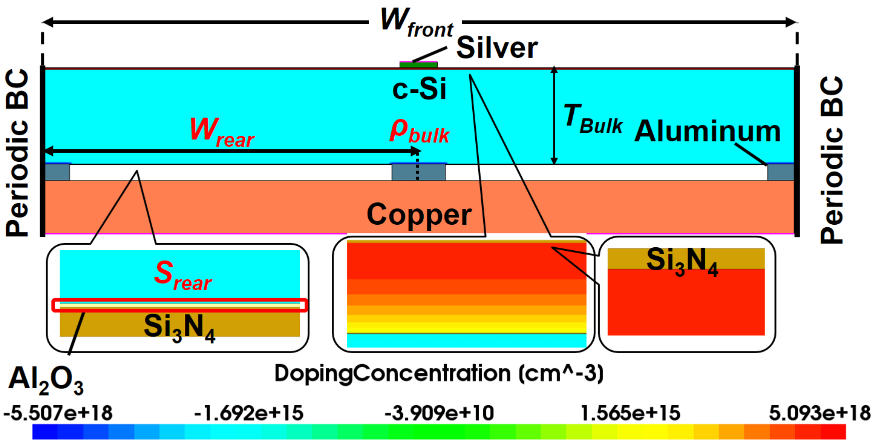

Figure 4.5: Simulation modeling of bifacial PERC with monofacial/front condition

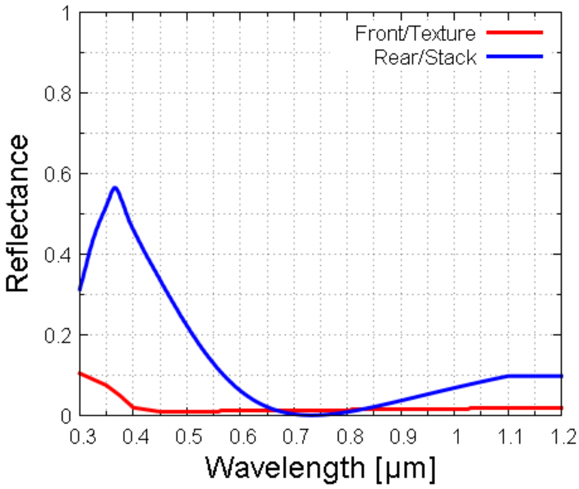

Figure 4.6: Front- and rear-surface light reflectances

A comparison of the experimental results of bifacial PERC [67] are shown in Fig. 4.7 and presented in Table 4.2, The comparison shows that the modeling results agree well with those obtained in the experiments.

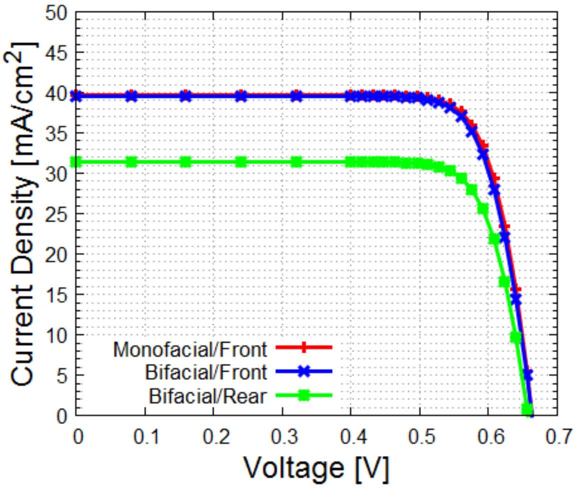

Figure 4.7: J-V curves of modeling for comparison with the experimental result of bifacial PERC

Table 4.2: J-V parameters of modeling for comparison with the experimental result of bifacial PERC

Condition	η [%]	J_{SC} [mA/cm^2]	V_{OC} [mV]	FF [%]	R_S [Ωcm^2]
Monofacial/front (Experiment)	21.0	39.7	664	79.7	0.65
Monofacial/front (Simulation)	21.0 (±0.0)	39.7 (±0.0)	663 (-1)	80.0 (+0.3)	0.66 (+0.01)
Bifacial/front (Experiment)	20.8	39.5	664	79.1	0.82
Bifacial/front (Simulation)	20.7 (-0.1)	39.5 (±0.0)	663 (-1)	79.1 (±0.0)	0.83 (+0.01)
Bifacial/rear (Experiment)	16.5	31.4	658	79.6	0.82
Bifacial/rear (Simulation)	16.5 (±0.0)	31.4 (±0.0)	657 (-1)	80.0 (+0.4)	0.84 (+0.02)

4.3.2 Bifacial PERC: Monofacial/front

The cell efficiencies of the p- and n-type bifacial PERC under the monofacial/front condition are shown in Fig. 4.8. The effect of rear passivation SRV for each bulk of p-type, p-type (w/o BO), and n-type is studied, and a suitable bulk condition for any passivation conditions is provided. For p-type bulk, the bulk resistivity that corresponds to the higher bulk lifetime is the most appropriate, that is, a ρ_S of 2 Ω-cm. The p-type bulk provides a lower lifetime; thus, the lifetime of this bulk type is much more important than the internal resistance. However, in the p-type bulk without BO, suitable bulk resistivity changes at the rear passivation SRV of 10 cm/s, and a higher bulk lifetime of 2 Ω-cm should be selected for smaller SRV conditions, and a lower bulk resistivity of 0.5 Ω-cm should be selected for greater SRV conditions. This different trend from the p-type bulk is due to the overall higher bulk lifetime, which makes the rear passivation SRV dominant to the cell performance. Therefore, a smaller SRV, wherein there is almost no recombination loss suppressing bulk recombination is effective; however, at a greater SRV of the rear passivation that is dominant to the cell loss, improving the internal resistance

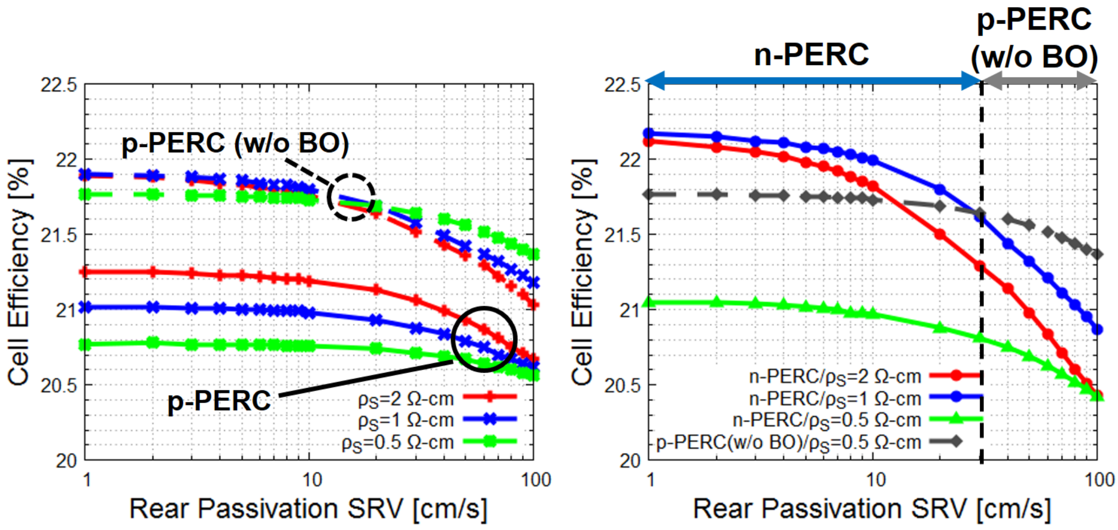

(a) p-PERC **(b) n-PERC**

Figure 4.8: Cell efficiencies of p- and n-type bifacial PERC under the monofacial/front condition

component should be selected.

In contrast, for n-type bulk, a bulk resistivity of 1 Ω-cm is suitable for any SRV, even the overall highest bulk lifetime situation. Here, the minority carrier of n-type bulk is the hole, which provides approximately 1/3 carrier mobility compared to the p-type bulk of the electron, and the lower bulk resistivity that corresponds to the heavier doping decreases the carrier mobility. PERC is the point-contact scheme, and the longer carrier transport is the bottleneck of the performance, especially for higher resistivity and smaller carrier mobility. The adoption of the heavier n-type doping is not effective for the point-contact scheme because of these phenomena, and the higher bulk resistivity will increase the internal resistance; therefore, a medium bulk resistivity value of 1 Ω-cm is suitable.

The comparison of the p-type (w/o BO) and n-type shows that the rear passivation SRV of 30 cm/s is the branch point of the bulk selection. An SRV smaller than 30 cm/s renders the n-type the most appropriate and a value greater than 30 cm/s makes p-type (w/o BO) bulk the optimum one. This bulk switching is due to the carrier mobility effect, as both the bulk types provide sufficient lifetimes. For the lower SRV condition, suppressing the bulk recombination loss is important, and for the higher SRV condition, improving the carrier transport by the lower bulk doping is better.

In summary, the above discussion optimizes the bifacial PERC performances at monofacial condition usage. At the lower bulk lifetime condition that corresponds to the p-type bulk, increasing the bulk lifetime is the best solution. However, at the higher bulk lifetime condition that corresponds to the p-type (w/o BO) and n-type bulks, the rear passivation SRV determines the cell designs; the smaller SRV condition that increases the bulk lifetime to suppress the recombination loss is the most appropriate; however, at the greater SRV condition, the recombination loss is not avoidable and improving the carrier transport should be considered.

The cell designs considering the rear pitch distance are shown in Figs. 4.9 and 4.10. The rear contact pitch distance is the most important design for PERC, and the suitable pitch distance is affected by the bulk resistivity and the rear passivation SRV. At a greater SRV, a longer pitch distance increases the effect of rear SRV; thus, the shorter pitch distance is favorable. Furthermore, regardless of the rear SRV, the carrier transport problem becomes larger when the pitch

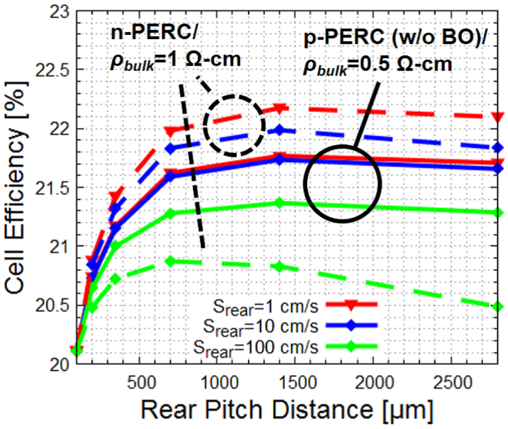

Figure 4.9: Effect of the rear pitch distance for p- and n-type bifacial PERC under the monofacial/front condition

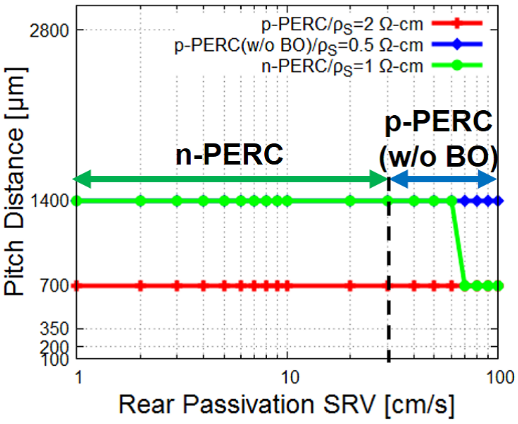

Figure 4.10: Suitable pitch distance of p- and n-type bifacial PERC under the monofacial/front condition

distance is longer; therefore, the adoption of the n-type bulk will make it sensitive to the pitch distance.

Figure 4.9 provides the trend against the rear pitch distance for three different SRV conditions. The important factor is that the n-type bulk is sensitive to the rear pitch distance, especially at the greater SRV condition. The n-type bulk provides poor carrier transport because of the smaller carrier mobility; thus, the effective SRV will increase compared to the p-type bulk. The suitable rear pitch distance is shown in Fig. 4.10. The p-type PERC of 700 μm pitch distance is the best for any rear passivation SRV, and the pitch distance of 1,400 μm is the best for the higher bulk lifetime condition.

4.3.3 Bifacial PERC: Bifacial/front and bifacial/rear

The adoption of the bifacial module removes the rear brass to allow the rear-side illuminated light to enter the cell; however, the contact resistance increases. Figure 4.11 shows the series resistance comparison between the bifacial/front and the monofacial/front. As seen from the graph, the internal resistance of the bifacial/front condition is significantly larger than that of the monofacial/front, especially at a larger rear pitch distance. This means the larger rear pitch dis-

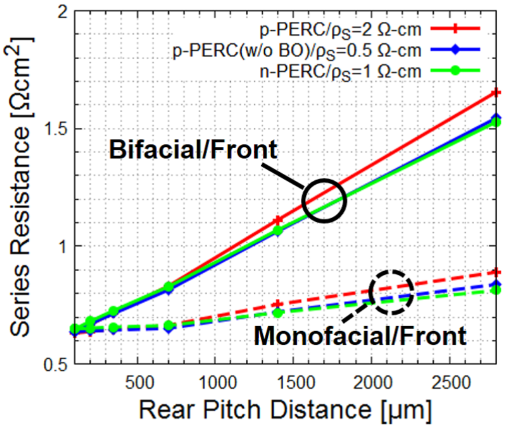

Figure 4.11: Series resistance of bifacial PERC under the bifacial/front condition

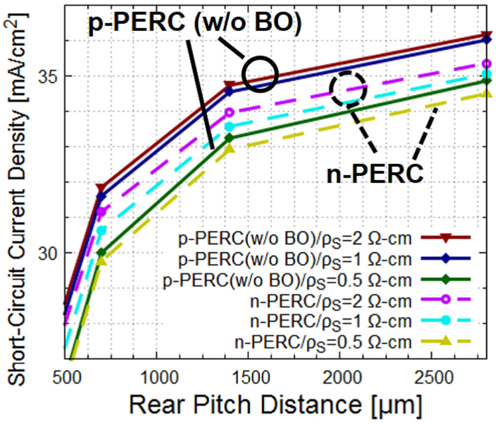

Figure 4.12: Short-circuit current density of bifacial PERC under the bifacial/rear condition

tance will degrade cell performance at the bifacial usage, which the larger pitch distance is important to increase the rear-side light absorption. Figure 4.12 shows the short-circuit current density of the bifacial PERC under the bifacial/rear condition. Contrary to the internal resistance, as it is obvious the larger rear pitch distance of the smaller rear contact area increases the short-circuit current density. In summary, a larger pitch distance is advantageous for the rear properties and is disadvantageous for the front properties.

The bifaciality factor, which is expressed by η_{rear}/η_{front}, is useful for understanding the cell performances at the bifacial usage. Figure 4.13 shows the bifaciality factor of the bifacial PERC. At the smaller SRV condition, a bifaciality factor higher than 0.8 is expected, and the p-PERC (w/o BO) provides a higher bifaciality factor. For both p-PERC and n-PERC, a lower bulk resistivity is better for the bifaciality factor. This indicates that a higher bulk lifetime improves the bifaciality factor because the rear-side illumination generates carriers mainly at the rear surface, which is the opposite side from the emitter region. Therefore, the carriers must move over longer distances compared to the front-side illumination, and the bulk lifetime is important for collecting carriers as much as possible.

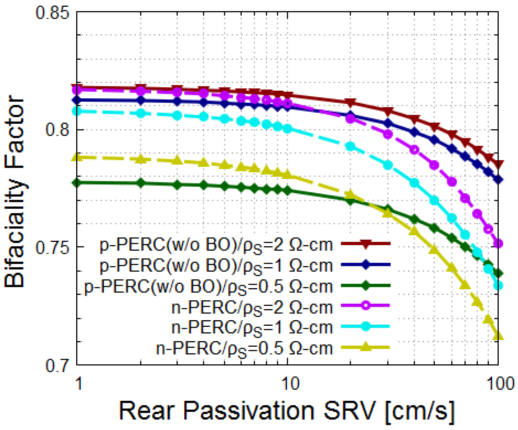

Figure 4.13: Bifaciality factor of the bifacial PERC

4.3.4 Bifacial PERC: Bifacial/double

The bifacial/double condition is the situation of the bifacial usage. The albedo of 20% is expected for the situation to evaluate performances.

Figure 4.14 shows the bifacial/double performances of the p-PERC and n-PERC. A power density higher than 25 mW/cm^2 is expected by adopting the bifacial scheme, which corresponds to a cell efficiency of approximately 25% under monofacial conditions. Regardless of the advantages and disadvantages of adopting the bifacial scheme discussed above, which provides a trade-off regarding the rear contact pitch distance, a similar discussion of the monofacial/front can be applicable. The rear passivation SRV of 30 cm/s is the key value also in the bifacial/double condition, where the smaller SRV makes the n-PERC and the greater SRV makes the p-PERC (w/o BO) suitable.

The cell designs of the bifacial PERC at bifacial/double are shown in Figs. 4.15 and 4.16, respectively. Compared to the cell designs of the monofacial/front (Fig. 4.9), the dependence against the rear pitch distance is larger and the performance at a larger rear pitch distance degrades more than the monofacial/front condition. This indicates that the internal resistance increase causes a disadvantage over the advantage of the improved short-circuit current density; this is because at a larger

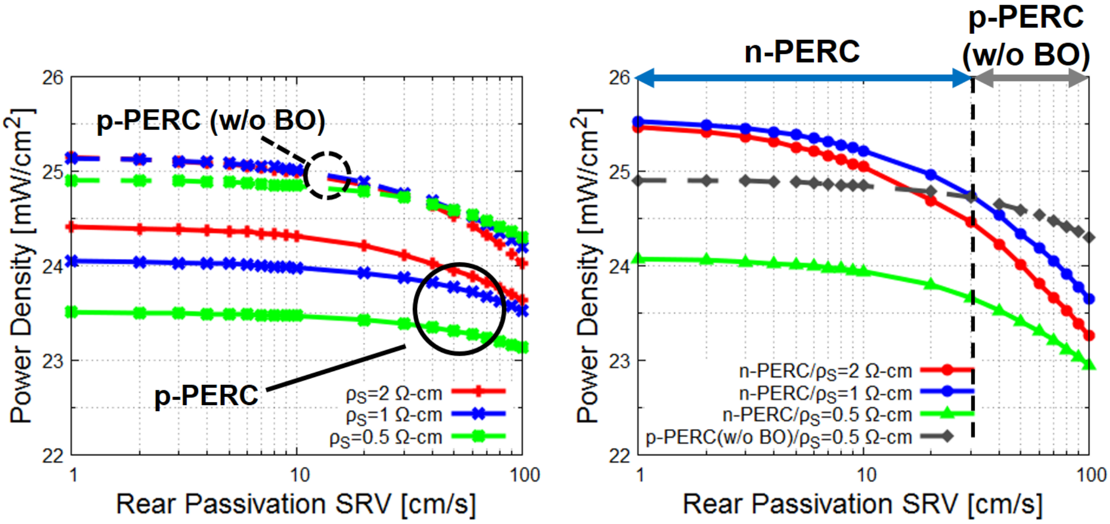

Figure 4.14: Cell efficiencies of p- and n-type bifacial PERC under the bifacial/double condition

pitch distance, the increase in short-circuit current density does not decrease the rear contact area much even if it increases the internal resistance significantly. The suitable pitch distance is almost the same as the monofacial/front condition, that is, a pitch distance of 700 μm for p-PERC and 1,400 μm for the higher bulk lifetime condition.

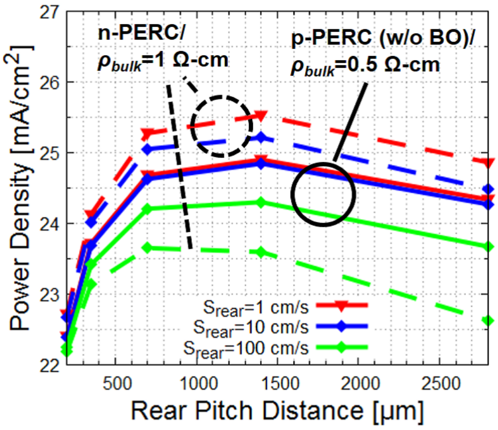

Figure 4.15: Effect of the rear pitch distance for p- and n-type bifacial PERC under the bifacial/double condition

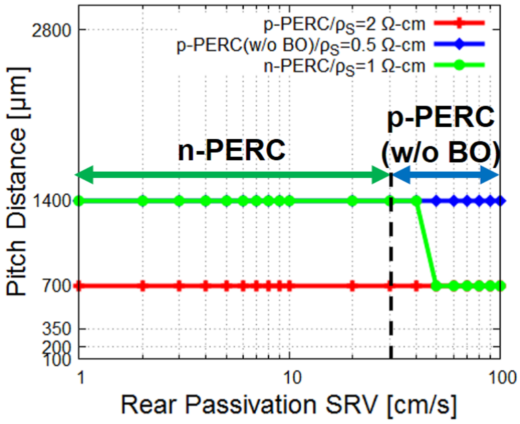

Figure 4.16: Suitable pitch distance of p- and n-type bifacial PERC under the bifacial/double condition

4.3.5 Conclusion

The bifacial PERC solar cell designs for four illumination conditions are discussed by considering the bulk effects of resistivity, lifetime, and rear passivation SRV. The suitable cell designs are almost the same between the monofacial/front and bifacial/double conditions. The rear passivation SRV value of 30 cm/s is the key value that determines the suitable bulk type, the smaller SRV makes the n-type, and the greater the SRV, improves the p-type (w/o BO). By adopting the bifacial scheme, a power density larger than 25 mW/cm^2 is expected, and the rear contact pitch distance of 700 μm for p-PERC and 1400 μm for the higher bulk lifetime condition are favorable.

Chapter 5

IBC Solar Cell

5.1 Characterization of IBC solar cells

Interdigitated back contact (IBC) solar cells concentrate both the emitter and BSF regions at the rear side. Furthermore, IBC facilitates non-contact shading at the front surface, thereby enabling absorption of all light and increasing the photocurrent.

The concentration of both p^+- and n^+-regions at the rear side causes unique IBC problems: increased carrier recombination at the p^+- / n^+-interface regions [70] and electrical shading [71, 72]. These problems must be considered while designing IBC solar cells.

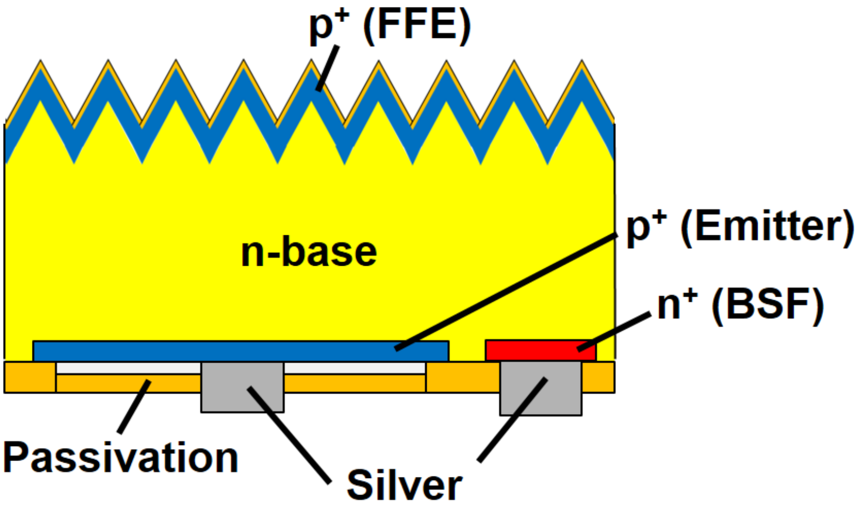

Figure 5.1: n-IBC solar cell structure [5]

5.2 Front diffusion in IBC solar cells

IBC solar cells concentrate both the emitter and BSF regions on the rear side. However, the front side contributes to the cell performance in terms of front-side doping, wherein FFE and FSF are known [73]. These have different effects on solar cells for the carrier transport view, as shown in Fig. 5.2.

The problem of electrical shading arises from the shrunk emitter area and the worse emitter carrier collection. There are a few ways of solving this problem; for example, using the rear emitter overlap scheme [74–76]; however, this emitter overlapping scheme has the potential to increase the leakage current [70] in some situations [76]. One method of solving the electrical shading is the formation of FFE. The FFE eases the electrical shading problem caused by the shrunk emitter area, which has poor carrier collection, by enhancing the lateral-direction carrier transport of the minority-carrier at the floated emitter region. The FFE has a bipolar structure [77] that collects holes above the BSF region, and the collected holes are pumped as the majority-carrier to the region above the FFE, where the carriers are re-injected and then collected to the emitter at the rear side [78]. This FFE will work effectively as the emitter area at the rear side is small, and it is reported that the FFE can be preferred over the FSF [73].

Another FSF scheme simply pushes the minority-carrier back to the rear side, which enhances the vertical-direction carrier transport. The FSF scheme is a common method used for designing IBC solar cells [78]. Furthermore, the entire

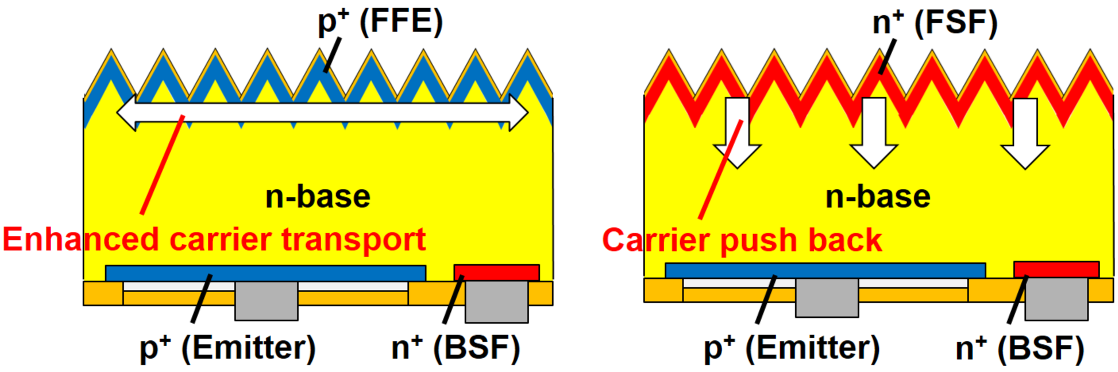

Figure 5.2: Front floating emitter (FFE) and front surface field (FSF) in n-type IBC solar cell

cell performance is significantly affected by the design of the rear side [79]; the large emitter area is preferred, and the IQE drops in the BSF region.

To achieve better performance, optimization of the front diffusion profile is important for both FFE and FSF. In a study on optimization of the front diffusion profile [80], it is reported that the FFE provides higher J_{SC} as compared to the FSF, especially for the higher front SRV condition. In this study, the optimization of the front diffusion profile of IBC solar cells was conducted by applying the bifacial scheme to the cell [81].

5.3 Bifacial IBC solar cell designs [81]

In this section, the results from our study on bifacial IBC solar cell front designs are presented in [81]. This section is composed of the simulation modeling, its results, and discussion.

5.3.1 Simulation modeling

Figure 5.3 shows the simulations of the bifacial IBC solar cell with three illumination conditions: bifacial/front, bifacial/rear, and bifacial/double. In this study, the n-type IBC solar cell has been investigated.

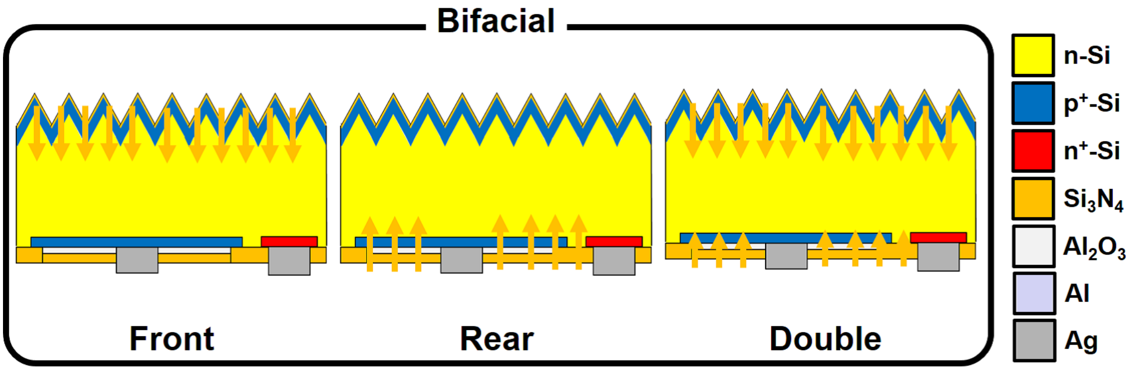

Figure 5.3: Bifacial IBC solar cell simulations for three illumination conditions

Table 5.1 summarizes the modeling parameters in this study. The fundamental parameters are obtained from the previous study on bifacial IBC [82], and the detailed process parameters are described in the literature [83].

Here, the IBC solar cell has a multidimensional rear structure; thus, 3D modeling is appropriate. However, considering the simulation time and convergence, 2D modeling is used in this study with three confinements: the rear electrode area is increased to include the busbar area, the difference in the contact structure is expressed by the contact resistivity, and the effect of the rear emitter and BSF structure is expressed by the emitter-BSF pitch surface recombination velocity [70]. The bold characters in the table correspond to these confinements.

Table 5.1: Modeling parameters

Parameter	**Symbol**	**Value**
Bulk property [82]		n-type Cz-Si
Bulk resistivity [82]	$\rho_{emitter}$	1 Ω-cm
Emitter profile [82]	$\rho_{emitter}$	60 Ω/sq
BSF profile [82]	ρ_{BSF}	100 Ω/sq
Bulk thickness [83]	T_{bulk}	170 μm
Periodic width of cell [82]	W_{cell}	2,200 μm
Emitter width [82]	$W_{emitter}$	1,650 μm
BSF width [82]	W_{BSF}	530 μm
Emitter-BSF pitch width [82]	W_{pitch}	10 μm
Bulk lifetime [44]	τ_{bulk}	5 ms
Front surface reflectance [23]		Flat surface with texture R-T random scattering
Internal light reflectance	R_{front} R_{Ag} $R_{rear(mono)}$ $R_{rear(bi)}$	85% (R_{front}) 80% (R_{Ag}) 90% ($R_{rear(mono)}$) 80% ($R_{rear(bi)}$)
The surface recombination velocity [26, 27]	S_{front} $S_{emitter}$ S_{BSF} S_{pitch}	$C_S/1 \times 10^{16}$ cm/s (S_{front}) 2,000 cm/s ($S_{emitter}$) 500 cm/s (S_{BSF}) **40,000 cm/s** (S_{pitch})
Contact resistivity	$\rho_{contact}$	**15 mΩcm^2**
Electrode width [82]	W_{elec}	$60 + W_{cell} \times (800(busbarwidth)/17,500(busbarpitch))$ $\boldsymbol{\mu}$**m**

The result of the simulation is shown in Fig. 5.4. Furthermore, the front- and rear-surface light reflectances are shown in Fig. 5.5. The rear-surface light reflectance is calculated by the TMM optical solver with an 80 nm thick Si_3N_4 passivated condition.

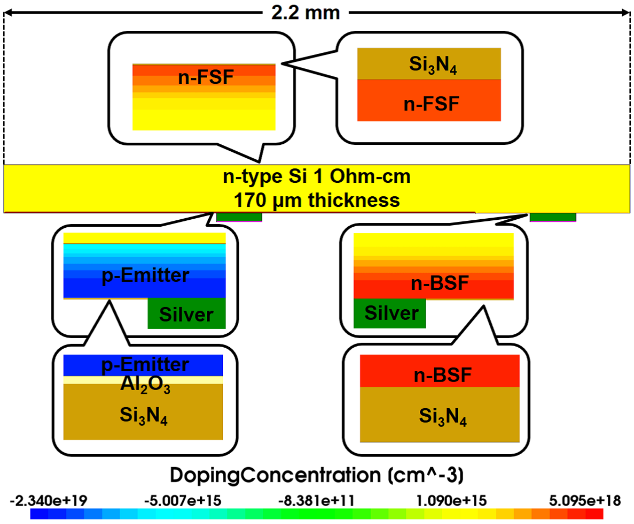

Figure 5.4: Bifacial IBC solar cell simulation modeling

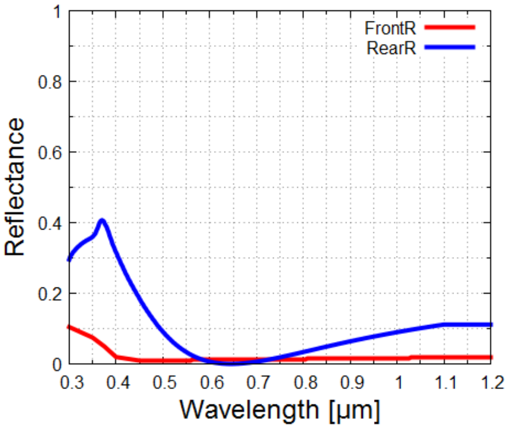

Figure 5.5: Front- and rear-surface light reflectances

The J-V characteristics of the three conditions are shown in Fig. 5.6. Furthermore, the J-V parameters are compared to the experimental results [82] listed in Table 5.2. The comparisons prove that the modeling results agree with those obtained from the experiments.

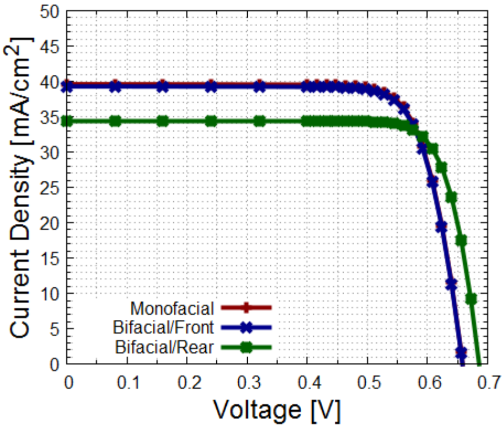

Figure 5.6: J-V characteristics of the three conditions

Table 5.2: J-V parameters of modeling for the comparison with the experimental results of bifacial IBC

Condition	J_{SC} **[mA/cm^2]**	V_{OC} **[mV]**	FF [%]	η [%]
Monofacial	39.6 (±0.0)	658 (-2)	78.6 (-0.3)	20.4 (-0.2)
Bifacial/front	39.3 (+0.3)	658	78.7	20.3
Bifacial/rear	34.4 (-0.1)	686	81.0	19.0

The additional simulation that evaluated the bulk lifetime effect is shown in Fig. 5.7. It is difficult to determine the bulk lifetime accurately, and it can affect the cell performance. The simulation results show that a bulk lifetime of higher than 1 ms is sufficient to ensure the performance. The results also support the reliability of the modeling.

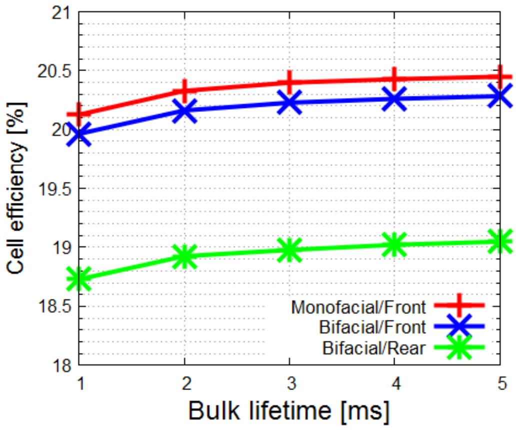

Figure 5.7: Cell efficiencies obtained under the three conditions against bulk lifetime

5.3.2 Bifacial IBC: Bifacial/front

Figure 5.8 shows the cell performances of bifacial IBC under the bifacial/front condition against front doping of both FFE and FSF. In this case, as a comparison, the non-front doping condition with the S_{front} of 10 cm/s is plotted as a dashed-line. The entire performance is improved by the adoption of the FFE scheme; however, only the FF performance of the FSF scheme is better. The characteristic of the J_{SC} improvement by the FFE scheme is observed, which leads to an improvement in V_{OC} and η as a consequence. The difference in the maximum cell

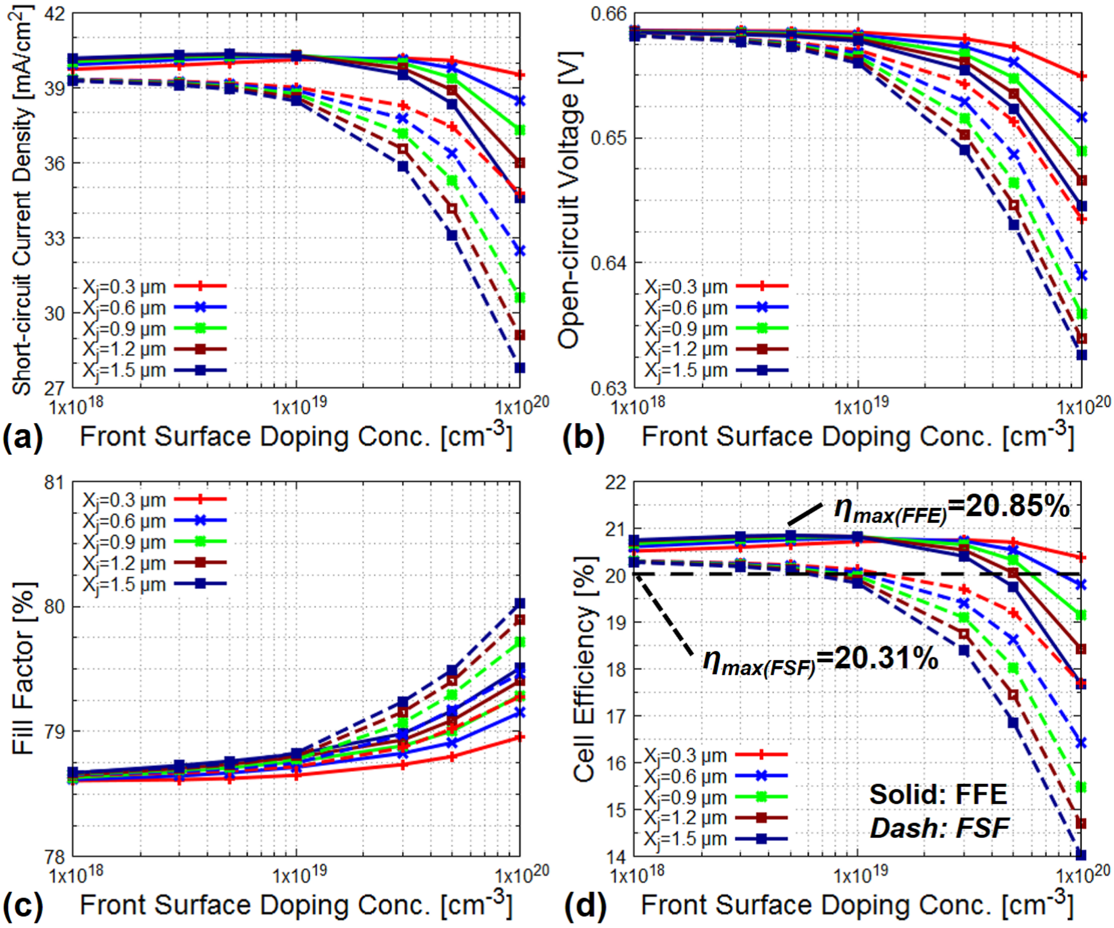

Figure 5.8: Cell performances of bifacial IBC under the bifacial/front condition against front doping

efficiency is approximately 0.5%, with $\eta_{FFE} = 20.85\%$ and $\eta_{FSF} = 20.31\%$.

For optimization, the FFE has the trade-off that the optimized profile is the following: the front surface concentration $C_S = 5 \times 10^{18}$ cm^{-3} and the diffusion depth $X_j = 1.5$ μm are the most appropriate values. Moreover, the FSF shows that lighter doping, that is, $C_S = 1 \times 10^{18}$ cm^{-3} and a diffusion depth of $X_j = 0.3$ μm are the optimum values. The FFE works as a temporary minority-carrier collector, and the deeper diffusion depth is suitable for collecting carriers. Moreover, the FSF is the field-effect passivation region; thus, the diffusion depth is not important. In contrast, heavier front doping causes increased carrier recombination and is disadvantageous.

This bifacial/front performance composes the main performance in a bifacial/double situation; therefore, the results of this situation are important for understanding the FFE and FSF characteristics of the bifacial IBC.

5.3.3 Bifacial IBC: Bifacial/rear

The bifacial/rear performances of the bifacial IBC against front doping of both FFE and FSF are shown in Fig. 5.9. In contrast to the bifacial/front condition, the bifacial/rear condition shows different trends against front doping. The most important factor is that the FSF scheme is better in this situation; however, advantage of the cell efficiency against the FFE scheme is within 0.1%. The rear-side illumination generates carriers mainly to the rear side, wherein the emitter and BSF are concentrated. Therefore, the carrier-transport problem, which is

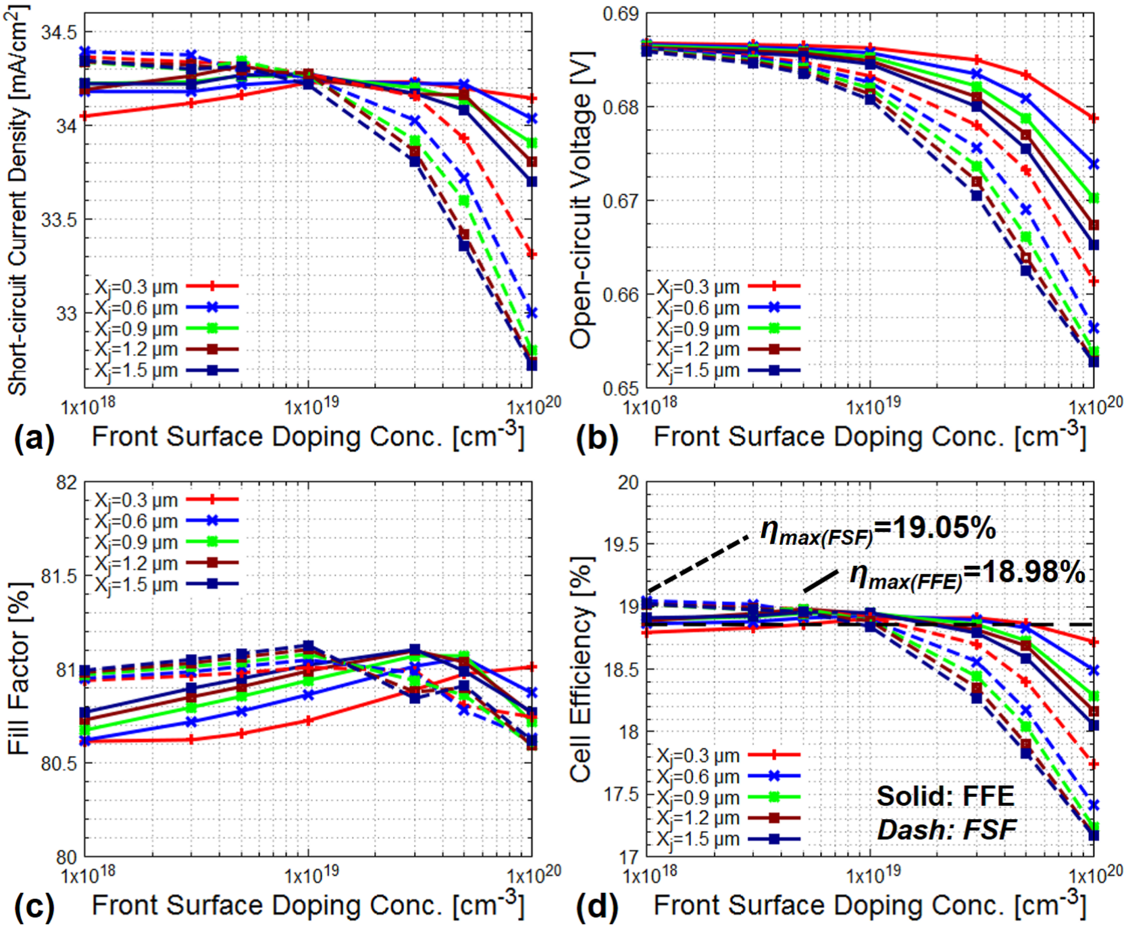

Figure 5.9: Cell performances of bifacial IBC under the bifacial/rear condition against front doping

important for front-side illumination is less important, and the effect of the FFE is small. Moreover, the FSF characterization of the field-effect passivation works generally; therefore, the adoption of the FSF scheme is better in this situation.

The J_{SC} at the lighter front surface doping is almost equal between the FFE and FSF schemes. In this case, V_{OC} of the FSF scheme is lower than that of the FFE scheme, which indicates that the FFE of the temporary minority-carrier collection region maintains the minority-carriers from recombination and improves the V_{OC} performance. The FF performance improves by adopting the FSF scheme, and consequently, the total performance of the cell efficiency is improved by the FSF scheme.

Similar to the bifacial/front situation, the front doping optimization shows similar trends in both the FFE and FSF schemes. The FFE shows the optimized profile of $C_S = 5 \times 10^{18}$ cm^{-3} and $X_j = 1.2$ μm. Meanwhile, the FSF shows that a lighter doping of $C_S = 1 \times 10^{18}$ cm^{-3} and $X_j = 0.6$ μm are the best parameters.

5.3.4 Bifacial IBC: Bifacial/double

The bifacial/double situation corresponds to the usage of the bifacial IBC cell on the bifacial module. Figures 5.10 and 5.11 show the bifaciality factor and power density of the bifacial IBC against front doping, respectively. The higher bifaciality factor of the FSF scheme originates from its advantage under the bifacial/rear condition, and even the FFE scheme bifaciality factor is above 0.9, which is significantly higher for the bifacial cells. Because the IBC cell concentrates both the

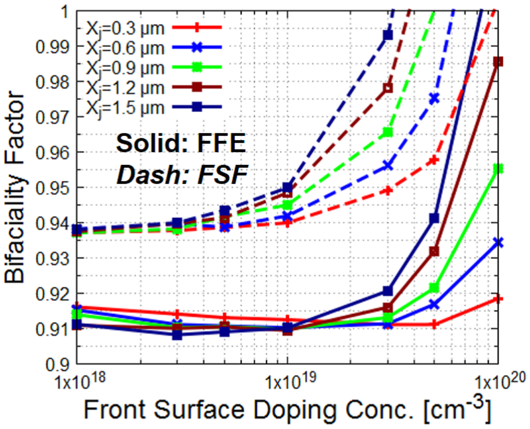

Figure 5.10: Bifaciality factor of bifacial IBC against front doping

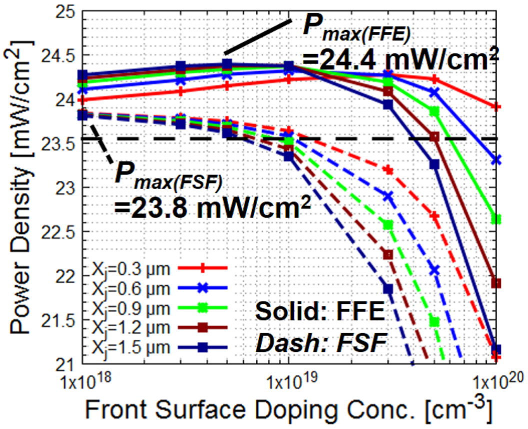

Figure 5.11: Power density of bifacial IBC at the bifacial/double situation against front doping

emitter and the BSF, the bifaciality factor is likely to be high compared to the other cells of the front-side emitter structures.

The power density of 24.4 $\mathrm{mW/cm^2}$ is available by adopting the FFE scheme, which is 0.6 $\mathrm{mW/cm^2}$ higher than that of the FSF scheme. The optimized doping profile comprises the following parameters: $C_S = 5 \times 10^{18}$ $\mathrm{cm^{-3}}$ and $X_j = 1.5$ μm for the FFE scheme, and $C_S = 1 \times 10^{18}$ $\mathrm{cm^{-3}}$ and $X_j = 0.3$ μm for the FSF scheme.

The J_0 value that expresses the diode quality is shown in Fig. 5.12. The $J_0 = J_{SC}/\exp(V_{OC}/V_T)$ $(V_T = kT/q)$ is calculated in a bifacial/double situation against the front doping, and a value below 300 $\mathrm{fA/cm^2}$ is obtained at a lighter surface doping concentration under $1{\times}10^{19}$ $\mathrm{cm^{-3}}$. The heavier doping causes a significant increase in J_0, especially for the FSF scheme. This evaluation shows that the FFE scheme is much more robust against the front-side carrier recombination, which indicates that the FFE region collects minority-carriers as the majority-carriers.

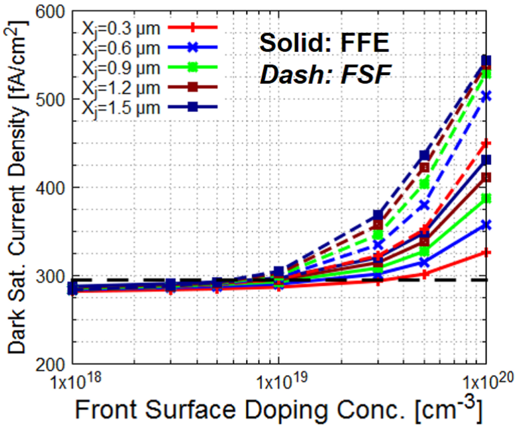

Figure 5.12: J_0 of bifacial IBC under bifacial/double condition against front doping

5.3.5 Cell structure optimization

The FFE improves the lateral-direction carrier transport; therefore, the wider the unit cell, the better the FFE scheme works. The shortening of the unit cell is another solution to avoid the carrier transport problem, in which the FSF scheme may exceed the FFE performance. Figure 5.13 shows the power density of bifacial IBC in the bifacial/double situation against the emitter area percentage for different unit cell widths. Here, the evaluation is performed until the front surface concentration is less than 1×10^{19} cm^{-3} because the heavier doping will increase the recombination loss significantly. Furthermore, the rear contact area shrinks to maintain the rear contact area percentage; therefore, the maximum emitter area percentage decreases at smaller W_{cell} conditions.

The unit cell of width 2,200 μm, which is the value used in the above discussion, is the best in this evaluation; however, the FSF scheme shows better performance than the FFE scheme at a smaller unit cell width. One important factor is that the optimized emitter area percentage is the same between the W_{cell} of 2,200 μm and 1,650 μm. This means that the optimized emitter area is determined by other parameters of the emitter and the BSF sheet resistance (or the emitter-BSF pitch distance) or more. The maximum power density of 24.8 mW/cm^2 was obtained by the FFE scheme with $W_{cell} = 2,200$ μm (see Table 5.3). The larger W_{cell} minimizes the difference between the FFE and the FSF scheme even at 0.1

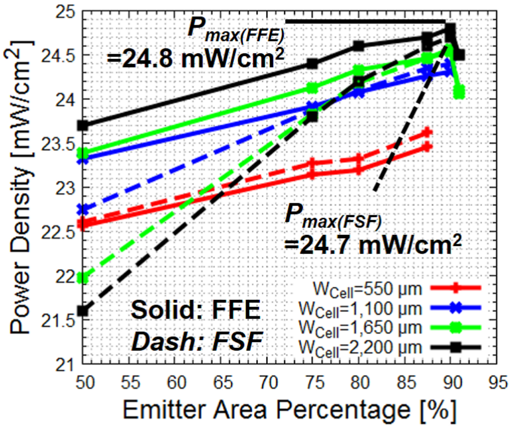

Figure 5.13: Power density of bifacial IBC under bifacial/double condition against emitter area percentage

mW/cm^2 power density performance; however, the FFE scheme provides better performance than the FSF scheme.

Table 5.3: Optimized cell designs of bifacial IBC for both FFE and FSF schemes under bifacial/double condition

Parameter	**FFE**	**FSF**
W_{cell} [μm]	2,200	2,200
$\frac{W_{emitter}}{W_{cell}}$ [%]	90	90
X_j [μm]	1.5	0.6
C_S [cm^{-3}]	3×10^{18}	1×10^{18}
P_{max} [mW/cm^2]	24.8	24.7

5.3.6 IQE mapping

The IQE mapping [82, 84] is a powerful analysis to reveal the dominant cell loss parts. In this study, a 950 nm monochromatic light source with an intensity of 25 μW/cm^2 was used to scan the cell. Both the FFE and the FSF cells with the optimized front diffusion at an emitter area percentage of 75% were used for the analysis.

Figure 5.14 shows the IQE mapping of bifacial IBC for the FFE, FSF, and non-front diffusion schemes. The FFE scheme provides a significantly higher IQE value in the BSF region, which is the key to high performance with the adoption of the FFE scheme. The FSF scheme shows an increased IQE value, which is comparable to that of the non-diffusion scheme. In summary, the FFE scheme improves recombination loss in the BSF region drastically, and the FSF scheme improves the entire recombination loss.

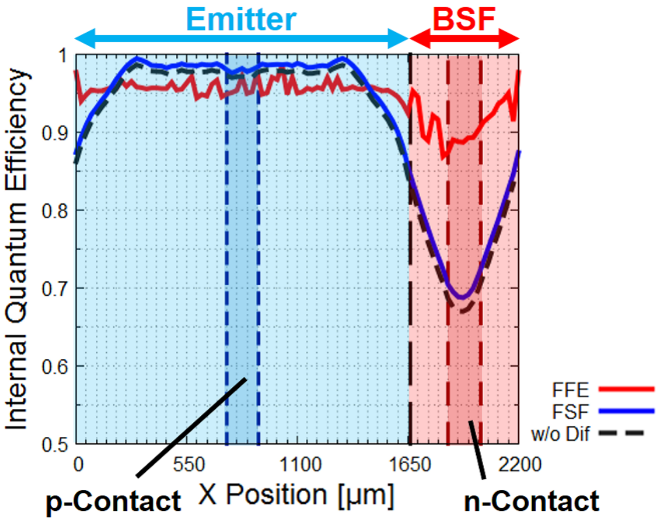

Figure 5.14: IQE mapping of bifacial IBC

5.3.7 Loss analysis

Several loss analysis methods have been proposed. In this study, the power (or the current) density-based loss analysis is used to reveal the loss components at the MPP condition [85], and the free energy loss analysis (FELA) [86,87] is used to obtain the recombination power loss distributions.

The power density-based loss analysis is composed of the optical, recombination, and resistive loss components. By setting the maximum power density to 29.49 mW/cm^2 from the theoretical efficiency limit of 29.4% [88] and the AM1.5G spectrum power of 100.3 mW/cm^2, the optical losses of the shading loss $P_{shading}$ (zero in IBC solar cell), the imperfect light trapping $P_{Imperfect}$, the absorbed and not-generated carriers P_{NonGen}, the recombination losses of P_{SRH}, P_{Auger}, and P_{Rad}, and the resistive losses of P_{Series} and P_{Shunt} are considered. The optical losses are calculated by the number of photons of each component p_{Input} (input photons), $p_{Escaped}$ (escaped photons), $p_{Absorbed}$, the electrode shading coverage S_{Elec} and quantum yield QY as

$$\begin{aligned} P_{Shading} &= (p_{Input} \times S_{Elec})/p_{Input} \times 29.49, && (5.1)\\ P_{Imperfect} &= (p_{Escaped} - p_{Shading})/p_{Input} \times 29.49, && (5.2)\\ P_{NonGen} &= (p_{Absorbed}(1 - QY))/p_{Input} \times 29.49. && (5.3) \end{aligned}$$

The resistive loss is expressed by R_S and R_{Shunt} as

$$\begin{aligned} P_{Series} &= R_S J_{mpp}^2, && (5.4)\\ V_{Shunt} &= V_{mpp} + R_S J_{mpp}, && (5.5)\\ P_{Shunt} &= V_{Shunt}^2 / R_{Shunt}. && (5.6) \end{aligned}$$

The ratio of SRH R_{SRH}, Auger R_{Auger}, and radiative recombination R_{Rad} for the entire cell volume to the total recombination are used to express the recombination power loss P_{SRH}, P_{Auger}, and P_{Rad}. By setting the total loss as P_{Rec},

$$P_{Rec} = 29.49 - (P_{Opt} + P_{Res}), \quad (5.7)$$

$$P_{SRH,Auger,Rad} = \frac{\int_V R_{SRH,Auger,Rad} dV \times P_{Rec}}{\int_V R_{SRH} dV + \int_V R_{Auger} dV + \int_V R_{Rad} dV}. \quad (5.8)$$

From the above expressions, the loss analysis of bifacial IBC is evaluated, as shown in Fig. 5.15. Here, the power density is 1.2× by considering rear-side illumination, and it seems that the rear-side shading is included in the imperfect light trapping. The main difference between the FFE, FSF, and non-diffusion schemes appears in the SRH recombination and Auger recombination components. The FFE scheme of the smaller losses in the BSF region contributes to it, and the FSF scheme suppresses the entire loss from the non-diffusion scheme.

Another loss analysis of the FELA is used to illustrate the recombination loss distribution. The FELA uses the free energy of the difference of the quasi-Fermi energy of electrons and holes $\Delta E_F = E_{Fn} - E_{Fp}$ to express the loss parts. For the recombination power loss Φ_R, it is expressed as

$$\Phi_R = \text{abs}((R_{SRH} + R_{Auger} + R_{Rad}) \times (E_{Fn} - E_{Fp})). \tag{5.9}$$

Figure 5.16 shows the FELA recombination loss distribution of bifacial IBC for both the FFE and FSF schemes. The FFE scheme shows the suppressed recombination power density at the BSF region, which corresponds to the above

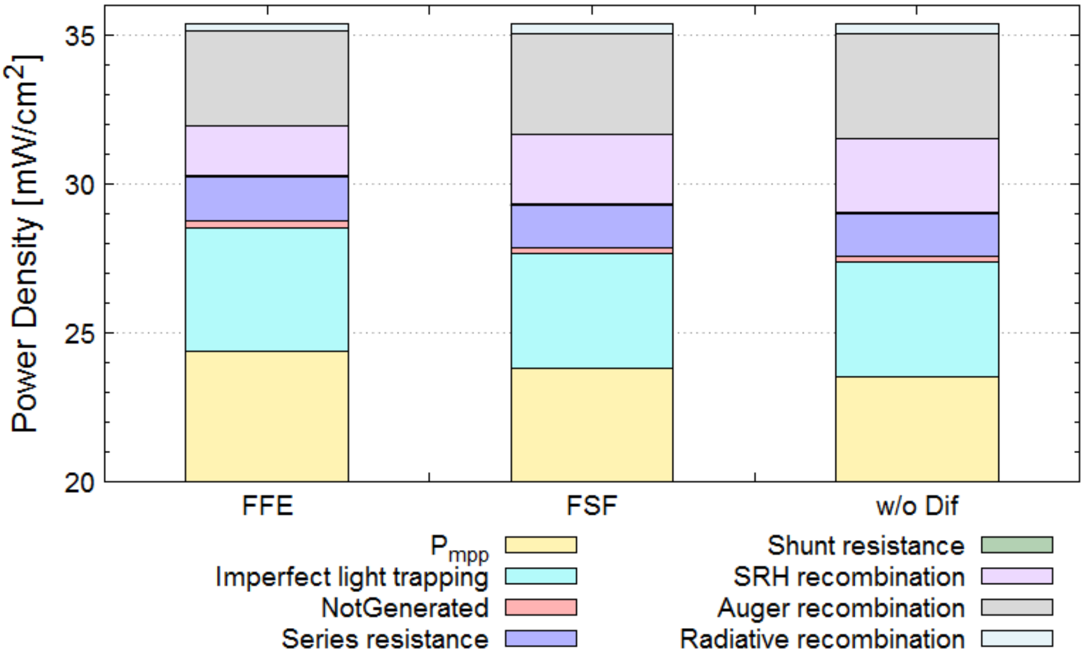

Figure 5.15: Loss analysis of bifacial IBC

loss analysis. The emitter region exhibits a smaller recombination loss power density; however, the surface regions are high-recombination parts.

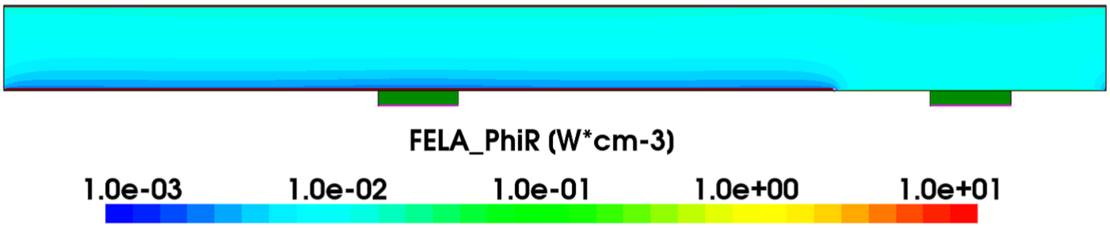

(a) FFE

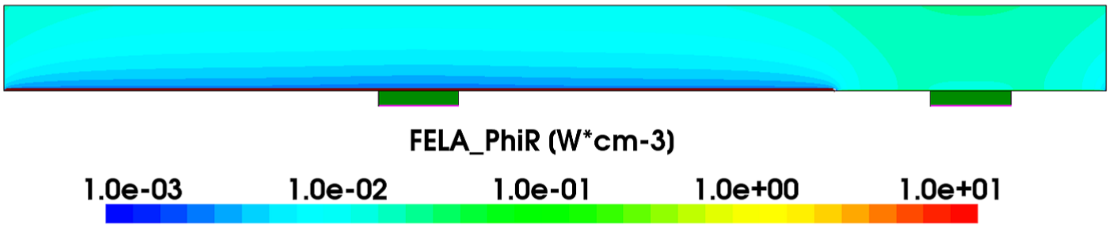

(b) FSF

Figure 5.16: FELA recombination loss distribution of bifacial IBC

5.3.8 Conclusion

The optimizations of the front diffusion of bifacial IBC to compare the FFE and FSF schemes have been performed. The FFE yielded better results in the front-side and bifacial performances by enhancing the lateral-carrier transport to avoid the loss of the BSF region. Moreover, the FSF showed better rear-side performance by field-effect passivation and carriers pushing back to the rear-side carrier collection regions. The FFE showed optimized diffusion profiles, and the FSF showed lighter diffusion profiles to achieve the desired performance.

The unit cell effect was evaluated, and it was observed that the smaller unit cell made the FSF better. However, the larger unit cell of 2200 μm was the best in the evaluation. The FFE scheme of the rear emitter area of 90% was the optimum design.

The IQE mapping showed that the FFE scheme avoided the BSF region loss significantly, and the FSF scheme improved the entire cell recombination performance. The loss analysis revealed that the FFE scheme suppressed the bulk and auger recombination from the other methods, which corresponded to the FELA recombination power density distributions.

Chapter 6

TOPCon Solar Cells

6.1 Characterization of TOPCon solar cell

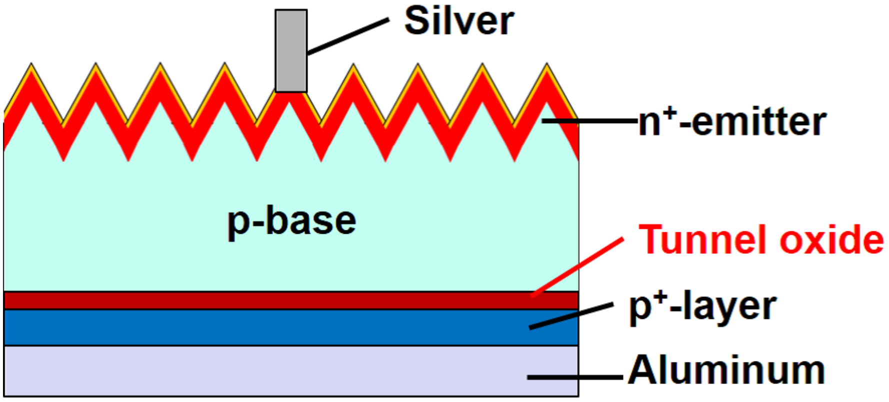

Figure 6.1: p-TOPCon solar cell structure [7]

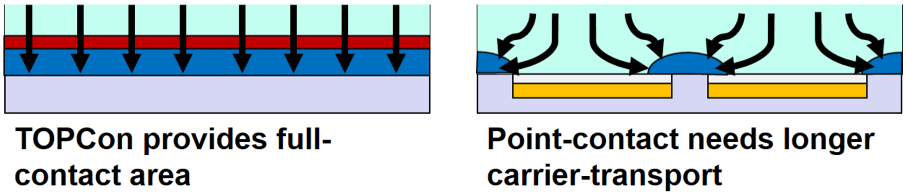

Figure 6.2: carrier-transport of TOPCon and the point-contact

Tunnel oxide passivated contact (TOPCon) is a newer advanced c-Si solar cell structure that was proposed in 2014 [7]. This TOPCon structure is expected to be the next major innovation after PERC [89, 90]. The feature of TOPCon solar cells is the carrier selective contact realized by the tunnel oxide; thus, only the majority-carrier can pass the tunnel oxide.

TOPCon solar cells solve the problem in PERC of the increased internal resistance by the restricted contact area, wherein the full-area tunnel oxide provides 1D-carrier transport and reduces carrier transport length as compared to the multidimensional carrier transport in partial contact structures, such as PERC (see Fig. 6.2) [90]. By the TOPCon's 1D-carrier transport and the carrier selective contact provided by the tunnel dielectric layer, it succeeded in being compatible with both the high V_{OC} (recombination part) and FF (resistive part). However, the lack of a rear passivation layer with a higher internal light reflectance may be slightly disadvantageous in terms of the optical performance.

There is an 'i-TOPCon', implying 'industrial-TOPCon', which the rear point-contact scheme has adopted [91]. This i-TOPCon is a combination of the PERC technology and the TOPCon technology, which exhibited 24.58% cell efficiency.

The carrier tunnel at the Si/dielectric layer is determined by the thickness of the dielectric layer; the thinner dielectric layer passes both the majority- and the minority-carrier currents, and the thicker dielectric layer inhibits both the majority- and the minority-carrier currents; therefore, the optimization of the

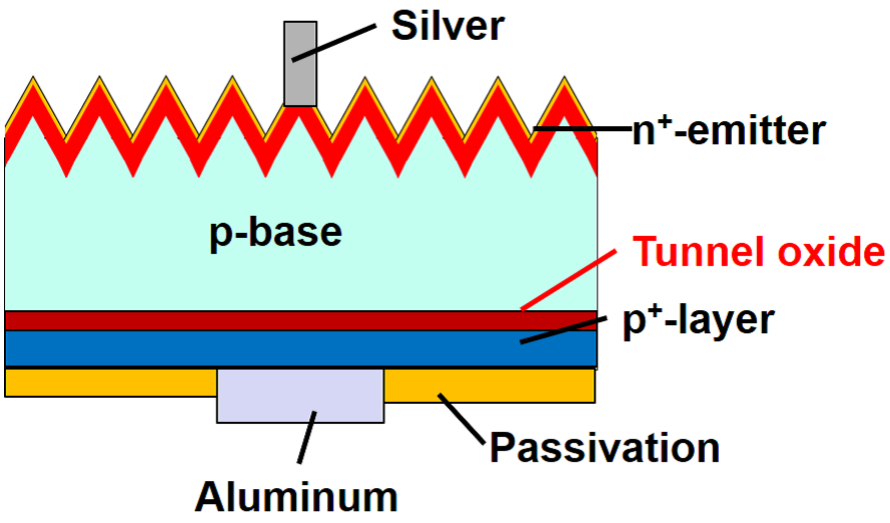

Figure 6.3: i-TOPCon solar cell structure [91]

dielectric layer thickness is important (see Fig. 6.4).

Furthermore, the carrier tunnel is affected by the tunnel parameters: the effective masses, the Si/dielectric interface band structures of both the electron and the hole, and relative permittivity. This carrier-tunnel is based on the direct tunnel model that Schenk proposed [92]. The model aimed at reducing the CPU time with an effective calculation method, which the model application has introduced in [93, 94].

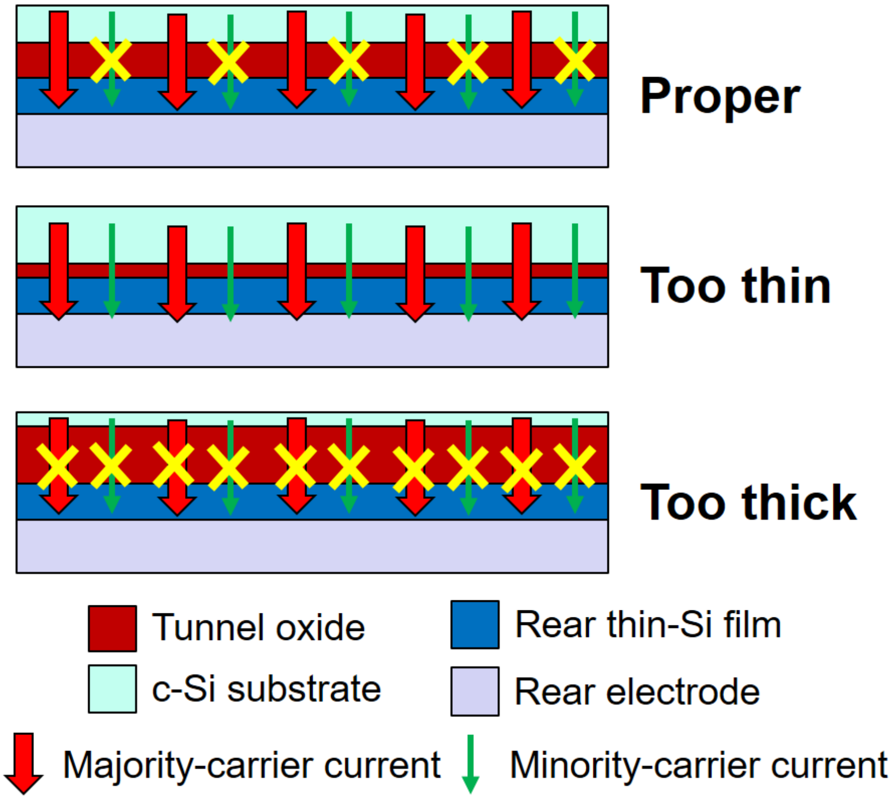

Figure 6.4: Carrier selective contact regarding the thickness of tunnel oxide

6.2 Carrier tunnel in TOPCon solar cells

The carrier tunnel is a key mechanism in TOPCon solar cells. The Si/dielectric interface has different band offsets between the electrons and the holes, which provides carrier selective contact. The important parameters of direct carrier tunneling are the dielectric constant, band offsets at the Si/interface, and effective masses. These parameters are unique material values; thus, the selection of the tunnel dielectric material is an important factor to be considered while designing TOPCon solar cells. The typical and prospective dielectric material's parameters are listed in Table 6.1.

Table 6.1: Tunnel parameters of Si/dielectric interface

Parameters	**Symbol**	**SiO_2**	**Si_3N_4**	**Al_2O_3**	**TiO_2**	**HfO_2**
Relative permittivity	ε_{OX}	3.9 [47]	7.5 [47]	9.1 [47]	12 [99]	22 [102]
Electron tunnel mass	m_e/m_0	0.40 [95]	0.50 [95]	0.41 [96]	10 [99]	0.11 [103]
Hole tunnel mass	m_h/m_0	0.32 [95]	0.41 [95]	0.36 [96]	0.8 [99]	0.29 [104]
Electron barrier [eV]	Φ_e	3.1 [95]	2.1 [95]	2.9 [97,98]	-0.22 [100]	2.1 [102,103]
Hole barrier [eV]	Φ_h	4.5 [95]	1.9 [95]	3.4 [97,98]	2.2 [100]	2.6 [102,103]
Fixed charge		Positive [90]	Positive [90]	Negative [90]	Negative [101]	Positive [105]

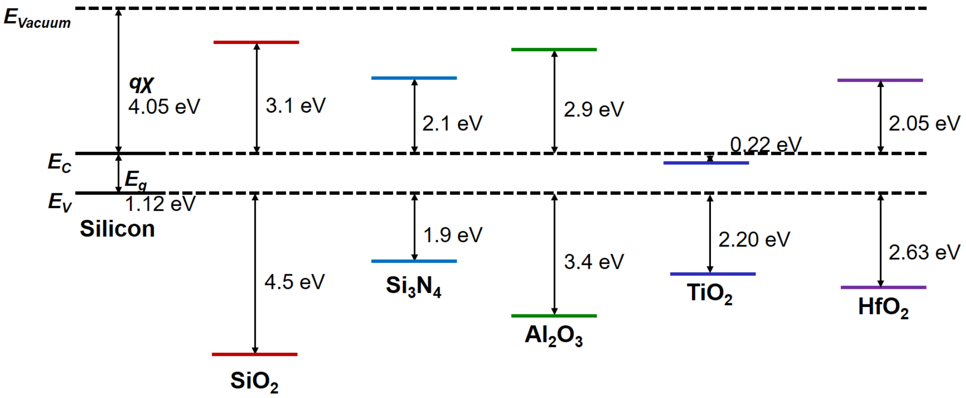

Figure 6.5: Band structure of Si/dielectric interface

Note that the tunnel parameters of many dielectric materials are not determined strictly, and there are differences between reports [106, 107]; however, the parameters used in this study are cited from the latest articles as much as possible. The tunnel parameter of Si is the DOS effective mass m_C, which is 1.18 for electrons and 0.81 for holes [108]. The Si effective mass m_{Si}, which is 0.19 for electrons and 0.16 for holes, was used [47].

The prospective materials of HfO_2 are called as 'high-κ' dielectrics [109], which are generally used in CMOS devices. They find applications in solar cells as the tunnel layers are not studied extensively, and they have the potential of improving the cell performances.

6.3 Carrier tunnel modeling [92, 94]

The carrier tunnel modeling is necessary to evaluate TOPCon solar cells. In this study, the tunnel modeling proposed by Schenk et. al. [92], which it is generally mentioned as "Direct Tunneling Model," is used. Here, the summarization of the modeling from the literature [92, 94] is provided.

The model introduces the transmission coefficient (TC) $\Gamma(E)$ to reduce the calculation time of the device simulation with sufficient precision. The electron tunnel current is expressed as follows:

$$j_n = \frac{qm_C^* k_B T}{2\pi^2 \hbar^3} \int_0^\infty dE\Gamma(E) \times \ln \left\{ \frac{\exp[\frac{E_{F,S}(d)-E_C(d)-E}{k_B T}]+1}{\exp[\frac{E_{F,M}(0)-E_C(d)-E}{k_B T}]+1} \right\}. \tag{6.1}$$

where q is the elementary charge, m_C^* is the conductivity mass, k_B is the Boltzmann constant, $E_{F,S}(d)$ is the substrate Fermi energy at the semiconductor/oxide interface, $E_{F,M}(0)$ is the gate Fermi energy, $E_C(d)$ is the conduction band energy at the semiconductor/oxide interface, and T is the temperature. The equation assumes the independent particle approximation, incoming and outgoing states as plane waves, and the trapezoid shape barrier and parabolic $E_(k)$ relation in the barrier region are approximated for the 1D solution of TC. For $\Gamma(E)$, it is expressed as follows:

$$\Gamma(E) = \frac{2}{1+g(E)}, \tag{6.2}$$

and then $g(E)$ is

$$\begin{aligned} g(E) = \frac{\pi^2}{2}\{ & \frac{m_{Si}k_F}{m_M k_{Si}} (Bi'_d Ai_0 - Ai'_d Bi_0)^2 \\ & + \frac{m_M k_{Si}}{m_{Si} k_F} (Bi_d Ai'_0 - Ai_d Bi'_0)^2 \\ & + \frac{m_M m_{Si}}{\lambda_0^2 m_{ox}^2 k_F k_{Si}} (Bi'_d Ai'_0 - Ai'_d Bi'_0)^2 \\ & + \frac{\lambda_0^2 m_{ox}^2 k_F k_{Si}}{m_M m_{Si}} (Bi_d Ai_0 - Ai_d Bi_0)^2 \}, \end{aligned} \tag{6.3}$$

with

$$Ai_0 \equiv Ai\left(\frac{\Phi_B - E}{\hbar\Theta_{ox}}\right), \quad Ai_d \equiv Ai\left(\frac{\Phi_B + qF_{ox}d - E}{\hbar\Theta_{ox}}\right). \tag{6.4}$$

Φ_B is the barrier height for electrons, and m_M, m_{ox}, and m_{Si} are the effective electron masses for metals, oxides, and semiconductors, respectively. k_F and k_{Si} are the momenta in the electrodes, and A_i and B_i are the Airy functions. λ_0 and $\hbar\Theta_{ox}$ are expressed as follows:

$$\lambda_0 = \frac{\hbar\Theta_{ox}}{qF_{ox}}, \tag{6.5}$$

$$\hbar\Theta_{ox} = (\frac{q^2\hbar^2F_{ox}^2}{2m_{ox}})^{1/3}. \tag{6.6}$$

The model includes the image potential with a simple approximation of a straight continuation of the band edge. This approximation allows errors only at the edges of the barrier. Here, the image potential is expressed as follows:

$$\begin{aligned} E_{im}(x) = \frac{q^2}{16\pi\epsilon_{ox}} \sum_{n=0}^{\infty} (k_1k_2)^n, \\ \times \left[\frac{k_1}{nd+x} + \frac{k_2}{d(n+1)-x} + \frac{2k_1k_2}{d(n+1)}\right]. \end{aligned} \tag{6.7}$$

Here, k_1 and k_2 are

$$k_1 = \frac{\epsilon_{ox}-\epsilon_M}{\epsilon_{ox}+\epsilon_M} = -1, \quad k_2 = \frac{\epsilon_{ox}-\epsilon_{Si}}{\epsilon_{ox}+\epsilon_{Si}}, \tag{6.8}$$

The approximation with image force for barrier lowing is the effective solution. Introducing $\Gamma(E)$ with image force reduces more CPU time than that reduced using the Schrödinger equation. The barrier potential is mapped as a trapezoid with the following equation:

$$S_{tra}(E) = S_{im}(E). \tag{6.9}$$

Here, $S_{tra}(E)$ and $S_{im}(E)$ are expressed as follows:

$$\begin{aligned} S_{tra}(E) = \frac{2}{3}\{\left[\frac{\Phi_B(E)-E}{\hbar\theta_{ox}}\right]^{3/2} - \left[\frac{\Phi_B(E)+qF_{ox}d-E}{\hbar\theta_{ox}}\right]^{3/2} \\ \times \Theta\left[\Phi_B(E)+qF_{ox}d-E\right]\} \end{aligned} \tag{6.10}$$

$$S_{im}(E) = \sqrt{\frac{2m_{ox}}{\hbar^2}} \int_{x_l(E)}^{x_r(E)} d\xi \sqrt{\Phi_B + qF_{ox}\xi + E_{im}(\xi) - E} \tag{6.11}$$

$x_{l,r}(E)$ are the turning points that can be expressed in the carrier energy as follows:

$$\Phi_B + qF_{ox}x_{l,r} + E_{im}\left(x_{l,r}\right) = E., \tag{6.12}$$

Finally, $\Phi_V(E)$ is approximated by three energy values of E_j $(j = 0, 1, 2)$, which is expressed as follows:

$$\begin{aligned}\Phi_B\left(E\right) = \Phi_B\left(E_0\right) &+ \frac{\Phi_B\left(E_2\right) - \Phi_B\left(E_0\right)}{\left(E_2 - E_0\right)\left(E_1 - E_2\right)}\left(E - E_0\right)\left(E_1 - E\right) \\ &- \frac{\Phi_B\left(E_1\right) - \Phi_B\left(E_0\right)}{\left(E_1 - E_0\right)\left(E_1 - E_2\right)}\left(E - E_0\right)\left(E_2 - E\right)\end{aligned} \tag{6.13}$$

The above discussion focused on electrons; however, this model can be applied to holes. The input parameters listed in Table 6.1 determine the carrier tunnel at the Si/oxide interface.

6.4 Evaluation of tunnel dielectric materials [110]

The evaluation of tunnel dielectric materials for TOPCon solar cells is performed [110]. The fixed charge of tunnel dielectric materials will affect the cell performance, and suitable and non-suitable materials are determined by the bulk doping type. Thus, the combination of the bulk type and the tunnel materials must be studied.

6.4.1 Simulation modeling

The evaluation is based on the experimental results of TOPCon solar cell, which is the highest cell efficiency result at the rear-side carrier selective contact structure [111] (the detailed information is available in our previous study [112]). Table 6.2 presents the simulation modeling settings.

Here, the Si/dielectric interface SRV of 100 cm/s is determined to obtain a well-matched simulation result, and its value corresponds to the reported SRV value of the suitable bulk and dielectric material combination of approximately 500 cm/s [113].

Table 6.2: Numerical simulation settings in this study

Parameters	**SValue**
Cell periodic width [mm]	1.4 (with periodic BC)
Bulk thickness [μm]	200 [111]
Emitter profile [Ω/sq]	140 [111]
Rear thin-Si profile	$C_S = 1 \times 10^{20}$ cm^{-3}/Thickness = 20 nm
Front electrode coverage [%]	1.1 [90]
Front property	Flat surface (Si_3N_4/Al_2O_3 passivated) with texture R-T data and random scattering [23]
Internal light reflectance [%]	90 (Front), 85 (Rear),
SRV value (Si/front (rear) surface) [cm/s]	500 (front), 10^6 (Rear)
SRV value (Si/tunnel dielectric) [cm/s]	1,000
Contact resistivity [mΩcm^2]	1 [90]

Figures 6.6 and 6.7 show the structure and modeling of TOPCon solar cells, respectively.

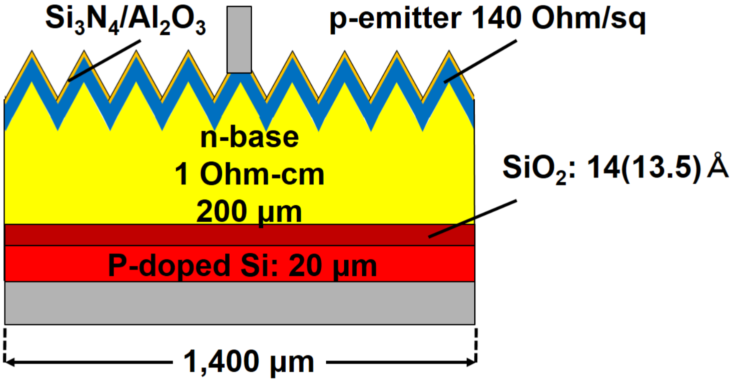

Figure 6.6: Structure of TOPCon solar cells with the experiment [111]

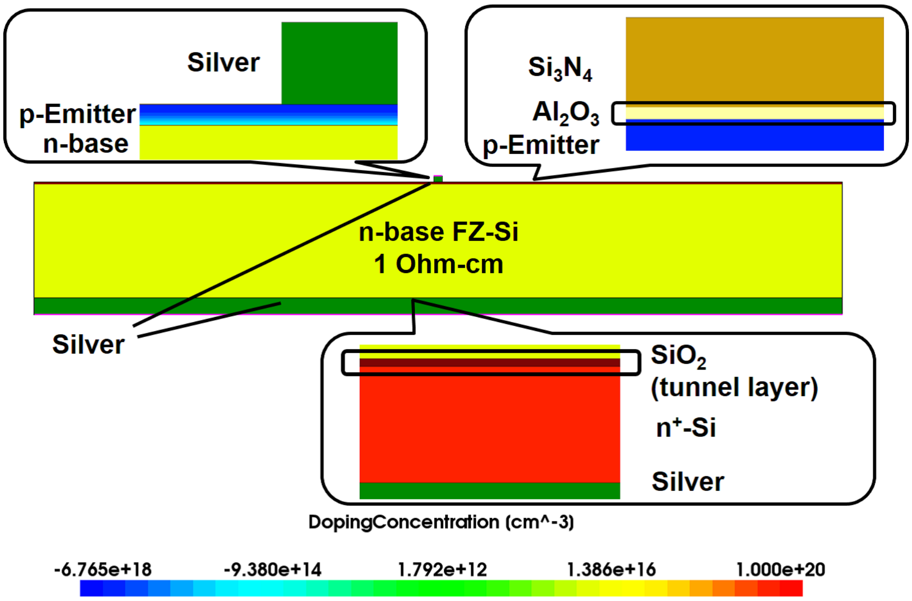

Figure 6.7: Modeling of TOPCon solar cells with the experiment [111]

The simulation result of TOPCon solar cell modeling is shown in Fig. 6.8 as the J-V characteristic and is presented in Table 6.3 as a comparison between the J-V performances and the experimental results.

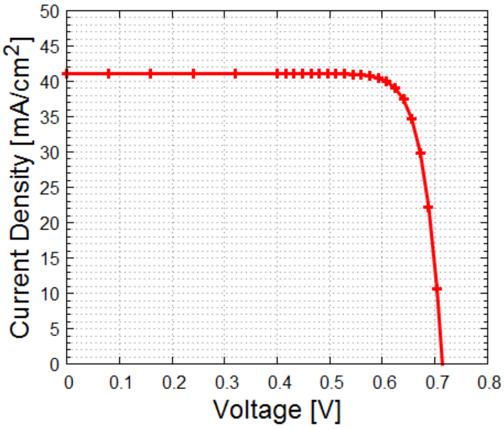

Figure 6.8: J-V characteristic of TOPCon solar cells with the experimental condition

Table 6.3: J-V performance of TOPCon solar cells with simulation and experimental [111] results

Dataset	J_{SC} **[mA/cm^2]**	V_{OC} **[mV]**	FF [%]	η [%]	J_0 **[fA/cm^2]**
Experiment	41.4	713	83.1	24.5	
Simulation	41.1 (-0.3)	714 (+1)	83.1 (±0.0)	24.3 (+0.2)	34.6

The dark J-V characteristics of the TOPCon solar cell modeling are shown in Fig. 6.9. Under the short-circuit condition, a dark current of the order of 1×10^{-10} mA/cm^2 is obtained.

The above results show that the simulation modeling reproduces the experiment well [7]. The following results discuss the effect of the tunnel dielectric material and bulk-type selections on the cell performance.

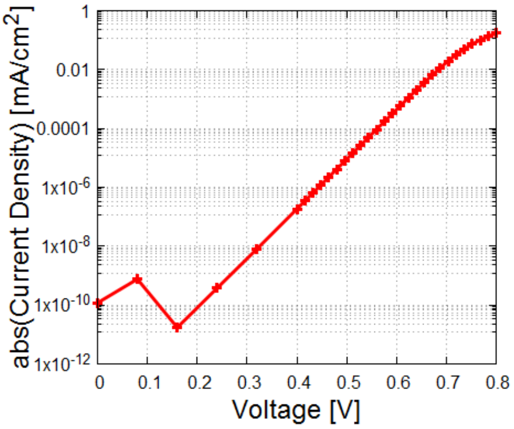

Figure 6.9: Dark J-V characteristic of TOPCon solar cells with the experimental condition

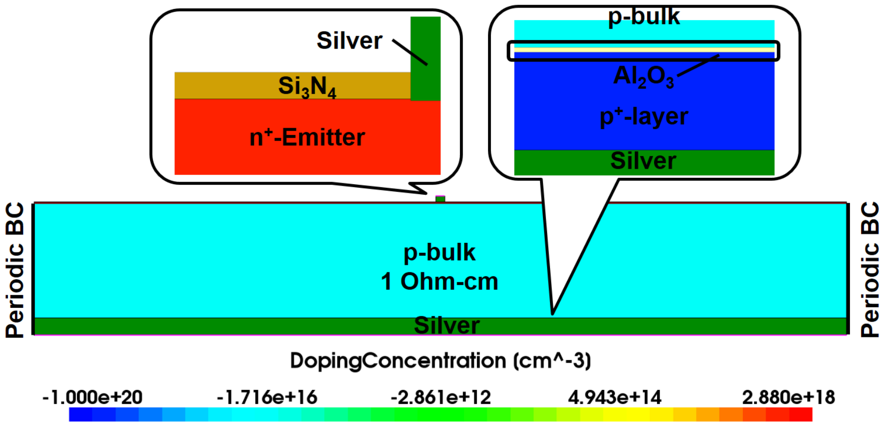

Figure 6.10: Simulation modeling of p-TOPCon

6.4.2 Dielectric materials and bulk type

Figure 6.11 shows the J-V performances of p-type TOPCon solar cells for different tunnel dielectric materials against the dielectric thickness. The TiO_2 TOPCon shows a different trend because of the negative value of the conduction band offset that does not work as the carrier selective contact. For other dielectric materials, the maximum cell performances are almost the same as about 23% cell efficiency, only the thickness at which the cell performance decreases. This means that the different dielectric materials only appear as tunnel parameter effects, and the fixed charge effect does not appear. For p-TOPCon, the bulk lifetime is not high at 150 μs in this study ($\rho_{bulk} = 1$ Ω-cm). Thus, the difference in the SRV at the Si/dielectric is not dominant in the cell performance.

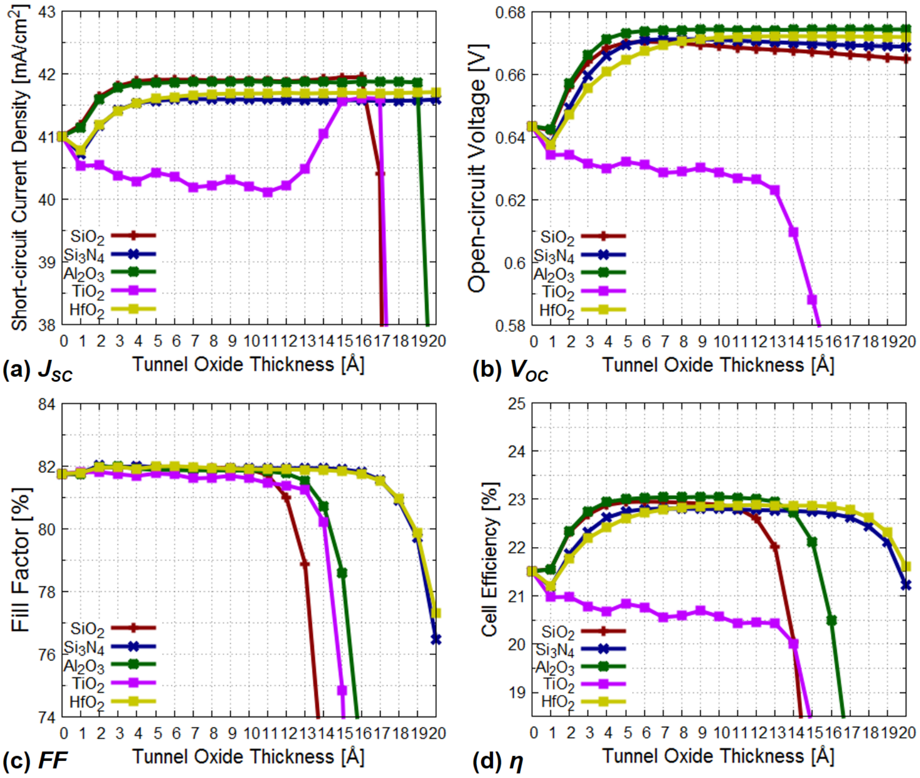

Figure 6.11: J-V performances of p-TOPCon for different tunnel dielectric materials against the dielectric thickness

The use of p-type bulk with BO-cluster deactivation [38] was evaluated, as shown in Fig. 6.12. The trend against the tunnel dielectric thickness is similar to that of p-TOPCon; however, the cell performance is entirely improved to over 24% for the maximum cell efficiency. One issue is that the maximum cell efficiency differs between the tunnel dielectric materials, that the Al_2O_3 with the negative fixed charge provides a cell efficiency of 24.5%, while other materials provide approximately 24% cell efficiency. This is because of the fixed charge effect, where the bulk lifetime improvement makes its effect dominant on the cell performance.

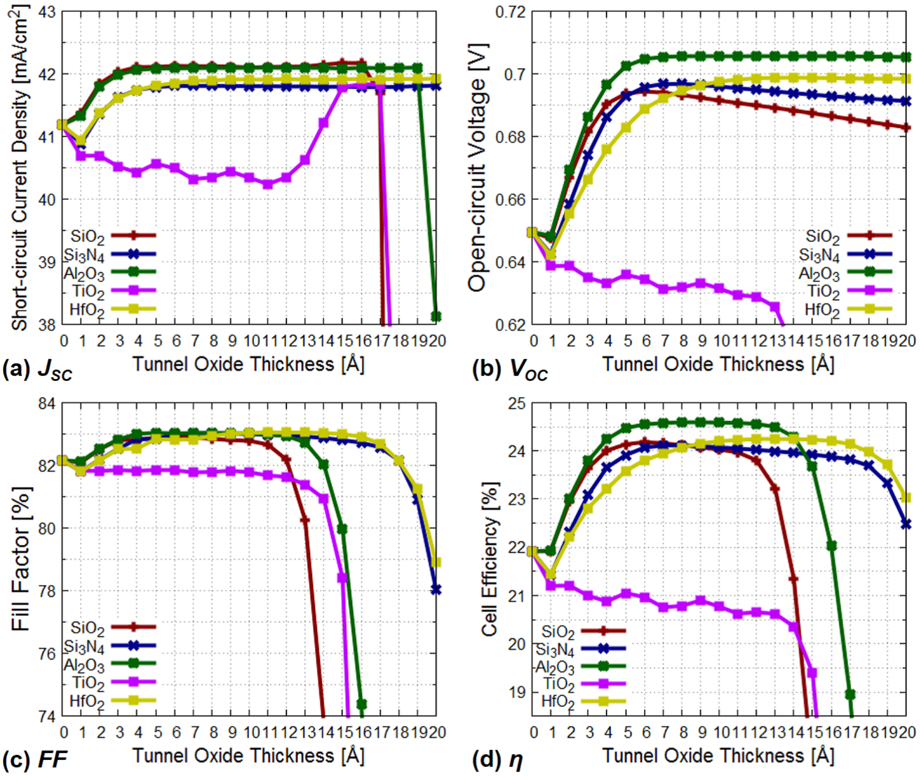

(a) J_{SC} (b) V_{OC} (c) *FF* (d) η

Figure 6.12: J-V performances of p-TOPCon (w/o BO) for different tunnel dielectric materials against the dielectric thickness

Figure 6.13 shows the effect of the fixed charge. The Al_2O_3 and SiO_2 have negative and positive fixed charges, as shown in Table 6.1. At the p-type bulk condition, the maximum cell efficiency is almost the same between the Al_2O_3 TOPCon and the SiO_2 TOPCon; however, by adopting the p-type bulk without a BO-cluster, the cell efficiency difference of approximately 0.5% appears.

The results show that selecting a dielectric material under higher bulk lifetime conditions, including the p- (w/o BO) and n-type bulks, is more difficult than the p-type bulk of the lower lifetime because both the tunnel parameters and the fixed charge effect must be considered.

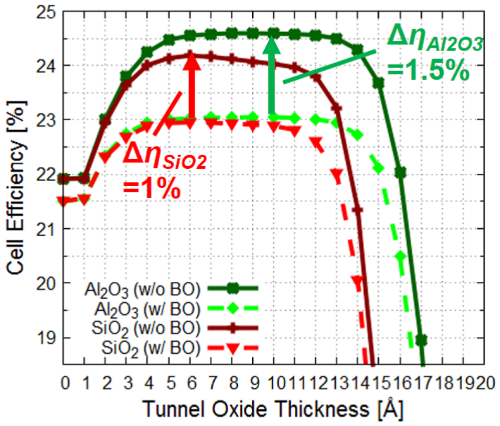

Figure 6.13: Effect of the fixed charge for different bulk quality

The J-V performances of n-TOPCon are shown in Fig. 6.14. TiO_2 shows a flat trend, especially for FF, which is also because of the negative value of the band offset. For cell efficiency, most materials provides a maximum cell efficiency of 24.5%. One important problem is regarding HfO_2, where sufficient cell performance is obtained even at a 3 nm tunnel dielectric thickness, which is not observed in the p-type bulk. This phenomenon makes n-type TOPCon with the HfO_2 tunnel dielectric material because it will drastically ease the control of the tunnel dielectric thickness.

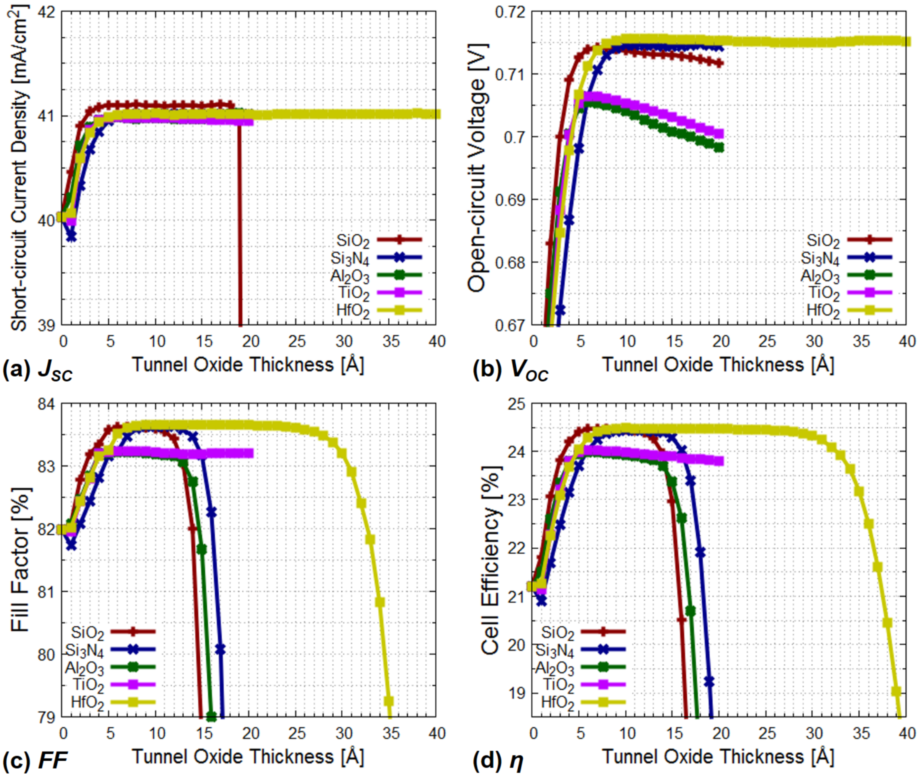
(a) J_{SC}

(b) V_{OC}

(c) FF

(d) η

Figure 6.14: J-V performances of n-TOPCon for different tunnel dielectric materials against the dielectric thickness

6.4.3 Analysis of carrier tunneling

Research on carrier tunneling on TOPCon solar cells is important to improve device performance. Figure 6.15 shows the minority-carrier tunnel current density for both the p-type and n-type bulks. By considering the tunnel dielectric thickness at which the cell efficiency reached its peak, the border minority-carrier tunnel current density that should be below is determined as $J_{tunnel} = 0.2$ mA/cm^2. The tunnel current density decreases as the thickness increases; however, an excessively thick tunnel dielectric will also decrease the majority-carrier tunnel current density, which causes a drop in J_{SC} and FF.

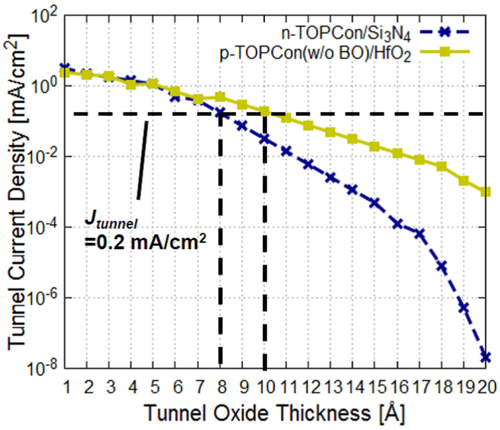

Figure 6.15: Tunnel current density of the minority-carriers against the tunnel dielectric thickness

The estimation of the maximum tunnel dielectric thickness is useful for designing TOPCon solar cells. From the above discussion, the tunnel dielectric thickness modeling based on the majority-carrier effective mass is verified. Figure 6.16 plots the maximum tunnel dielectric thickness and the approximate function of it. Here, the maximum tunnel dielectric thickness is defined as the thickness at which the cell efficiency first drops under 90% of the maximum cell efficiency. The modeling is determined by the following equation:

$$t_{critical} = -13.7\ln(m_{e,h}/m_0) + 3.60. \tag{6.14}$$

The R^2 value of the derived model is 0.773, which indicates that the derived model is reasonable.

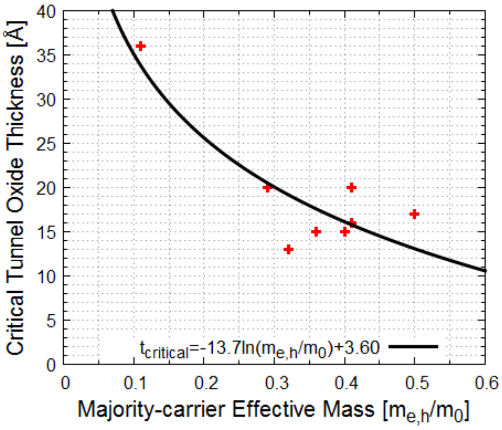

Figure 6.16: Tunnel dielectric thickness modeling based on the majority-carrier effective mass

6.4.4 Improvement of TOPCon solar cell performance

The cell performance improvements by varying the bulk resistivity, that is, the bulk lifetime, were evaluated. The p-TOPCon (w/o BO) with Al_2O_3 tunnel dielectric and n-TOPCon with HfO_2 tunnel dielectric were chosen because they provided the highest performances for each condition.

Figure 6.17 shows the cell performances against bulk resistivity. The most dominant parameter is V_{OC}, where the bulk resistivity is strongly related to the lifetime, and the higher bulk resistivity of the higher bulk lifetime improves cell performance. The maximum cell efficiency of approximately 24.8% is obtained by the p-TOPCon (w/o BO) with Al_2O_3 tunnel dielectric, which is close to the 25% cell efficiency. However, n-TOPCon with HfO_2 provides the V_{OC} of approximately 0.72 V (a significantly higher value), which means it passivates the rear-side contact properly.

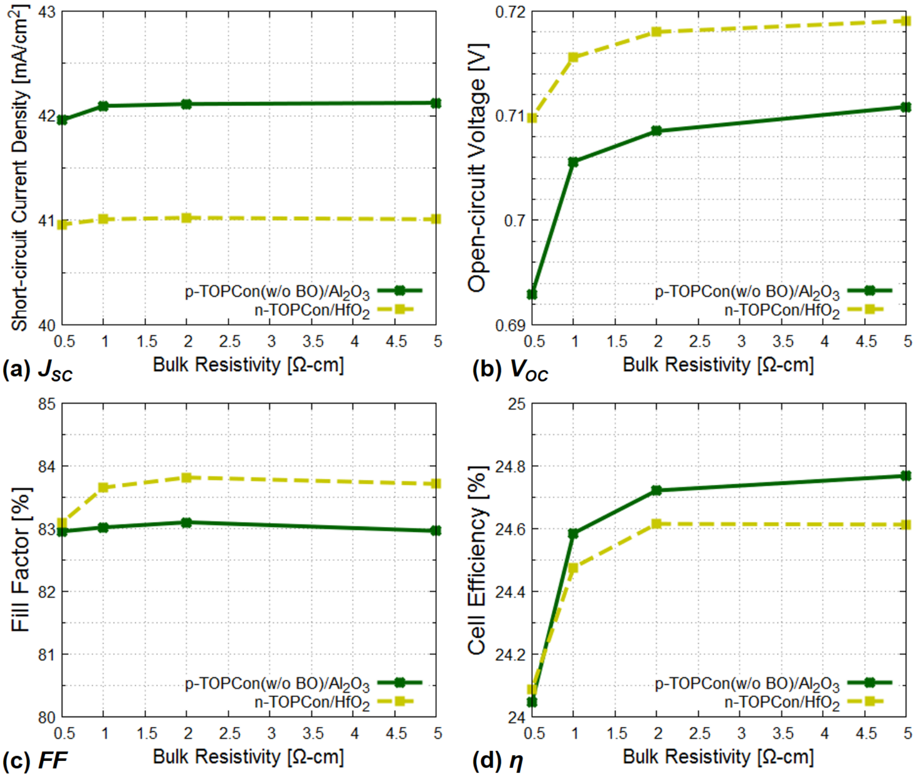

(a) J_{SC} (b) V_{OC}

(c) *FF* (d) η

Figure 6.17: Cell performances of TOPCon solar cells against bulk resistivity

6.4.5 Conclusion

The TOPCon solar cell performances were evaluated for different bulk types and tunnel dielectric materials. The fixed charge effect that comes from the tunnel dielectric material selection appears at the higher bulk lifetime conditions of p- (w/o BO) and n-type bulks. Under this condition, the selection of tunnel dielectric materials is more difficult because both the tunnel parameters and the fixed charge effect must be considered. The prospective material, HfO_2, provides a much thicker tunnel dielectric thickness limit of over 3 nm. The minority-carrier tunnel current density must be suppressed below 0.2 mA/cm^2 to ensure sufficient contact passivation. The tunnel dielectric thickness modeling is derived based on the majority-carrier effective mass in dielectric materials, which is expressed as $t_{critical} = -13.7\ln(m_{e,h}/m_0) + 3.60$, where the R^2 value is 0.773. The maximum cell efficiency of approximately 24.8% is obtained by the p-TOPCon (w/o BO) with Al_2O_3 tunnel dielectric by adjusting the tunnel dielectric thickness and bulk resistivity.

Chapter 7

Conclusion

7.1 Summary of the research

In this study, the performance improvements of c-Si solar cells were discussed. Comprehensive studies including PERC, IBC, and TOPCon were performed using numerical simulations. The following sections summarize the findings of these studies.

7.1.1 PERC

Outline: The bifacial PERC structure was evaluated for different illumination conditions.
•The optimized cell designs, with different types of bulk doping type and quality, and the optimized contact placement against the rear passivation quality were revealed.
•The bulk quality was the most important factor. The use of higher-quality bulk enabled the resistivity and carrier mobility to influence the cell performances.
•The illumination condition of the monofacial and bifacial situations did not affect the optimized cell designs; however, the bifacial situation made the rear designs dominant and sensitive against it.

7.1.2 IBC

Outline: The bifacial IBC structure was evaluated for front doping of FFE and FSF under different illumination conditions.
•The optimized doping profiles and the FFE scheme provide better cell performance.
•The unit cell determined which of the two schemes was better, the FFE or the FSF scheme, and the smaller unit cell made the FSF scheme more suitable. How-

ever, the optimized design revealed that the FFE finally demonstrated higher performance.
•IQE mapping and loss analysis revealed the loss dominant part and mechanism of the IBC solar cell.

7.1.3 TOPCon

Outline: The selection of tunnel dielectric materials was studied for different bulk types.
•The selection of tunnel dielectric materials was more difficult in the condition with higher bulk lifetime because both tunnel parameters and fixed charge effect were dominant.
•The adoption of Al_2O_3 for p-type and HfO_2 for n-type bulks was the best option for five tunnel dielectric materials. HfO_2 in the n-type bulk increased the acceptable thickness.
•The majority-carrier effective mass determined the acceptable tunnel dielectric thickness, which was following the log-scale variation.
•The higher bulk resistivity was suitable for the TOPCon solar cell, and the p-type bulk without the BO-cluster produced the highest performance.

The results of the above studies can improve future cell performance in the PV industry using the provided cell designs.

7.2 Outlook in the PV field

The increasing demands of renewable energy is significantly expanding the PV market. The necessary improvements required in solar cells are increased conversion efficiency and reduced costs of manufacturing and installation.

7.2.1 For improving cell performances

Improving the cell performances requires advances in solar cell structures, which includes proposal of new structures or optimization of the existing structures. One candidate with the highest c-Si solar cell efficiency adopts HBC, which is a combination of IBC and c-Si / a-Si heterojunction [8]. The highest cell efficiency achieved by a single-junction solar cell is 26.7% [3], which leads to further improvements in c-Si solar cells.

Moreover, the emerging technology of TOPCon provides high performance, which is rendered by the compatible higher V_{OC} and FF [7]. The i-TOPCon [91] process improves the performance of J_{SC} by absorbing incident light from both sides, which can improve the three main performance parameters of the cell. This feature makes i-TOPCon another potential candidate in c-Si solar cells.

The HBC and i-TOPCon structures will be the leading cell structures in the near future developments of the PV field. The development of these structures is complex; thus, simulations become considerably important.

7.2.2 For low costing

Altering a conventional Al-BSF structure requires complex manufacturing processes and higher costs. Furthermore, the adoption of higher-quality n- or p-type bulks without the BO-cluster is also expensive.

The PERC structure is cheaper as compared to other advanced solar cells, which contributes small additional processes to a conventional Al-BSF solar cell. Overall, the advances of PERC solar cells can facilitate both, higher performance and reduced manufacturing cost. The PERC structure is now in increased demand and will soon be the most commonly used solar cell structure, [1]; thus, PERC research will continue to be the first topic in the PV field.

Furthermore, the choice of materials is important not only to improve performance, but also to reduce costs. In particular, for TOPCon solar cells, the choice of tunnel materials is one of the most important factors. Simulations can help in evaluating and determining the suitable material, which is an important factor.

Summing up the results of process simulations to evaluate the whole manufacturing process can provide more information. The optimized process can be determined by simulation, which can predict the manufacturing costs.

7.2.3 Simulation in the PV field

The solar cell simulation provides a lot of useful information, which includes how to improve cell performance, optimized cell designs, and the performance of loss analysis. As mentioned earlier, simulations performed before the manufacturing stage helps in suppressing the process duration and costs. However, modeling needs several repetition of the experiments. The simulation results will provide feedback for realistic manufacturing of solar cells by predicting their features.

Therefore, advances in the PV field require both experimental research and simulations to improve performance, reduce costs, and for further developments.

References

[1] A. Blakers, "Development of the PERC solar cell," IEEE J. Photovolt. Vol. 9, No. 3, pp. 629-635, May. 2019.

[2] K. Sopian, S. L. Cheow, and S. H. Zaidi, "An overview of crystalline silicon solar cell technology: Past, present, and future," AIP Conf. Proc. Vol. 1877, No. 1, 020004, Sep. 2017.

[3] M. A. Green, E. D. Dunlop, D. H. Levi, J. Hohl-Ebinger, M. Yoshita, and A. W. Y. Ho-Baillie, "Solar cell efficiency tables (version 54)," Prog. Photovolt. Res. Appl. Vol. 27, No. 7, pp. 565-575, Jul. 2019.

[4] M. A. Green, A. W. Blakers, J. Zhao, A. M. Milne, A. Wang, and X. Dai, "Characterization of 23-percent efficient silicon solar cells," IEEE Trans. Elec. Dev. Vol. 37, No. 2, pp. 331-336, Feb. 1990.

[5] M. D. Lammer and R. J. Schwartz, "The interdigitated back contact solar cell: A silicon solar cell for use in concentrated sunlight," IEEE Trans. Elec. Dev. Vol. ED-24, No. 4, pp. 337-342, Apr. 1977.

[6] K. Wakisaka, M. Taguchi, T. Sawada, M. Tanaka, T. Matsuyama, T. Matsuoka, S. Tsuda, S. Nakano, Y. Kishi, and Y. Kuwano, "More than 16% solar cells with a new "HIT" (doped a-Si/ non-doped a-Si/ crystalline Si) structure," The Conf. Record of the 22nd IEEE Photovolt. Spec. Conf. Vol. 2, pp. 887-892, Oct. 1991.

[7] F. Feldmann, M. Bivour, C. Reichel, M. Hermle, and S. W. Glunz, "Passivated rear contacts for high-efficiency n-type Si solar cells providing high interface passivation quality and excellent transport characteristics," Sol. Energy Mater. Sol. Cells Vol. 120, Part A, pp. 270-274, Jan. 2014.

[8] K. Yoshikawa, W. Yoshida, T. Irie, H. Kawasaki, K. Konishi, H. Ishibashi, T. Asatani, D. Adachi, M. Kanematsu, H. Uzu, and K. Yamamoto, "Exceeding

conversion efficiency of 26% by heterojunction interdigitated back contact solar cell with thin film Si technology," Sol. Energy Mater. Sol. Cells Vol. 173, Part A, pp. 37-42, Dec. 2017.

[9] J. Nakamura, N. Asano, T. Hieda, C. Okamoto, H. Katayama, and K. Nakamura, "Development of heterojunction back contact Si solar cells," IEEE J. Photovolt. Vol. 4, No. 6, pp. 1491-1495, Nov. 2014.

[10] K. Masuko, M. Shigematsu, T. Hashiguchi, D. Fujishima, M. Kai, N. Yoshimura, T. Yamaguchi, Y. Ichihashi, T. Mishima, N. Matsubara, T. Yamanishi, T. Takahama, M. Taguchi, E. Maruyama, and S. Okamoto, "Achievement of more than 25% conversion efficiency with crystalline silicon heterojunction solar cell," IEEE J. Photovolt. Vol. 4, No. 6, pp. 1433-1435, Nov. 2014.

[11] K. Yoshikawa, H. Kawasaki, W. Yoshida, T. Irie, K. Konishi, K. Nakano, T. Uto, D. Adachi, M. Kanematsu, H. Uzu, and K. Yamamoto, "Silicon heterojunction solar cell with interdigitated back contacts for a photoconversion efficiency over 26%," Nat. Energy Vol. 2, 17032, Mar. 2017.

[12] A. Kojima, K. Teshima, Y. Shirai, and T. Miyasaka, "Organometal halide perovskites as visible-light sensitizers for photovoltaic cells," J. Am. Chem. Soc. Vol. 131, No. 17, pp. 6050-6051, Apr. 2009.

[13] A. K. Jena, A. Kulkami, and T. Miyasaka, "Halide perovskite photovoltaics: background, status, and future prospects," Chem. Rev. Vol. 119, No. 5, pp. 3036-3103, Mar. 2019.

[14] J. Ramanujam and U. P. Singh, "Copper indium gallium selenide based solar cells - a review," Energy Environ. Sci. Vol. 10, No. 6, pp. 1306-1319, Mar. 2017.

[15] M. Nakamura, K. Yamaguchi, Y. Kimoto, Y. Yusuke, T. Kato, and H. Sugimoto, "Cd-free Cu(In,Ga)(Se,S)$_2$ thin-film solar cell with record efficiency of 23.35%," IEEE J. Photovolt. Vol. 9, No. 6, pp. 1863-1867, Nov. 2019.

[16] K. Makita, H. Mizuno, T. Tayagaki, T. Aihara, R. Oshima, Y. Shoji, H. Sai, H. Takato, R. Müller, P. Beutel, D. Lackner, J. Benick, M. Hermle, F. Dimroth, and T. Sugaya, "III-V/Si multijunction solar cells with 30% efficiency using

smart stack technology with Pd nanoparticle array," Prog. Photovolt. Res. Appl. Vol. 28, No. 1, pp. 16-24, Jan. 2020.

[17] D. A. Clugston and P. A. Basore, "PC1D version 5: 32-bit solar cell modeling on personal computers," Conf. Record the 26th IEEE Photovolt. Spec. Conf., pp. 207-210, Sep. 1997.

[18] T. Sugiura, "Improvements of PERC solar cell performances with TCAD simulation," Keio University, School of Integrated Design Engineering Master thesis, Mar. 2018.

[19] S. Ning, "Simulation and process development for ion-implanted n-type silicon solar cells," Georgia Institute of Tech. Master Thesis of Sci. Electro. Computer Engineering, May. 2013.

[20] J. O. Schumacher, "Numerical simulation of silicon solar cells with novel cell structures," Fraunhofer-Institut für Solare Energiesysteme Freiburg, Ph.D. thesis, 2000.

[21] Vinod, R. Kumar, and S. K. Singh, "Solar photovoltaic modeling and simulation: As a renewable energy solution," Energy Reports Vol. 4, pp. 701–712, Nov. 2018.

[22] A. Cuevas, "The recombination parameter J_0," Energy Procedia Vol. 55, pp. 53-62, Dec. 2014.

[23] S. C. Baker-Finch and K. R. McIntosh, "Reflection of normally incident light from silicon solar cells with pyramidal texture," Prog. Photovolt. Res. Appl. Vol. 19, No. 4, pp. 406-416, Jun. 2011.

[24] R. S. Bonilla, B. Hoex, P. Hamer, and P. R. Wilshaw, "Dielectric surface passivation for silicon solar cells: A review," Phys. Status Solidi A Vol. 214, No. 7, 1700293, Jun. 2017.

[25] J. Schmidt, F. Werner, B. Veith, D. Zielke, S. Steingrube, P. P. Altermatt, S. Gatz, T. Dullweber, and R. Brendel, "Advances in the surface passivation of silicon solar cells," Energy Procedia Vol. 15, pp. 30-39, Dec. 2012.

[26] R. R. King, R. A. Sinton, and R. M. Swanson, "Studies of diffused phosphorus emitters: Saturation current, surface recombination velocity, and quantum efficiency," IEEE Trans. Elec. Dev. Vol. 37, No. 2, pp. 365-371, Feb. 1990.

[27] N. Wehmeier, G. Schraps, H. Wagner, B. Lim, N. Harder, and P. P. Altermatt, "Boron-doped PECVD silicon oxides as diffusion sources for simplified high-efficiency solar cell fabrication," 28th Euro. Photovolt. Sol. Energy Conf. Exhibit., pp. 1980-1984, Sep. 2013.

[28] P. Godlewski, R. Baraona, and H. Brandhorst Jr., "Low-high junction theory applied to solar cells," Sol. Energy Vol. 29, No. 2-3, pp. 131-150, Aug. 1990.

[29] J. G. Fossum and E. L. Burgess, "High-efficiency p^+-n-n^+ back-surface-field silicon solar cells," Appl. Phys. Lett. Vol. 33, No. 3, pp. 238-240, Aug. 1978.

[30] A. Kaminski, B. Vandelle, A. Fave, J. P. Boyeaux, L. Q. Nam, R. Monna, D. Sarti, and A. Laugier, "Aluminum BSF in silicon solar cells," Sol. Energy Mat. Sol. Cells Vol. 72, No. 1-4, pp. 373-379, Apr. 2002.

[31] Y. Fan, P. Han, P. Liang, Y. Xing, X. Mao, and S. Hu, "Investigation of the forming process and characteristics of Al-BSF in silicon solar cells," International Conf. on Mat. for Renewable Energy and Environment, pp. 57–61, Aug. 2013.

[32] T. F. Ciszek, M. R. Page, T. H. Wang, and J. A. Casey, "Float-zone and Czochralski crystal growth and diagnostic solar cell evaluation of a new solar-grade feedstock source," Conf. Record of the 29th IEEE Photovolt. Spec. Conf., pp. 210-213, May. 2002.

[33] X. Yu and D. Yang, "Growth of crystalline silicon for solar cells: Czochralski Si," Handbook of Photovoltaic Silicon, Springer, Berlin, Heidelberg, pp. 129-174, Nov. 2019.

[34] B. Singha and C. S. Solanki, "N-type solar cells: advantages, issues, and current scenarios," Mater. Res. Express Vol. 4, No. 7, 072001, Jul. 2017.

[35] C. Battaglia, A. Cuevas, and S. D. Wolf, "High-efficiency crystalline silicon solar cells: status and perspectives," Energy Environ. Sci. Vol. 9, No. 5, pp. 1552-1576, Feb. 2016.

[36] S. W. Glunz, S. Rein, J. Y. Lee, and W. Warta, "Minority carrier lifetime degradation in boron-doped Czochralski silicon," J. Appl. Phys. Vol. 90, No. 5, pp. 2397-2404, Sep. 2001.

[37] B. A. Veith-Wolf, S. Schäfer, R. Brendel, and J. Schmidt, "Reassessment of intrinsic lifetime limit in n-type crystalline silicon and implication on maximum solar cell efficiency," Sol. Energy Mater. Sol. Cells Vol. 186, pp. 194-199, Nov. 2018.

[38] T. Niewelt, J. Schön, W. Warta, S. W. Glunz, and M. C. Schubert, "Degradation of crystalline silicon due to boron-oxygen defects," IEEE J. Photovolt. Vol. 7, No. 1, pp. 383-398, Jan. 2017.

[39] D. C. Walter, B. Lim, and J. Schmidt, "Realistic efficiency potential of next-generation industrial Czochralski-grown silicon solar cells after deactivation of the boron-oxygen-related defect center," Prog. Photovolt. Res. Appl. Vol. 24, No. 7, pp. 920-928, Jul. 2016.

[40] D. J. Roulston, N. D. Arora, and S. G. Chamberlain, "Modeling and measurement of minority-carrier lifetime versus doping in diffused layers of n^+-p silicon diodes," IEEE Trans. Elec. Dev. Vol. ED-29, No. 2, pp. 284-291, Feb. 1982.

[41] B. Ding, "Improving radiative recombination efficiency of green light-emitting diodes," Mater. Sci. Tech. B Vol. 34, No. 14, pp. 1615-1630, Apr. 2018.

[42] P. P. Altermatt, F. Geelhaar, T. Trupke, X. Dai, A. Neisser, and E. Daub, "Injection dependence of spontaneous radiative recombination in crystalline silicon: Experimental verification and theoretical analysis," Appl. Phys. Lett. Vol. 88, No. 26, 261901, Jun. 2006.

[43] L. Yuan, H. Deng, S. Li, S. Wei, and J. Luo, "Unified theory of direct or indirect band-gap nature of conventional semiconductors," Phys. Review B Vol. 98, No. 24, 245203, Dec. 2018.

[44] A. Richter, S. W. Glunz, F. Werner, J. Schmidt, and A. Cuevas, "Improved quantitative description of Auger recombination in crystalline silicon," Phys. Review B Vol. 86, No. 16, 165202, Oct. 2012.

[45] P. Singh and N. M. Ravindra, "Temperature dependence of solar cell performance - an analysis," Sol. Energy Mater. Sol. Cells Vol. 101, pp. 36-45, Jun. 2012.

[46] A. Abdallah, O. El Daif, B. Aïssa, M. Kivambe, N. Tabet, J. Seif, J. Haschke, J. Cattin, M. Boccard, S. D. Wolf, and C. Ballif, "Towards an optimum silicon heterojunction solar cell configuration for high temperature and high light intensity environment," Energy Procedia Vol. 124, pp. 331-337, Sep. 2017.

[47] Sentaurus Device User Guide (Synopsys, Mountain View, CA, 2016), Version L-2016.03 (Synopsys, Mountain View, CA, 2016).

[48] G. H. Spencer and M. V. R. K. Murty, "General ray-tracing procedure," J. Opt. Society America Vol. 52, No. 6, pp. 672–678, Jun. 1962.

[49] C. C. Katsidis and D. I. Slapkas, "General transfer-matrix method for optical multilayer systems with coherent, partially coherent, and incoherent interference," Appl. Opt. Vol. 41, No. 19, pp. 3978-3987, Jul. 2002.

[50] W. Fichtner, D. J. Rose, and R. E. Bank, "Semiconductor device simulation," IEEE Trans. Elec. Dev. Vol. ED-30, No. 9, pp. 1018-1030, Sep. 1983.

[51] A. Fell, K. R. McIntosh, P. P. Altermatt, G. J. M. Janssen, R. Stangl, A. Ho-Baillie, H. Steinkemper, J. Greulich, M. Müller, B. Min, K. C. Fong, M. Hermle, I. G. Romijn, and M. D. Abbott, "Input parameters for the simulation of silicon solar cells in 2014," IEEE J. Photovolt. Vol. 5, No. 4, pp. 1250-1263, Jul. 2015.

[52] D. B. M. Klaassen, "A unified mobility model for device simulation - I. Model equations and concentration dependence," Sol. State Elec. Vol. 35, No. 7, pp. 953-959, Jul. 1992.

[53] A. Schenk, "Finite-temperature full random-phase approximation model of band gap narrowing for silicon device simulation," J. Appl. Phys. Vol. 84, No. 7, pp. 3684-3695, Oct. 1998.

[54] M. A. Green, "Self-consistent optical parameters of intrinsic silicon at 300 K including temperature coefficients," Sol. Energy Mater. Sol. Cell. Vol. 92, No. 11, pp. 1305-1310, Nov. 2008.

[55] D. K. Schroder, R. N. Thomas, and J. C. Swartz, "Free carrier absorption in silicon," IEEE J. Sol. State Circuits. Vol. SC-13, No. 1, pp. 180-187, Feb. 1978.

[56] D. Kray, M. Hermle, and S. W. Glunz, "Theory and experiments on the back side reflectance of silicon wafer solar cells," Prog. Photovolt. Res. Appl. Vol. 16, No. 1, pp. 1-15, Jan. 2008.

[57] C. Riordan and R. Hulstrom, "What is an Air Mass 1.5 Spectrum?" IEEE Conf. Photovolt. Spec., pp. 1085-1088, May. 1990.

[58] R. Guerrero-Lemus, R. Vega, T. Kim, A. Kimm, and L. E. Shephard, "Bifacial solar photovoltaics - A technology review," Renew. Sustain. Energy Reviews. Vol. 60, pp. 1533-1549, Jul. 2016.

[59] C. A. Gueymard, V. Lara-Fanego, M. Sengupta, and Y. Xie, "Surface albedo and reflectance: Review of definitions, angular and spectral effects, and intercomparison of major data sources in support of advanced solar irradiance modeling over the Americas," Sol. Energy Vol. 182, pp. 194-212, Apr. 2019.

[60] A. Lorenz, J. John, B. Vermang, E. Cornagliotti, and J. Poortmass, "Comparison of illumination level dependency and rear internal reflectance of PERC type cells with different dielectric passivation stacks," 26th Euro. Photovolt. Sol. Energy Conf. Exhibit., pp. 1486-1488, Jan. 2011.

[61] C. Kranz, S. Wyczanowski, S. Dorn, K. Weise, C. Klein, K. Bothe, T. Dullweber, and R. Brendel, "Impact of the rear surface roughness on industrial-type PERC solar cells," 27th Euro. Photovolt. Sol. Energy Conf. Exhibit., pp. 557-560, Jan. 2012.

[62] J. Müller, S. Gatz, K. Bothe, and R. Brendel, "Optimizing the geometry of local aluminum-alloyed contacts to fully screen-printed silicon solar cells," 38th IEEE Photovolt. Spec. Conf., pp. 2223-2228, Jun. 2012.

[63] M. Zanuccoli, R. D. Rose, P. Magnone, E. Sangiorgi, and C. Fiegna, "Performance analysis of rear point contact solar cells by three-dimensional numerical simulation," IEEE Trans. Elec. Dev. Vol. 59, No. 5, pp. 1311-1319, May. 2012.

[64] M. Müller, P. P. Altermatt, H. Wagner, and G. Fischer, "Sensitivity analysis of industrial multicrystalline PERC silicon solar cells by means of 3-D device simulation and metamodeling," IEEE J. Photovolt. Vol. 4, No. 1, pp. 107-113, Jan. 2014.

[65] M. Ernst, D. Walter, A. Fell, B. Lim, and K. Weber, "Efficiency potential of p-type Al_2O_3/SiN_x passivated PERC solar cells with locally laser-doped rear contacts," IEEE J. Photovolt. Vol. 6, No. 3, pp. 624-631, May. 2016.

[66] R. Khoury, I. Martin, G. López, C. Jin, J. M. Ló pez–González, L. Zeyu, P. Bulkin, E. V. Johnson, and R. Alcubilla, "Partially contacted surfaces with contact size in the 1 μm range for c-Si PERC solar cells," IEEE 44th Photovolt. Spec. Conf., pp. 1781-1786, Jun. 2017.

[67] T. Dullweber, C. Kranz, R. Peibst, U. Baumann, H. Hannebauer, A. Fülle, S. Steckemetz, T. Weber, M. Kutzer, M. Müller, G. Fischer, P. Palinginis, and H. Neuhaus, "PERC+: industrial PERC solar cells with rear Al grid enabling bifaciality and reduced Al paste consumption," Prog. Photovolt. Res. Appl. Vol. 24, No. 12, pp. 1487-1498, Dec. 2016.

[68] Th. Katsaounis, K. Kotsovos, I. Gereige, A. Al-Saggaf, and A. Tzavaras, "2D simulation and performance evaluation of bifacial rear local contact c-Si solar cells under variable illumination conditions," Sol. Energy Vol. 158, pp. 34-41, Dec. 2017.

[69] **T. Sugiura, S. Matsumoto, and N. Nakano, "Bifacial PERC solar cell designs: Bulk and rear properties and illumination condition," IEEE J. Photovolt. Vol.10, Iss.6, pp.1538-1544, Nov. 2020.**

[70] P. Spinelli, B. W. H. van de Loo, A. H. G. Vlooswijk, W. M. M. Kessels, and I. Cesar, "Quantification of pn-junction recombination in interdigitated back-contact crystalline silicon solar cells," IEEE J. Photovolt. Vol. 7, No. 5, pp. 1176-1183, Sep. 2017.

[71] M. Hermle, F. Granek, O. Schultz-Wittmann, and S. W. Glunz, "Shading effects in back-junction back-contacted silicon solar cells," 33rd IEEE Photovolt. spec. Conf., May. 2008.

[72] C. Reichel, F. Granek, M. Hermle, and S. W. Glunz, "Investigation of electrical shading effects in back-contacted back-junction silicon solar cells using the two-dimensional charge collection probability and the reciprocity theorem," J. Appl. Phys. Vol. 109, No. 2, 024507, Jan. 2011.

[73] I. Cesar, N. Guillevin, A. R. Burgers, A. A. Mewe, M. Koppes, J. Anker, L. J. Geerligs, and A. W. Weeber, "Mercury: A back junction back contact

front floating emitter cell with novel design for high efficiency and simplified processing," Energy Procedia Vol. 55, pp. 633-642, Dec. 2014.

[74] N. Harder, V. Mertens, and R. Brendel, "Buried emitter solar cell structures: Decoupling of metallisation geometry and carrier collection geometry of back contacted solar cells," Phys. Stat. Sol. (RRL) Vol. 2, No. 4, pp. 148-150, Aug. 2008.

[75] N. Harder, V. Mertens, and R. Brendel, "Numerical simulations of buried emitter back-junction solar cells," Prog. Photovolt. Res. Appl. Vol. 17, No. 4, pp. 253-263, Jun. 2009.

[76] C. Reichel, A. Fell, M. Hermle, and S. W. Glunz, "Back-contacted back-junction Si solar cells with locally overcompensated diffusion regions - comparison of buried emitter and floating base design," Phys. Stat. Sol. A Vol. 216, No. 4, 1800791, Feb. 2019.

[77] W. T. Matzen, S. Y. Chang, and B. G. Carbajal, "A device model for the tandem junction solar cell," IEEE Trans. Elec. Dev. Vol. ED-26, No. 9, pp. 1365-1368, Sep. 1979.

[78] A. R. Burgers, I. Cesar, N. Guillevin, A. A. Mewe, P. Spinelli, and A. W. Weeber, "Designing IBC cells with FFE: long range effects with circuit simulation," IEEE 43rd Photovolt. Spec. Conf., pp. 2408-2411, Jun. 2016.

[79] M. W. P. E. Lamers, A. A. Mewe, I. G. Romijn, E. E. Bende, Y. Komatsu, and M. Koppes. D. Morecroft, M. Cascant, F. J. Castaño, A. W. Weeber, and I. Cesar, "Towards 21% efficient n-Cz IBC based on screen printing," 26th Euro. Photovolt. Sol. Energy Conf. Exhibit. Sep. 2011.

[80] D. Ding, H. Lin, H. Liu, G. Lu, Z. Li, Y. Zhang, and W. Shen, "High-efficiency interdigitated back contact silicon solar cells with front floating emitter," Phys. Stat. Sol. A Vol. 216, No. 23, 1900445, Dec. 2019.

[81] **T. Sugiura, S. Matsumoto, and N. Nakano, "Optimization of Front Diffusion Profile in Bifacial Interdigitated Back Contact Solar Cell," IEEE J. Photovolt. Vol.10, Iss.6, pp.1582-1590, Nov. 2020.**

[82] T. Tachibana, T. Mochizuki, K. Shirasawa, and H. Takato, "An investigation of internal quantum efficiency of bifacial interdigitated back contact (IBC)

crystalline silicon solar cell," IEEE J. Photovolt. Vol. 9, No. 6, pp. 1526-1531, Nov. 2019.

[83] T. Tachibana, K. Tanahashi, T. Mochizuki, K. Shirasawa, and H. Takato, "Bifacial interdigitated-back-contact (IBC) crystalline silicon solar cell: fabrication and evaluation by internal quantum efficiency mapping," IEEE 7th World Conf. Photovolt. Energy Conv., pp. 3738-3742, Jun. 2018.

[84] I. Cesar, N. Guillevin, A. A. Mewe, P. Spinelli, A. R. Burgers, V. Rosca, L. A. G. Okel, B. J. Geerligs, A. W. Weeber, S. Sawallich, and M. Nagel, "Enablers for IBC: integral cell and module development and implementation in PV industry," Energy Procedia Vol. 124, pp. 834-841, Sep. 2017.

[85] A. G. Aberle, W. Zhang, and B. Hoex, "Advanced loss analysis method for silicon wafer solar cells," Energy Procedia Vol. 8, pp. 244–249, Dec. 2011.

[86] R. Brendel, S. Dreissigacker, N. -P. Harder, and P. P. Altermatt, "Theory of analyzing free energy losses in solar cells," Appl. Phys. Lett. Vol. 93, No. 17, 173503, Oct. 2008.

[87] G. Micard and G. Hahn, "Free energy loss analysis decomposition of the power voltage characteristic of an interdigitated back contact solar cell" 29th Euro. Photovolt. Sol. Energy Conf. Exhibit., pp. 1267-1271, Sep. 2014.

[88] A. richter, M. Hermle, and S. W. Glunz, "Reassessment of the limiting efficiency for crystalline silicon solar cells," IEEE J. Photovolt. Vol. 3, No. 4, pp. 1184-1191, Oct. 2013.

[89] C. Messmer, A. Fell, F. Feldmann, N. Wöhrle, J. Schön, and M. Hermle, "Efficiency roadmap for evolutionary upgrades of PERC solar cells by TOPCon: Impact of parasitic absorption," IEEE J. Photovolt. Vol. 10, No. 2, pp. 335-342, Mar. 2020.

[90] F. Feldmann, M. Bivour, C. Reichel, H. Steinkemper, M. Hermle, and S. W. Glunz, "Tunnel oxide passivated contacts as an alternative to partial rear contacts," Sol. Energy Mater. Sol. Cells Vol. 131, pp. 46-50, Dec. 2014.

[91] D. Chen, Y. Chen, Z. Wang, J. Gong, C. Liu, Y. Zou, Y. He, Y. Wang, L. Yuan, W. Lin, R. Xia, L. Yin, X. Zhang, G. Xu, Y. Yang, H. Shen, Z. Feng,

P. P. Altermatt, and P. J. Verlinden, ”24.58% total area efficiency of screen-printed, large area industrial silicon solar cells with the tunnel oxide passivated contacts (i-TOPCon) design,” Sol. Energy Mater. Sol. Cell. Vol. 206, 110258, Mar. 2020.

[92] A. Schenk and G. Heiser, ”Modeling and simulation of tunneling through ultra-thin gate dielectrics,” J. Appl. Phys. Vol. 81, No. 12, pp. 7900-7908, Jun. 1997.

[93] **T. Sugiura, S. Matsumoto, and N. Nakano, ”Evaluations of TOPCon solar cell rear structure on numerical simulation,” International Conf. Sol. State Dev. Mater., pp. 817-818, Sep. 2019.**

[94] **T. Sugiura, S. Matsumoto, and N. Nakano, ”Numerical analysis of p-type and n-type based carrier-selective contact solar cells with tunneling oxide thickness and bulk properties,” Jpn. J. Appl. Phys. Vol. 59, No. SG, SGGF03, Feb. 2020.**

[95] Y. C. Yeo, Q. Lu, W. C. Lee, T. King, C. Hu, X. Wang, X. Guo, and T. P. Ma, ”Direct tunneling gate leakage current in transistors with ultrathin silicon nitride gate dielectric,” IEEE Elec. Dev. Lett. Vol. 21, No. 11, pp. 540-542, Nov. 2000.

[96] T. V. Perevalov, A. V. Shaposhnikov, V. A. Gritsenko, H. Wong, J. H. Han, and C. W. Kim, ”Electronic structure of α-Al_2O_3: ab initio simulations and comparison with experiment,” JETP Lett. Vol. 85, No. 3, pp. 165-168, Apr. 2007.

[97] E. Bersch, S. Rangan, R. A. Bartynski, E. Garfunkel, and E. Vescovo, ”Band offsets of ultrathin high-κ oxide films with Si,” Phys. Rev. B. Vol. 78, No. 8, 085114, Aug. 2008.

[98] J. Deckers, E. Cornagliotti, M. Debucquoy, I. Gordon, R. Mertens, and J. Poortmans, ”Aluminum oxide-aluminum stacks for contact passivation in silicon solar cells,” Energy Procedia Vol. 55, pp. 656-664, Sep. 2014.

[99] B. Enright and D. Fitzmaurice, ”Spectroscopic determination of electron and hole effective masses in a nanocrystalline semiconductor film,” J. Phys. Chem. Vol. 100, No. 3, pp. 1027-1035, Jan. 1996.

[100] S. S. Surah, M. Vishwakarma, R. Kumar, R. Nain, S. Sirohi, and G. Kumar, ” Tuning the electronic band alignment properties of TiO_2 nanotubes by boron doping. Phys. Vol. 12, pp. 1725-1731, Mar. 2019.

[101] D. Suh, D. Choi, and K. J. Weber, ”Al_2O_3/TiO_2 stack layers for effective surface passivation of crystalline silicon,” J. Appl. Phys. Vol. 114, No. 15, 154107, Oct. 2013. Aug

[102] M. C. Cheynet, S. Pokrant, F. D. Tichelaar, and J. Rouvi ére, ”Crystal structure and band gap determination of HfO_2 thin films,” J. Appl. Phys. Vol. 101, No. 5, 054101, Mar. 2007.

[103] S. Monaghan, P. K. Hurley, K. Cherkaoui, M. A. Negara, and A. Schenk, ”Determination of electron effective mass and electron affinity in HfO_2 using MOS and MOSFET structures,” Sol. State Elec. Vol. 53, No. 4, pp. 438-444, Apr. 2009.

[104] J. C. Garcia, A. T. Lino, L. M. R. Scolfaro, J. R. Leite, V. N. Freire, G. A. Farias, and E. F. da Silva, ”Band structure derived properties of HfO_2 from first principles calculations,” AIP Conf. Proc. Vol. 772, No. 1, pp. 189-190, Aug. 2005.

[105] M. Sohgawa, M. Yoshida, T. Naoyama, T. Tada, K. Ikeda, T. Kanashima, A. Fujimoto, and M. Okuyama, ”Contactless characterization of fixed charges in HfO_2 thin film from photoreflectance,” Jpn. J. Appl. Phys. Vol. 44, No. 4B, pp. 2409-2414, Apr. 2005.

[106] S. Mitra, H. Ghosh, H. Saha, and K. Ghosh, ”Recombination analysis of tunnel oxide passivated contact solar cells,” IEEE Trans. Elec. Dev. Vol. 66, No.3, pp. 1368-1376, Mar. 2019.

[107] J. Melskens, B. W. H. van de Loo, B. Macco, L. E. Black, S. Smit, and W. M. M. (Erwin) Kessels, ”Passivating contacts for crystalline silicon solar cells: from concepts and materials to prospects,” IEEE J. Photovolt. Vol. 8, No. 2, pp. 373-388, Mar. 2018.

[108] H. D. Barber, ”Effective mass and intrinsic concentration in silicon,” Sol. State Elec. Vol. 10, No. 11, pp. 1039-1051, Nov. 1967.

[109] G. Ribes, J. Mitard, M. Denais, S. Bruyere, F. Monsieur, C. Parthasarathy, E. Vincent, and G. Ghibaudo, "Review on high-κ dielectrics reliability issues," IEEE Trans. Dev. Mater. Reliability, Vol. 5, No. 1, pp. 5–19, Mar. 2005.

[110] **T. Sugiura, S. Matsmoto, and N. Nakano, "Numerical analysis of tunnel oxide passivated contact solar cell performances for dielectric thin film materials and bulk properties," Sol. Energy (Submitted)**

[111] B. Steinhauser, F. Feldmann, J. Polzin, L. Tutsch, V. Arya, B. Grübel, A. Fischer, A. Moldovan, J. Benick, A. Richter, A. A. Brand, S. Kluska, and M. Hermle, "Large area TOPCon technology achieving 23.4% efficiency," IEEE 7th World Conf. Photovolt. Energy Conv., pp. 1507-1510, Jun. 2018.

[112] F. Feldmann, B. Steinhauser, V. Arya, A. Büchler, A. A. Brand, S. Kluska, M. Hermle, and S. W. Glunz, "Evaluation of TOPCon technology on large area solar cells," 33rd Euro. Photovolt. Sol. Energy Conf. Exhibit., pp. 465-467, Sep. 2017.

[113] B. E. Davis and N. C. Strandwitz, "Aluminum oxide passivating tunneling interlayers for molybdenum oxide hole-selective contacts," IEEE J. Photovolt. Vol. 10, No. 3, pp. 722-728, May. 2020.

Publications and presentations

A Related publications

c-Si photovoltaics

•Takaya Sugiura, Satoru Matsumoto, and Nobuhiko Nakano, "Bifacial PERC solar cell design: Bulk and rear properties and illumination condition," IEEE Journal of Photovoltaics Vol. 10, No. 6, pp. 1538-1544, Nov. 2020. (Chapter 4: PERC solar cell)

•Takaya Sugiura, Satoru Matsumoto, and Nobuhiko Nakano, "Optimization of front diffusion profile in bifacial interdigitated back contact solar cell," IEEE Journal of Photovoltaics Vol. 10, No. 6, pp. 1582-1590, Nov. 2020. (Chapter 5: IBC solar cell)

•Takaya Sugiura, Satoru Matsumoto, and Nobuhiko Nakano, "Numerical analysis of p-type and n-type based carrier-selective contact solar cells with tunneling oxide thickness and bulk properties," Japanese Journal of Applied Physics Vol. 59, No. SG, SGGF03, Feb. 2020. (Chapter 6: TOPCon solar cell)

•Takaya Sugiura, Satoru Matsumoto, and Nobuhiko Nakano, "Numerical analysis of tunnel oxide passivated contact solar cell performances for dielectric thin film materials and bulk properties," Solar Energy (in press). (Chapter 6: TOPCon solar cell)

B Other publications

Piezoresistive modeling

•Takaya Sugiura, Naoki Takahashi, and Nobuhiko Nakano, "The piezoresistive mobility modeling for cubic and hexagonal silicon carbide crystals," Journal of Applied Physics Vol. 127, No. 24, 245113, Jun. 2020.

•Takaya Sugiura, Naoki Takahashi, and Nobuhiko Nakano, "Evaluation of p-Type 4H-SiC piezoresistive coefficients in (0001) plane using numerical simulation," Materials Science Forum Vol. 1004 (ICSCRM2019 Proceedings), pp. 249-255, Jul. 2020.

C Proceedings of the conference

c-Si photovoltaics

•Takaya Sugiura, Satoru Matsumoto, and Nobuhiko Nakano, ”Design of emitter doping profile and junction depth in Si solar cells,” The 7th International Symp. Adv. Sci. Tech. Silicon Mater., 2016.11.21-25, Hawaii, USA.

D International conference presentations

c-Si photovoltaics

•Takaya Sugiura, Satoru Matsumoto, and Nobuhiko Nakano, ”Evaluation of TOPCon solar cell rear structure on numerical simulation,” 2019 International Conference on Solid State Devices and Materials, 2019.09.02-05, Nagoya University, Aichi.

Piezoresistive modeling

•Takaya Sugiura, Naoki Takahashi, and Nobuhiko Nakano, ”Evaluation of p-Type 4H-SiC piezoresistive coefficients in (0001) plane using numerical simulation,” International Conference on Silicon Carbide and Related Materials 2019, 2019.09.29-10.04, Kyoto International Conference Center, Kyoto.

E Domestic conference presentations

c-Si photovoltaics

• 杉浦隆弥、松本智、中野誠彦 ”PERC型太陽電池の性能向上を目指したTCADシミュレーション” 第65回応用物理学会春季学術講演会、西早稲田、2018年3月17日-20日

• 杉浦隆弥、松本智、中野誠彦 ”Si太陽電池のエミッタ最適化による発電効率向上のシミュレーション” 第4回再生可能集積システム研究会、慶應大学日吉、2016年10月29日

Acknowledgments

This study was conducted at Nakano Laboratory, Department of Electronics and Electrical Engineering, Faculty of Science and Technology, Keio University. I am grateful to Associate Professor, Dr. Nobuhiko Nakano for supervising my research since 2015.

Furthermore, I am grateful to Emeritus Professor, Dr. Satoru Matsumoto for suggesting the research on solar cells.

I would like to acknowledge my thesis committee, i.e., Prof. Hiroki Ishikuro, Associate Prof. Kei Noda, and Prof. Kohei Itoh for their insightful comments and suggestions that helped me complete my thesis.

I am also indebted to Dr. Hidetaka Takato, Dr. Toshimitsu Mochiduki, and Dr. Tomihisa Tachibana at the National Institute of Advanced Industrial Science and Technology (AIST) for their suggestions on my research.

In addition to the research on solar cells, I would like to express my gratitude to Assistant Prof. Hidetoshi Takahashi for suggesting the research on piezoresistive modeling. Furthermore, I am thankful to Mr. Naoki Takahashi and Mr. Ryohei Sakota for supporting my research in the field of piezoresistive modeling.

This study was supported in part by the VLSI Design and Education Center (VDEC) and in part by the University of Tokyo in collaboration with Synopsys, Inc.